Theoretical Studies of Excited State Reactions Using Surface Hopping Molecular Dynamics and Reduced-Dimensionality Methods

状態遷移分子動力学と次元縮約法を用いた励起状態反応の理論研究

Shi Wei Liang

Graduate School of Chemical Sciences and Engineering

Hokkaido University

2024

Contents

Chapter 1 General Introduction

1.1 Excited state chemical reaction

From understanding the Woodward-Hoffmann symmetry rules by “arrow pushing” to an initio quantum calculation, supposing where the electrons are (the occupancy of the orbitals, spatial and symmetry characteries) is a central problem of understanding and predicting chemical process, The validity of this view for reaction systems can be experimentally probed by examination of the chemistry of electronically excited state, by comparison of the reactivates of states having different orbital occupations (electron configuration).

Basically, the chemical reaction is a process in which one or more substances (reactants) are converted to one or more substances(products) by rearranges the constituent atoms of reactants to created different substances products. in this rearrangement process need to be activated by some outer energy source such as chemical energy, heat energy, photo energy, or electric energy etc. The chemical reactivity of variety reaction system can be understood by the occupancy of atomic and molecular orbital. the chemical reactions were regard as two types according to their occupancy of electrons in atomic or molecule orbital. The first types can be classified into electronic ground state reaction, in which stable molecules represent minima on the ground state potential energy surface (PES). In really word, a large number of chemical reactions take place in the electronic ground state. In primarily, the Arrhenius equation was widely used to describe a reaction, determining energy for the reaction barrier. However, the Arrhenius equation ignores microcosmic mechanistic considerations such as whether one or multiple reactivate intermates are involved in the reactions. With the development of chemical theory, in 1935, transition state theory (TST)[1] was proposed simultaneously by

Henry Eyring, *Meredith Gwynne Evans* and *Michael Polanyi*, TST assumes that the reactivity of ground state reaction is controlled by a special type of chemical equilibrium (quasi-equilibrium) complex. However, word is colorful, in 2004, Scientists first discovered a wondering reaction mechanism in the dissociation reaction of formaldehyde (H_2CO) named roaming reaction.[2–4] Roaming reaction is a reaction mechanism in which products are formed via the reorientation motion in the long-range region of the potential, bypassing the reaction pathway of conventional TST. Therefore, more and more research are focused on such non-TST controlled reaction.

Another class of chemical reactions can be classified into excited state reactions, these kinds of reaction are more complicated to study than the ground state reactions because of involving multiple PESs and electronic configurations. And it was involved in different biological and chemical reactions. For example, photoswitches[5] and light-driven molecular motor[6] utilize the photoinduced cis-trans(E-Z) isomerization of the double bond (C=C or C=N) between excited state and ground state to create a unidirectional motion of molecule. A most general photoswitch is azobenzene composed of two phenyl rings interconnected by a N=N bond, which are typically isomerized with UV light (350-370 nm) to their cis form and with blue light (420-480 nm) to trans.[7] This mean cis and trans isomer of the compounds can be switched reversibly with each other by allocation of light if a particular wavelength. This photochemical property of these compounds is the reason or the photoresponsive behavior and this make them suitable for use in various applications. Such as in the development of various sensor and dyes in various industries. Light-driven molecular motor as a kind of machines which can perform their functions in the microenvironments have been studied extensively. The first molecule able to undergo photochemically powered unidirectional ration around a double bond was presented by *Ben L. Feringa* in 1999. This kind of molecule can perform a 360° full rotation of the remaining part though absorbing light energy form the environment.[8] The first-generation light-driven molecular motor perform a full rotation consisting of two steps of

photoisomerization and two steps of thermal helix inversion. Recently, some new designed light-driven molecular motor can perform a 360° full rotation though 2-step 3-step working mechanism which can improve potential application in molecular machines field[6]. in theorical research of light-driven molecular motor, photoisomerization process undergo an excited state reaction which always draw researchers' attention. For example, the factor of conversion efficiency for photoisomerization, relaxation time and the duration of excited state, etc. Therefore excited-state reaction theory and methodology is a useful tool to understand the reaction mechanism, helping the experimental designed photoswitches and light-driven molecular motor.

Moreover, excited state reaction plays a key role in the formation of chemical substances in the interstellar medium. The interstellar medium is permeated by high-energy radiation fields including UV radiation, the interstellar UV field has been known or inferred to be present since the dawn of modern astronomy. Some parts of the interstellar medium, so-called molecular clouds are shielded from the onslaught of external UV irradiation by interstellar dust particles that efficiently absorb UV and visible radiation. These cold clouds rich in molecules and ions, the presence of most molecules and ions can be explained by gas-phase chemical reactions, however, the rest of formation of molecules ions is difficult to describe simply by on ground state chemical reactions. Such as dissociative recombination reaction[9], and the interstellar ice photochemical reaction.[10] Dissociative recombination reaction is a chemical process in which a positive polyatomic ion combines with an electron, and the neutral molecule dissociates. In direct process of dissociative recombination reaction, the neutral molecules first stimulated into high excited state and then dissociated into two or more fragments, a typical example of dissociative recombination reaction in astrophysics is $CH_3+e^-\rightarrow CH_2+H$.[11] Ice photochemistry provides an attractive explanation for the existence of complex organic molecules in interstellar sources, this view has been observed in series of laboratory experiments carried out in the 1970s and 1980s, the experimental group found that UV

irradiation of interstellar ice analogs resulted in the production of large abundances of large and complex organics.[10]

In biology, biological molecules are macromolecules naturally present in cells and living organisms, as well as their man-made counterparts designed for specific functions.[12] Biomolecules vary in size and are categorized into four main types: nucleic acids, carbohydrate, lipids, and proteins along with their smaller building-blocks, such as amino acids or nucleobases. the excited state reaction is important branch in photochemical and photophysics of nucleic acids (NAs) due to the potential photochemical events triggered by UV light.[13] By excited state reaction study of nucleic acids building blocks. utilizing its photoactivated properties for designing new light-response materials. Naturally, biomolecules are exposed to the sunlight, excited state reaction can give rise to the desired processes such as the energy conversion in light-harvesting proteins or the undesired ones such as DNA damage by the UV irradiations. In addition, the light-matter interaction in biomolecules can be explored for the technology or medical applications such as energy storage, biosensing or photo-activated drug delivery. Moreover, excited state reactions occur in biochemical systems, such as the energy transfer between fluorophores in phycobiliproteins and during photosynthesis. The excited state reaction is also involved in chemiluminescence and bioluminescence process. The chemiluminescence or bioluminescence process is the emission of light due to transitions of electrons form molecular orbital of higher energy to those of lower energy, usually the ground state or the lowest unoccupied molecular orbitals. Bioluminescence is a chemiluminescence process taking place in living organisms, such as the most well-known firefly. In bioluminescence process of firefly, luciferin can be generated by oxidation of substances in the activate site of an enzyme, which contribute to the emission of light. It is believed that this reaction leads to a critical peroxide intermediate, which is actual light emitter. Therefore, a detailed study on such bioluminescence can lead us to characterize the bioluminescence properties, such as the ability to transfer the system

from ground to excited state, the lifetime of excited state relaxation, and quantum yield, etc. All of these photochemical reactions are related to the electronic excited state. Therefore, the excited state reaction keeps a very closed relationship in different field in biology and chemistry.

1.2 Photochemical reaction

Photochemistry is an interdisciplinary field of chemistry and physics, which concentrates on the photo-induced (ultraviolet light to visible light) chemical phenomena. The research and application of photochemistry is important for the basic theories and green energy utilization. the basic research of photochemistry was starting from the invention of laser technology[14] in late 1950s, providing a reliable method to observe the molecules in the microsecond scale. The development of femtosecond laser furthermore promotes the research of chemical reaction field, making it possible to observe the detailed intermediates in chemical reaction process, capturing the information for the mechanism of chemical reaction. Therefore, it is no double that the development of femtosecond laser carried a revolution in experimental photochemistry field, and consequently accelerated the improvement of photochemistry.[15] The theoretical framework of photochemistry was established in the 20th century. In early 19th century, *Grotthus* and *Draper* give the first law of photochemistry, namely, only the light absorbed by a substance, or substances is effective in bringing about chemical change, since some of it can be re-emitted in the form of heat of light. Then, Stark and Einstein improved this law under the quantum theory, which can be described as: a single photo can excite only one electron. Based on previous theories, some general photochemistry such as Lambert-Beer law, Jablonski diagram, Franck-Condon rule, etc. revealed that theorical chemist already give a good understanding of the photochemistry.

Theoretically, after light absorption, some photophysical or photochemical deactivation mechanisms can compete, and the excess energy can be released through

light emission or radiationless decay process that convert it into vibrational energy in S_0. the spectral position, shape, and width of the absorption or emission spectra will depend on all the competing event that dominate the short-timescale dynamics of the molecule. In order to systematic study the photochemical process we first to put it in relation to well-known photophysical and photochemical process. The photon energy result in excitation of an electron from the initial occupied orbital to an unoccupied higher orbital. Depending on the spin of the electrons, an electronic state can be noted as singlet and triplet, respectively.

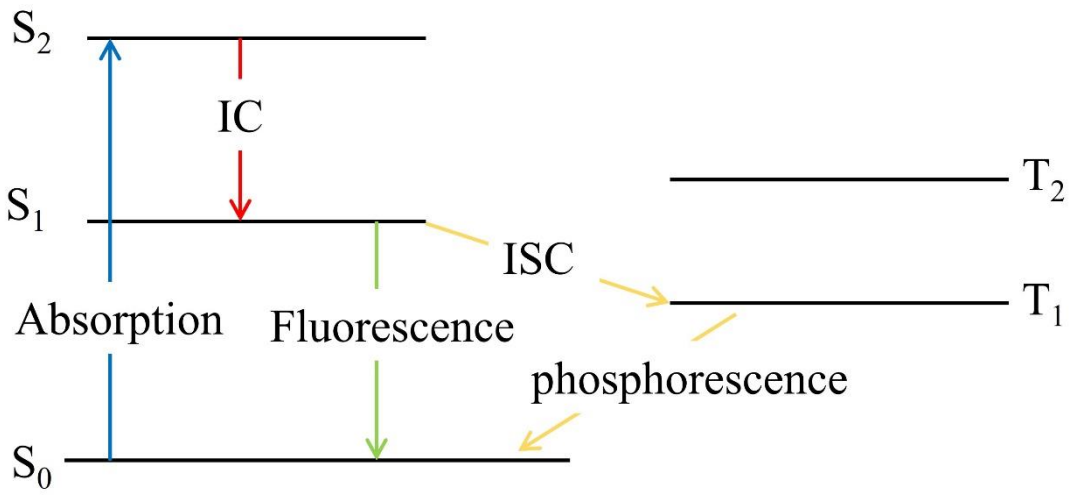

Figure. 1.1 The Jablonski Diagram of molecular absorbance and fluorescence

Figure 1.1 shows the Jablonski diagram which a schematic of the transition of electronic state of a molecule during photochemistry.[16] According to different spin and symmetry characteries, General photophysics and photochemical process refer to transition between different electronic states (ground state to excited state and vice versa), which can be classified as radiative and radiationless events. All of these phenomena occur through interactions between PESs. The most common radiative processes are (1) Spin-forbidden absorption ($S_0 \rightarrow T_1$). (2) Spin-forbidden triplet-singlet emission ($T_1 \rightarrow S_0$). (3) Spin-allowed singlet-singlet absorption ($S_0 \rightarrow T_1$). (4) Spin-allowed singlet-singlet emission ($S_1 \rightarrow S_0$). While the most common radiationless processes are: (1) Spin-

allowed transitions between two surfaces with the same spins ($S_1 \rightarrow S_0$), which two surfaces are almost degenerated along all degrees of freedom. These spin-allowed transitions or internal conversion (conical intersections (CI)) are very important to characterize and understand nonadiabatic process. (2) Spin-allowed transitions between one state to another state of different spin ($S_1 \rightarrow T_1$). These radiationless decays are known as intersystem crossings (ISC). However, Jablonski diagram does not provide any description of the course of a photochemical reaction at the microscopic level. the concept of intrinsic reaction coordinate (IRC)[17,18] allows a stationary description of the most reactive molecular geometries followed along the reaction path from reactants to products. an IRC is derived as classical trajectories for motion of the nuclei whereby the kinetic energy is removed at each step. Thus, describing a thermal chemical reaction with an IRC that connects reactants and products via a transition state is a well-established tool in computational chemistry. In contrast, most photochemical reactions are ultrafast start from an excited initial condition and involves serval PES. To be able to explain the mechanism of a chemical reaction, a detailed description of the PES is required. The PES illustrates how the excited state is populated, whether the transformation is spin-allowed or spin-forbidden, etc. Using theoretical chemistry, one can, in principle, compute the chemical properties of any system in any state, and simulate whole dynamics process by full-quantum or classical-quantum mixed method. In this branch of study, the short-lived excited states can be treated using different electronic theoretical method.

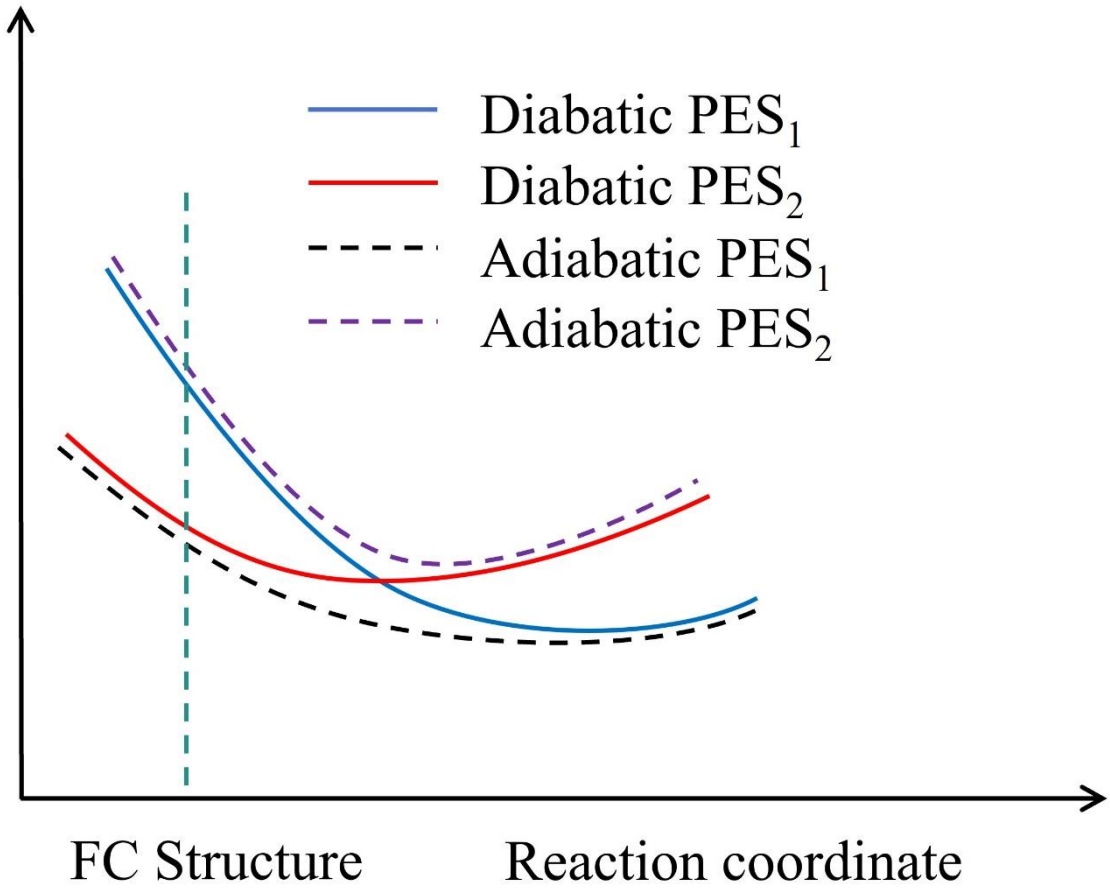

Figure 1.2 one-dimensional representation for photochemical reactions involving two adiabatic electronic states along a certain reaction coordinate, dash line represents the adiabatic potential energy surface, while solid line is diabatic potential energy surface.

We speak of a nonadiabatic photochemical process involving a between two electronic state potential energy surface as shown in **Figure 1.2**. Dash line represents the adiabatic potential energy surface, while solid line is diabatic potential energy surface. the nonadiabatic photochemical reaction can proceed through an avoided crossing, in which the excited state potential energy surface nearly touches. For a long time, people believe that electronic state with same symmetry do not cross because of non-crossing rule. However, this rule is only valid of for diatomic molecules, and it was demonstrated

by systematic quantum chemical investigations, and advances in laser spectroscopy enabling measurements of excited state lifetime in alkenes, polyenes, and aromatic compounds in the femtosecond scale. To understand the dynamics process of photochemical mechanism and demonstrate the relation to the experimental observations, one needs to apply the correct methodology for each specific system. In next chapter, we will introduce basic methodologies about nondiabetic dynamics simulation next chapter and how to analyze the result, which will allow us to answer the questions.

Chapter 2 method

2.1 AIMD nonadiabatic dynamics

Nonadiabatic coupling are intense around molecular geometries where two electronic states are degenerate. This concept was first pointed out by *Zener* in 1932 and given the calculation method of nonadiabatic transition probabilities.[19] Then, *Teller* extended the seminal work in 1937, and also demonstrated the possible existence of what he called conical crossing between PES.[20] *Zimmerman* and *Michl* were the first to suggesting at a conical intersection were the key feature to understand certain photochemical mechanisms. Since, the 1970s, conical intersection[21] have become an established paradigm for understanding reaction mechanisms in photochemical as important as transitions state in thermal chemistry.[21–23] Considering the effect of Nonadiabatic coupling needs a quantum mechanical treatment of the time evolution of the molecular geometry and of the electronica populations (occupancies of the electronic states). Theoretically, the motion of nuclei can be seen as nearly instantaneously static compared to the motion of electrons because of the mass of electrons is less than nuclei (Theory of relativity effect), which also can be called Born-Oppenheimer approximation (BOA).[24] It allows us to decouple the electronic and nuclear problem, defining the very concept of the potential energy surface. However, when chemical reaction which involves electronic excited state, nonadiabatic process led to the transition of electronic state

between different potential energy surface, corresponding to a breakdown of the BOA and demanding a treatment of both the nuclei and the electrons. There are large number of chemical problems that involve excited electronic state from photochemistry to chemical synthesis, with applications in renewable energy and bioimaging. Therefore, it is a major change in theorical field to describe the behavior of both electrons and nuclei in the context of nonadiabatic effects and excited state chemical reaction.

In order to meet the change of simulating dynamics beyond the BOA, there are two kinds of strategy have been proposed in the decades. The first one is that both electron and nuclei are described using quantum mechanics method, which so called full quantum method, such as multi-configuration time-dependent Hartree (MCTDH)[24] can provide numerically exact result at molecule level. however, this method requires a preconstructed potential energy surface and the limitation to relatively few degrees of freedom require a reduced dimensionality treatment for most molecules. That means some of the internal coordinates need to be frozen or the transformation coordinate system. Moreover, *Todd J. Martínez* proposed ab initio multiple spawning methods (AIMS)[25], which can expand the nuclear wave function in terms of linear combination of traveling Gaussian basis function. One feature of AIMS is that it can easily calculated required electronic struct quantities, including electronic state energy, and gradients are calculated on the fly.

Another method is that electron is described under quantum mechanics framework, while nuclei is treated classically. This most famous two methods are Ehrenfest dynamics[26,27] and trajectory surface hopping dynamics[28,29] method. In the former, nuclear forces are directly derived former the time-dependent propagation of an electronic wave function or density matrix, and trajectories evolve on a time-dependent average of the electronic states. In surfacing hopping dynamics, a set of electronic amplitudes are integrated together with the classical trajectories and dictate the probability that the trajectory will hop from one electronic state to other. There are two treatments of hopping probability, namely Tully's Fewest Switches[29] and Zhu-Nakamura method[30]. This thesis

focuses on nonadiabatic dynamics using trajectory surface hopping method. thus, Tully's Fewest Switches and Zhu-Nakamura method will be given in this section.

We start with a solving of the basic time-dependent Schrödinger equation (TDSE) for a molecular system as shown here:

$$i\frac{\partial\Psi(r,R,t)}{\partial t} = \hat{H}(r,R)\Psi(r,R,t) \qquad 2.1.1$$

Where r and R are the collection 3N electronic and 3N nuclear coordinates, respectively. the atomic units are used here and throughout this thesis, $\hbar$ = me = 1. The molecular system Hamiltonian can be defined as:

$$\hat{H}(r,R) = \hat{T}_{nuc} + \hat{T}_e + \hat{V}_{e-e}(r) + \hat{V}_{e-n}(r,R) + \hat{V}_{n-n}(R) \qquad 2.1.2$$

$$\hat{H}(r,R) = \hat{T}_{nuc} + \hat{H}_{el}(r,R) \qquad 2.1.3$$

In the equation, Hamiltonian can be split into two parts, the first item represents the nuclear kinetic energy operator, and the second part is electronic Hamiltonian operator containing the electronic kinetic energy operator as well as all the coulomb operator involving electrons and nuclei. The electron is treated quantumly, the total electronic wave function is expanded in a complete basis as:

$$\Psi_{el}(r,t) = \sum_j c_j(t)\phi_j\big(r,R(t)\big) \qquad 2.1.4$$

Where $\phi_j\big(r,R(t)\big)$ is a diabatic wave function, and c_j is the complex-valued expansion coefficients. we define matrix elements of the electronic Hamiltonian with respect to the basis functions.

$$V_{ij} = \langle\phi_i(r,R)|H_{el}|\phi_j(r,R)\rangle \qquad 2.1.5$$

Where as before brackets denote integration over electronic coordination only. Nonadiabatic coupling vector can be described as $d_{ij}(R)$:

$$d_{ij}(R) = \langle\phi_i(r,R)|\nabla_R|\phi_j(r,R)\rangle \qquad 2.1.6$$

Where the gradient is defined with respect to the atomic coordinates R, we now assume that atomic motion can be described by some as yet unspecified trajectory.

$$R = R(t) \qquad 2.1.7$$

$R(t)$ is a continuous function of time. classical mechanical equations of motion can be the solution of motion. Some integral method is applied to solve the motion function such as Runge-Kutta and Velocity-Verlet method. In this thesis, only Velocity-Verlet was used, thus the nuclei are treated classically using Velocity-Verlet algorithm:

$$x(t + \Delta t) = x(t) + v(t)\Delta t + \frac{1}{2}a(t)\Delta t^2 \qquad 2.1.8$$

$$v(t + \Delta t) = v(t) + \frac{a(t)+a(t+\Delta t)}{2}\Delta t \qquad 2.1.9$$

Assuming that $\Psi_{el}(r,t)$obeys time-dependent Schrödinger equation:

$$i\hbar\Psi_{el}(r,t) = H_{el}\Psi(r,t) \qquad 2.1.10$$

And substituting Eq4 in Eq10, multiplying with $\phi_j\big(r,R(t)\big)$ and integrating over r gives:

$$i\hbar c_i = \sum_j (V_{ij}\big(R(t)\big) - i\hbar R \cdot d_{ij})c_j(t) \qquad 2.1.11$$

For any given trajectory $R(t)$, this set of coupled differential equations can be integrated numerically to obtain the amplitudes c_i of each electronic state. there are two terms which promote transitions between electronic states, the off-diagonal elements of the electronic Hamiltonian V_{ij} and the nonadiabatic coupling $R \cdot d_{ij}$. The V_{ij} vanish if the electronic basis functions have been defined in adiabatic representation.

Therefore, under the nonadiabaticity framework, the active surface λ can change depending on the rated of change of $|c_\lambda|^2$, it can be shown:

$$-\frac{d|c_\lambda|^2}{dt} = \sum_k \left(2Re(Rd_{\lambda k}c_\lambda^* c_k) - \frac{2}{\hbar}Im(V_{\lambda k}c_\lambda^* c_k)\right) \qquad 2.1.12$$

Each term in the summation in Eq 2.1.12 is interpreted as the rate of population transfer from state λ to state k, given by $2Re(Rd_{\lambda k}c_{\lambda}^{*}c_{k}) - \frac{2}{\hbar}Im(V_{\lambda k}c_{\lambda}^{*}c_{k})$. Using a time step dt much smaller than the time scale of hopping probability during the time interval dt from state λ to state k then is proportional to $\left(2Re(Rd_{\lambda k}c_{\lambda}^{*}c_{k}) - \frac{2}{\hbar}Im(V_{\lambda k}c_{\lambda}^{*}c_{k})\right)dt$. Normalizing with the current population in state λ gives the final hopping probability as:

$$P_{\lambda\to k} = \frac{2Re(Rd_{\lambda k}c_{\lambda}^{*}c_{k}) - \frac{2}{\hbar}Im(V_{\lambda k}c_{\lambda}^{*}c_{k})}{|c_{\lambda}|^{2}}dt \qquad 2.1.13$$

If the hopping probability in Eq 2.1.12 is negative. That would signify a hopping form from state k to state λ. In the spirit of the fewest hops, these hops with negative hopping probability are ignored. Tully's Fewest Switches provides one of the most successful methods to estimate the switching probability.

Landau and Zener studied nonadiabatic transition in atomic collisions and the dissociation of diatomic molecules, which was reduced to a simplified two-state model, it also called the liner curve crossing model. In this model, a nonadiabatic dynamics is approximated as follows:[31] (1) the relevant nuclear motion near the curve crossing point is one-dimensional, which is referred to as the reaction coordinate in the context. The reaction coordinate is denoted as X, which is the displacement from the curve crossing point. (2) diabatic potentials near the crossing point W_1 and W_2 are approximated as linear in X; $W_1 = -F_1X$ and $W_2 = -F_2X$ for state 1 and state 2, respectively. (3) the off-diagonal term in the diabatic representation is approximated as the constant V through the region. (4) during the transition, the system is assumed to move with a constant velocity *v*. in the diabatic representation, the wave functions of the tow electronic state can be represented by $\phi_1(r,X)$ and $\phi_2(r,X)$, respectively. thus, total wave functions are then can be expressed as:

$$\Psi(r,X,t) = c_1(t)\phi_1(r,X) + c_2(t)\phi_2(r,X) \qquad 2.1.14$$

Assumption $X = vt$, then the Schrödinger equation is reduced to a matrix equation:

$$i\hbar\frac{\partial}{\partial t}\begin{pmatrix}C_1(t)\\C_2(t)\end{pmatrix} = \begin{pmatrix}W_1(X) & V\\V & W_2(X)\end{pmatrix}\begin{pmatrix}C_1(t)\\C_2(t)\end{pmatrix} \qquad 2.1.15$$

This equation is to be solved as an initial value problem under the conditions $C_1(-\infty) = 0$ and $|C_2(-\infty)| = 1$. Then the probability of the system undergoing a nonadiabatic transition is given by $P = |C_2(+\infty)|^2$ pre single crossing. The problem is reduced to a second order differential equation, whose solution is given by the Weber function, and Zener obtained the transition probability in the asymptotic namely:

$$P = exp\left[-\frac{\pi}{2\hbar v}\frac{V^2}{|F_1 - F_2|}\right] \qquad 2.1.16$$

Based on two-state *Landau-Zener* liner curve crossing model, *Zhu and Nakamura* was improved Eq 2.1.16[32], and give an improved formula for transition probability valid up to the nonadiabatic transition region expressed as follows:

$$P = exp\left[-\frac{\pi}{4\sqrt{a^2}}\sqrt{\frac{2}{b^2+\sqrt{|b^4 \pm 1|}}}\right] \qquad 2.1.17$$

Where $\pm$ corresponding to the situation of $F_2F_1 > 0$ and $F_2F_1 < 0$. In this algorithm, two linear diabatic potential energy surface curves and constant diabatic coupling are assumed at the avoided point, this switching probability can be formulated in terms of two unitless parameters, namely, effective coupling and effective collision energy as follows:

$$a^2 = \frac{\hbar^2}{2\mu}\frac{\sqrt{|F_2F_1|}|F_2 - F_1|}{(2V_{12})^3} \qquad 2.1.18$$

And

$$b^2 = (E_t - E_X)\frac{|F_2 - F_1|}{\sqrt{|F_2F_1|(2V_{12})}} \qquad 2.1.19$$

In this formula, F_1 and F_2 are the forces on two diabatic potential energy surface, V_{12} is the diabatic coupling, μ is reduced mass of molecular system, E_X is energy at the crossing point and E_t represents the summation of potential energy and kinetic energy

in the direction of the nonadiabatic coupling vector. In principle, Tully's Fewest Switches is a local nonadiabatic transition probability computed at each integration time step along the propagation of trajectory. This means the trajectories can make an attempted hop at any time during the propagation of trajectory. However, Eq 2.1.17 should find the avoided crossing point, then we can calculate the transition probability in the avoided crossing region. it represents an average nonadiabatic transition probability along the trajectories, thus analytical equation 2.1.17 is a global switching probability. Thus, it's similar to the Tully's Fewest Switches, the trajectory surface hopping will occur when this switching probability is greater than a given uniform random number generated between 0 and 1. However, it requires a predetermined seam surface between two adiabatic potential energy surfaces instead of calculating the nonadiabatic coupling vector. Thus, it is difficult to applied for the general diatomic molecule.

In 2014, *Zhu etc*[33]*.,* report a new approach to generalize two parameters in Eq 2.1.18 and Eq 2.1.19, it has applied in chapter 4 of this thesis. The position and velocity in Cartesian coordinates are propagated along the on-the-fly classical trajectories by integrating the Newtonian equation of motion with the velocity-Verlet method. We can detect the minimum adiabatic potential gap form three consecutive time steps; thus, multidimensional forces can be covert into one-dimensional forces in Eq 2.1.18 and Eq 2.1.19:

$$\frac{|F_2-F_1|}{\sqrt{\mu}} = \sqrt{\sum_{i=1}^{N}\frac{1}{m_i}\sum_{\alpha=x,y,z}\left(F_2^{i\alpha}-F_1^{i\alpha}\right)^2} \qquad 2.1.20$$

And

$$\frac{\sqrt{|F_2F_1|}}{\sqrt{\mu}} = \sqrt{\left|\sum_{i=1}^{N}\frac{1}{m_i}\sum_{\alpha=x,y,z}F_2^{i\alpha}F_1^{i\alpha}\right|} \qquad 2.1.21$$

In Eq 2.1.20 and Eq 2.1.21, N is number of nuclei in the molecular system with the m_i mass, and multidimensional diabatic forces can be calculated as:

$$F_1^{i\alpha} = -\frac{\partial V_1}{\partial R_{i\alpha}} \text{and } F_2^{i\alpha} = -\frac{\partial V_2}{\partial R_{i\alpha}} \qquad 2.1.22$$

Where $R_{i\alpha}$ stands for x, y, and z components for the Cartesian coordinates for the *i*th nucleus. Thus, the diabatic potential energy gradient in on-the-fly dynamic simulation along a trajectory can be used to evaluate the multidimensional diabatic forces in Eq 2.1.20 and Eq 2.1.21, it can simply make one linear connection of an upper adiabatic force at t_1 with lower adiabatic force at t_3 and another liner connection of a lower adiabatic force at t_1 with an upper adiabatic force at t_3. Thus, the fitting diabatic forces $F_1^{i\alpha}$ and $F_2^{i\alpha}$ can be calculated as:

$$F_1^{i\alpha}(t) = -\frac{1}{R_{i\alpha}(t_3)-R_{i\alpha}(t_1)} \times \left[\frac{\partial U_-}{\partial R_{i\alpha}(t_3)}\left(R_{i\alpha}(t) - R_{i\alpha}(t_1)\right) - \frac{\partial U_+}{\partial R_{i\alpha}(t_1)}\left(R_{i\alpha}(t) - R_{i\alpha}(t_3)\right)\right] \quad 2.1.23$$

And

$$F_2^{i\alpha}(t) = -\frac{1}{R_{i\alpha}(t_3)-R_{i\alpha}(t_1)} \times \left[\frac{\partial U_+}{\partial R_{i\alpha}(t_3)}\left(R_{i\alpha}(t) - R_{i\alpha}(t_1)\right) - \frac{\partial U_-}{\partial R_{i\alpha}(t_1)}\left(R_{i\alpha}(t) - R_{i\alpha}(t_3)\right)\right] \quad 2.1.24$$

For three consecutive time steps $t_1 < t < t_2$, and U_+, U_- are the adiabatic potential energy surfaces along a trajectory. Diabatic coupling involved in Eq 2.1.18 is given by $2V_{12} = U_+(t) + U_-(t)$, By the above equations, we can calculate two unitless parameters a^2 and b^2 in the Eq 2.1.18 and Eq 2.1.19 at time t along an on-the-fly trajectory only depending on two potential energy surfaces and it gradients. In order to have an accurate fitting diabatic forces in Eq 2.1.21 and Eq 2.1.22, it should take a small integration time step. Moreover, we also need consider the hopping direction for nuclear motion. In this method, it takes a similar concept of Tully's Fewest Switches, where the hopping direction depend on the adiabatic coupling $R \cdot d_{ij}$ because this direction indicates the maximum non-adiabatic transition probability in Eq 2.1.13, thus the hopping direction can be defined by a vector related to two diabatic forces as follows:

$$s_{i\alpha} = \frac{F_2^{i\alpha} - F_1^{i\alpha}}{\sqrt{m_i}} \quad 2.1.25$$

And the normalized vector as:

$$n = \frac{s}{\|s\|} \qquad 2.1.26$$

The relation for classical momentum before and after hopping can be calculated by hopping direct vector n, the momentum could be decomposed into parallel and perpendicular directions expressed as:

$$P_{\|} = (P \cdot n)n \quad \text{and} \quad P_{\perp} = P - (P \cdot n)n \qquad 2.1.27$$

Perpendicular directions momentum is unchanged before and after hopping, thus we can conclude the relationship for parallel directions:

$$P_{\perp}(U_{+}, t) = P_{\perp}(U_{-}, t) \qquad 2.1.28$$

And

$$E_t = U_{+}(t) + \sum_{i=1}^{N} \frac{P_{i\|}(U_{+},t)}{2m_i} = U_{-}(t) + \sum_{i=1}^{N} \frac{P_{i\|}(U_{-},t)}{2m_i} \qquad 2.1.29$$

Where $P_{i\|}(U_{+}, t)$ and $P_{i\|}(U_{-}, t)$ is the momentum components on the upper and lower adiabatic potential surfaces at time t. then a simple scaling factor can be obtained from Eq 2.1.29 to rescale the change of parallel components of momentum. Finally, we can calculate the transition probability by this method, and it should note that if a^2 is large than 1000, the transition probability should set up to unity (1, diabatic limitation) and if b^2 is smaller than 0.001, it should be zero (0, diabatic limitation)[33], when $1000 > a^2 > 0.001$ the Eq 2.1.17 is actually preformed.

2.2 Wavefunction method

In above description of nonadiabatic dynamic simulation, we have introduced two type method that was used to compute the transition probability with the propagation along trajectories. Moreover, stationary electronic structure also needed in the nonadiabatic dynamics simulation. Thus, it is necessary to introduce the electronic structure method involved in thesis. The need for multiconfigurational method is often

motivated by an interest in systems where the electronic structure is not well-described by single determinant method. Any chemical reaction involves mixing the electronic wave function of the reactant and product and a large part of the reaction pathway should be better described by using more than one electronic configuration. Nonadiabatic reactions that involve conical intersection between an excited state and the ground state or states with significant double-excitation character should be studied with multireference methods. For nonadiabatic dynamic simulation, it is essential to computing nuclear gradients and derivative coupling by using multiconfigurational method[34] whatever in Tully's Fewest Switches-based methods or Zhu-Nakamura-based surface hopping. the framework of multireference theory aims at a generalization of construction of the electronic wave function beyond the single reference method. In principle, the concept is consisting of two types: (1) the multireference character is considered by a set of configurations as references, this aims primarily at the resolution of Quasi-degeneracies regarding orbitals and strongly coupled configurations (usually termed nondynamic, static or strong electron correlation)[35]. (2) orbital excitations from those references are constructed to improve the flexibility of the wave function, which is meant to include the remaining electron correlation as is done in the single reference configuration method. Basically, the methods can be divided into the ones that are based on multiconfigurational self-consistent field (MCSCF)[36–38] and multireference configuration interaction (MRCI)[39–42] and ones that based on perturbation theory (MRPT)[43–46]. A third area has emerged in more recent year which combines multireference approaches with DFT, specifically, the multiconfiguration pair-density function theory (MC-PDFT)[47–54]. And, some new algorithms have developed in recent years, including the density matrix renormalization group (DMRG)[55,56] method and full configuration interaction quantum Monte Carlo (FCIQMC)[57,58], which has attracted more and more attention the rapidly evolving fields. MCSCF and MRPT method has involved in the thesis, thus we just introduce them here.

In order to describe the MCSCF and MRPT method, we start from a review of full configuration interaction (FCI) method. The total electronic wave functions can be expressed as a linear combination of many-electron basis function $|\phi_i\rangle$:

$$|\Psi\rangle = \sum_i c_i|\phi_i\rangle \qquad 2.2.1$$

Where the many-electron functions $|\phi_i\rangle$ are construct from molecular orbitals (MOs) either by means of individual determinants or as configuration state functions (CSFs). The latter are eigenfunctions of the spin operator $\hat{s}^2$ and $\hat{s}_z$ by construction. The MOs must be computed before preforming an SCF or by any other appropriate method[35]. The FCI Hamilton matrix can be constructed by above process. If the configuration interaction expansion of the wave function includes all possible electronic configuration, the exact energies for a given basis set are calculated by diagonalization of the Hamiliton matrix using some iterative procedures. However, because of the highly computation cost of evaluating the complete determinant expansion, FCI just can be performed on small basis set and molecules. Therefore, it is essential to develop the approximation of FCI method.

The MCSCF method is a variational procedure, which is based on the expansion of the expansion of the wave function in Eq 2.2.1, and both the CI coefficients and MOs are optimized. The situation is more difficult when several electronic states should be described at the same time. In this case, state average multiconfigurational self-consistent field (SA-MCSCF) is usually performed, in which the average energy of several states is optimized to obtain a balanced description of these state. The MCSCF method can be used as an approach of its own for calculating several electronic states of a molecule, but also as a procedure that only to create the Mos needed in the correlated multireference calculation for defining the many-electron expansion function $|\phi_i\rangle$ and to compute the Hamiltonian matrix H.

A popular choice for the wave function used in the MCSCF methods is the complete

active space multiconfigurational self-consistent field (CASSCF). In this method, all possible configurations in a given orbital space and for a given number of electrons are constructed. It is essentially an FCI approach in the restricted space of active orbitals and electrons. Thus, the CAS is invariant under purely activate orbital rotations. This space is usually characterized as CAS (n electrons, n orbitals). Because of the factorial increasing of the size of the CAS with the number of active orbitals, this method also has a high computational cost when the target molecule with a large scale and large basis set. In principle, it is difficult to determine the actual size of these spaces because there are no straightforward rules on how to determine these spaces. Thus, when CASSCF method was performed in the calculation, it is better to recognize the orbital related to the excited state reaction or nonadiabatic process by visualizing the molecular orbitals (MOs) of target molecules. However, MCSCF method does not include dynamical correlation. So, the most accurate way to include multireference effects is to start with MCSCF and add dynamical correlation through configuration interaction (MRCI) or perturbation theory (MRPT) approaches.

For multireference perturbation theory (MRPT), the application of perturbation theory in a contracted way to zero order wave function at the complete activate space level was developed by *Roos, etc.* giving rise to CASPT2[59], and implemented in OpenMolcas[60,61] and Molpro[61] package. it is the most widely used approach in high accurate method to deal with the excited state reaction. Although CASPT2 is very useful for describing excited state with the inclusion of both dynamical and dynamical correlation[35], it is problematic around conical intersections since it uses perturbation theory correct one state at a time. The multistate CASPT2 (MS-CASPT2) was developed later, which considers coupling between states, and it thus more appropriate for conical intersections between excited states. In CASPT2, the reference wave function is an optimized MCSCF wave function. In most cases a CASSCF wave function can be for a single state or a state-averaged one. However, these methods are often much more

expensive, so until recently, in practice optimizations and dynamics were mostly done using CASSCF.

2.3 DFT method

Density functional theory (DFT) is widely used on ground state electronic calculation, couched in terms of the electronic density distribution[62] $n(r)$. Since its birth, it has become increasingly useful for the understanding and calculation of ground state chemical property of the molecular system, including ground electronic density, energy, and chemical reaction mechanism, etc. moreover, it also has been applied for solid matters, and large-scale materials[63–73]. Basically, DFT depends on the adequate knowledge of the exchange correlation energy function $E_{xc}[n(r)]$, and though more and more accurate forms are constantly being developed, there is no know systematic way to achieve a high level of accuracy. Here, we just simply introduce the basic concept of the fundamentals of DFT. The Schrödinger equation can be described as:

$$H\Psi = E\Psi \qquad 2.3.1$$

We assume that N nonrelativistic interacting electron with Hamiltonian as:

$$H = -\sum_i \frac{1}{2}\nabla_i^2 - \sum_{iA}\frac{Z_A}{|r_i - r_A|} + \sum_{i>j}\frac{1}{r_{ij}} \qquad 2.3.2$$

The aim is to simply minimize the energy over all possible antisymmetric wave functions,$\Psi(x_1, x_2, x_3, \dots, x_N)$ for number of electrons N. where x_i contains the spatial coordinate r_i and spin coordinate σ_i, this enables us to find the minimizing Ψ and energy *E*. the basic foundation of DFT is the Hohenberg-Kohn theorem, which states that external potential is a functional of the ground state density. Thus, a relationship has been constructed between electronic density and interaction about the molecular system. In Kohn-Sham (KS) theory, the electron density of the KS reference systems is given by[63]:

$$\rho(r) = \sum_i |\phi_i|^2 \qquad 2.3.3$$

And ground sate energy is expressed:

$$E[\rho] = T_s[\rho] + V_{ne}[\rho] + J[\rho] + E_{XC}[\rho] \qquad 2.3.4$$

Where $T_s[\rho]$ is kinetic energy:

$$T_s[\rho] = \sum_i \left\langle \phi_i \middle| -\frac{1}{2}\nabla^2 \middle| \phi_i \right\rangle \qquad 2.3.5$$

The nucleus electron potential energy, expressed in terms of the external potential due to the nuclei $v(r) = -\sum_A Z_A/(|r - R_A|)$.

$$V_{ne}[\rho] = \int \rho(r)v(r)dr \qquad 2.3.6$$

And the classical electron-electron repulsion energy is:

$$J[\rho] = \frac{1}{2}\iint \frac{\rho(r)\rho(r')}{|r-r'|}drdr' \qquad 2.3.7$$

For the remaining term exchange-correlation functional $E_{XC}[\rho]$, it can be expressed in the constrained search formulation for density functionals.

$$E_{XC}[\rho] = (T[\rho] - T_s[\rho]) + (V_{ee}[\rho] - J[\rho] \qquad 2.3.8$$

However, it is difficult to get the exact formalism of $E_{XC}[\rho]$ in Eq 2.3.8, there are many densities functional approximations has been developed for practical applications, which can be classify into three aspects. First is the simplest is local density approximation (LDA), the form of exchange part is given by:

$$E_x^{LDA}[\rho] = -\frac{3}{4}\left(\frac{3}{\pi}\right)^{1/3} \int \rho^{4/3}\, dr \qquad 2.3.9$$

While the functional for correlation was not derived from first principles, instead Monte Carlo simulation of the uniform gas. The LDA assumes that the density is the same everywhere, which tends to underestimate the exchange energy and overestimate the correlate energy. In order to correct for this error, it is common to expand in the terms of the gradient of the density to account for the non-homogeneity of the true electron density. Thus, generalized gradient approximation (GGA) as second type densities functional

approximations was proposed by researcher. For exchange part, takes the simple form of PBE:

$$E_X^{PBE} = -\int \rho^{4/3} \left[\frac{3}{4}\left(\frac{3}{\pi}\right)^{1/3} + \frac{\mu s^2}{1+\mu s^2/\kappa}\right] dr \qquad 2.3.10$$

In order to get more accurate exchange and correlation energy, Meta-generalized gradient approximation (Meta-GGA) include higher-order derivatives of the density Meta-GGA can give a form $E_{XC}^{MGAA} = \int \rho^{4/3} F(\rho(r), \nabla\rho(r), \nabla^2\rho(r), \tau(r) \ldots)\, dr$, including the kinetic energy density $\tau = \frac{1}{2}\sum_i |\nabla\phi_i|^2$. Moreover, some functionals contain parts of Hartree-Fock exchange type terms and uses all the orbitals (both occupied and virtual)[74].

2.4 OM2/MRCI method

Quantum-chemical ab initio method provide a convergent path to the exact solution of the Schrödinger equation and can therefore give more accurate answer for chemical reaction such as above introduction of DFT. However, because of the high computational cost, it is difficult to applied for largescale molecular system. Quantum-chemical semiempirical method are the simplest variant of electronic theory, involving integral approximations and parameterizations that limit their accuracy but make them very efficient, so that it can be utilized in a relatively large system.

Orthogonalization models OM2[75] and OM2/MRCI[76] method have been performed in this thesis, we thus, will introduce the OM2 simply here. In matrix notation, the basic equations of the model are as follows:

$$\Psi = C\phi \qquad 2.4.1$$

$$FC = CE \qquad 2.4.2$$

$$F = H + G(P) \qquad 2.4.3$$

They start out from an *ab inito* formalism and then introduce rather assumptions to speed

up the calculations, typically by neglecting many of less important terms in the Eq 2.4.3 Fock matrix. Orthogonalization corrections is included in the one electron terms and two-center one-electron terms, which employ the HF SCF-MO[77] treatment for the valence electrons with a minimal basis set of contracted Gaussian functions (STO-3G for hydrogen and ECP-3G for carbon, nitrogen, oxygen, and fluorine). These Empirical parameters are incorporated into the formalism and calibrated against reliable experimental or theoretical reference data to avoid the errors caused by those approximations. Based on the configuration of Hartree-Fock equation performed using OM2 calculation level, the excited state configuration can be defined and get the MRCI configuration by the linear combination of the obtained configuration.

2.5 Dimensionality reduction method

In computer science, datasets with many characteristics are called high-dimensional data, it has also received increasing attention from people. Massive and complex data contains a lot of useful information, but it also increases the difficulty to use the data effectively, and it also discover the essential characters of the data. For example, the problem called the "curse of dimensionality" appears due to the rapid and large-scale expansion of dimensions. Thus, researcher of computer science proposed a kind of method namely dimensionality reduction, which is a method for representing a given dataset using a lower number of features (dimensions), while still capturing the original data's meaningful properties[78].

In the mathematical sense, suppose there is a n-dimensional vector:

$$X = [x_1, x_2, \dots x_n] \qquad 2.5.1$$

X are mapped to m-dimensional vector Y through a map f:

$$Y = [y_1, y_2, \dots y_m] \qquad 2.5.2$$

And $m \ll n$, vector Y should contain the main features of vector X. Mathematically, the mapping function can be expressed as:

$$Y = f(X) \qquad 2.5.3$$

This process of feature extraction and selection can help people capturing the important features of the date sets. This mapping f is the algorithm that we want to find for feature reduction. The choice of mapping f differs depending on the pending problem.

The dimensionality reduction methods are divided into two categories: linear and nonlinear, Linear methods are easier to calculate than nonlinear and they can be parse. However, many of the problems are related to nonlinear and time-varying systems, which attracts more and more attention. Principal component analysis (PCA)[79] and classical multi-dimensional scaling (CMDS)[78] are the most widely used linear algorithms, PCA allows the original complex variable to be represented by several integrated factors that reflect the information contained in the original variable as much as possible, and these factors do not relate to each other, to achieve the purpose of simplification. if there are n samples, the number of indicators measured by a single sample is p , so there are total of np data, but the indicators usually interact with each other, and the PCA is to study how to find the principal components from the indicators. the goal of CMDS is to find the multidimensional data projections in the lower-dimensional space (2- dimension or 3-dimension) to maintain the similarity or inconsistency of the data. Steps of the CMDS algorithm includes construct the distance matrix D according to original data sets, calculating the inner product matrix B, and then calculating the eigenvalues $\lambda_1 \geq \lambda_2 \geq \cdots \lambda_n$ and eigenvector of B matrix. the new space can be constructed by product eigenvector and corresponding eigenvalue. It can be seen from above description that the CMDS and PCA are essentially the same, the difference is that the CMDS is based on the sample, and the PCA is based on variables. The Nonlinear dimensionality reduction methods such as isometric map (ISOMAP)[80], local linear embedding (LLE)[81], can re-set a set of data of dimensional space with some geometric features in low-dimensional space.

In this thesis, CMDS was involved, the details can reference the specific chapter.

Chapter 3 Theoretical study of $SiCH_4$

3.1 Introduction

Silaethylene and its derivatives are studied for their potential in creating new materials with unique electronic and mechanical properties[82,83]. It serves as a useful intermediate for synthesizing more complex organosilicon compounds[83,84], which have applications in pharmaceuticals[85], agrochemicals, and advanced materials. Also, it can participate in various chemical reactions, including cycloadditions and insertions, making it an important intermediate in organosilicon chemistry. Understanding the behavior of silaethylene can contribute to the development of new catalytic processes[86], particularly in the field of silicon-based organic synthesis.[87]

The dynamics of photoexcited π-bond is a very interesting and important phenomenon. In this context ethylene (C_2H_4) has been studied extensively including detail investigations of the characteristics of its reaction path, conical intersections and dynamics on these surfaces[88–90]. Silaethylene, formally known as silene, and represented by the molecular formula $H_2Si{=}CH_2$, is a chemical compound where one of the carbon atoms in ethylene (C_2H_4) is replaced by a silicon atom. This compound belongs to the broader class of organosilicon compounds, which are characterized by silicon atoms bonded directly to carbon atoms. Silaethylene ($H_2Si{=}CH_2$) features a double bond between a silicon atom and a carbon atom. In this structure, silicon (Si) forms a double bond with carbon (C),which is similar to the carbon-carbon double bond in ethylene. Thus, the properties of silicon-carbon double bonds are of considerable interest, as evidenced by large numbers of experimental and theoretical investigations, many of these studies

concentrated on the question of the strength of Si=C double bond in comparison to the C=C double bond in the ethylene. By estimating the heats of formation and the relative stability of silaethylene versus, *Walsh* et al. concluded that the C=C double bond is weaker than the Si=C double bond[91–93]. In order to give more information on the excited state of silaethylene, *Pitonak* et al. has a systematic studied of the energy surfaces, including the vertical excitations, equilibrium geometry, conical intersections and the comparation results between ethylene and silaethylene at multireference configuration interaction calculations with singles and doubles (MR-CISD) level. according to their result, there are four pathway was investigated and it is expected that after Frank-Condon excitation to the excited state, the conical intersection is immediately reached and rapid radiationless transition to the ground state will occur. However, such a mechanism does exist in the ethylene[94]. Then, *Zechmann* et al. has explored the excited sate dynamics process of silaethylene by the surface hopping combined with multireference configuration interaction methods. The evolution of the S_0 and S_1 state were investigated during the first 100(fs) after photoexcitation. In contrast to expectations based on previous static calculation of potential energy surface, two mechanisms were found, corresponding to torsion and pyramidalization paths. In their calculation, state-average multiconfiguration self-consistent filed (SA-CASSCF) and multireference configuration interaction with single and double excitation (MR-CISD) calculation were carried out for the ground state and the S_1 state of silaethylene. A CAS (2,2) complete activate space was chosen and the three states calculation at the MCSCF/6-31g* level had equal weights. Two distinct mechanisms for the relaxation from Franck-Condon region of the S_1 state to the ground state. these two different mechanisms mainly due to the CSi stretching mode[95]. However, the different reaction was recognized in other same type of photodynamic processes such as $CH_2NH_2^+$[96], C_2H_3F[97], and the research of silylenemethyl radical[98]. In previous studies, a small CAS space was chosen to perform the static calculation and dynamics. although, the MR-CISD method can consider more configuration correlation compared to SA-

CASSCF and can give more accurate result. The small CAS space may lead an incomplete identification of the mechanisms for understanding the photodynamic of silaethylene.

In this study, the reaction route map of silaethylene on the ground is explored using the using the ADDF method at B3LYP/def2-svp, six different paths have been searched, including two dissociation reaction paths and four proton-transform paths. then the photodynamic of silaethylene was investigated by means of Zhu-Nakamura based method surface hopping dynamics at MS-CASPT2/def2-svp level and six different paths was recognized.

3.2 Computational Details

The global switching trajectory surface hopping method have been performed to treat surface hopping occurred at an avoided crossing point adjacent adiabatic potential energy surface, usually located at conical intersection region. The global switching probability is calculated by Zhu-Nakamura-based Landau-Zener formula[99], as follows:

$$P = exp\left[-\frac{\pi}{4\sqrt{a^2}}\sqrt{\frac{2}{b^2+\sqrt{|b^4\pm 1|}}}\right] \qquad 3.2.1$$

In which a^2 is the effective nonadiabatic coupling constant and b^2 is effective collision energy, these two constants can be defined as:

$$a^2 = \frac{\hbar^2}{2\mu}\frac{\sqrt{|F_1F_2|}|F_1-F_2|}{(2V_{12})^3} \qquad 3.2.2$$

and

$$b^2 = (E_t - E_X)\frac{|F_2F_1|}{\sqrt{|F_1F_2|}(2V_{12})} \qquad 3.2.3$$

Where F_1 and F_2 are forces along two diabatic potential energy surface, the diabatic coupling V_{12} can be directly calculated by the difference between two adiabatic potential energy surfaces at avoided crossing region, μ represents the reduced mass of a diatomic molecule, E_t is the summation of potential energy and kinetic energy component along hopping vector direction, E_x is the potential energy at crossing point. It is noted that ± in

Eq 3.2.1 corresponds to $F_1F_2 > 0$ or $F_1F_2 < 0$.

3.3 Results and Discussion

3.3.1 The reaction route for $SiCH_4$

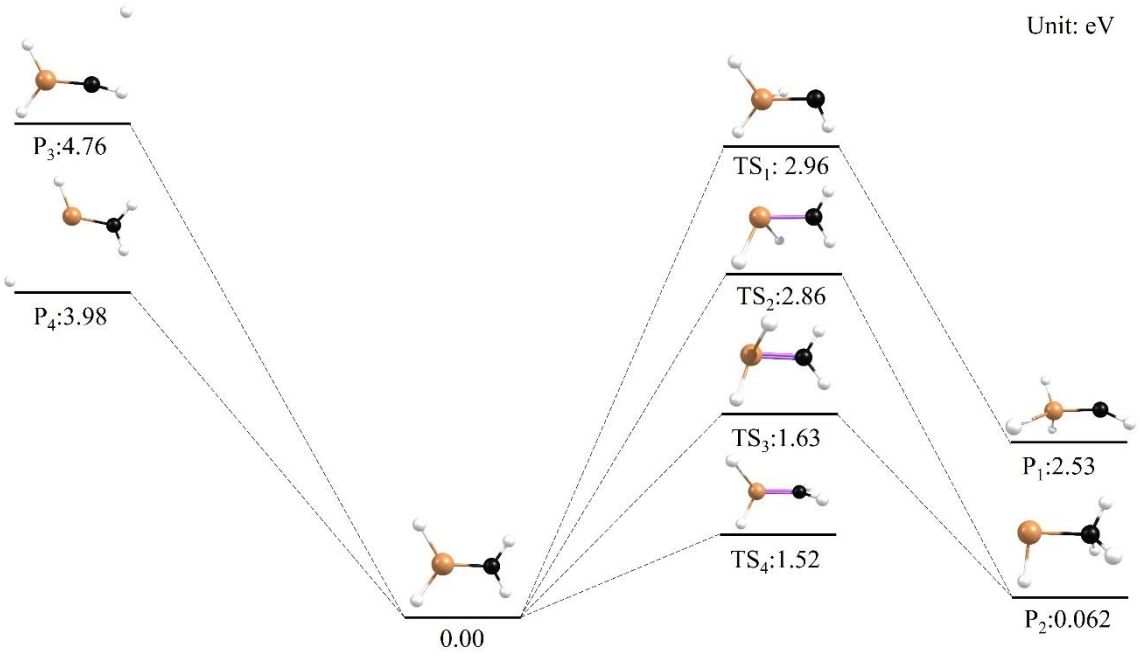

Figure 3.1 the reaction pathway on ground state of $SiCH_4$, including four TSs, two proton-transform products P_1 and P_2, dissociative products P_3 and P_4.

To systematically investigate the possible reaction pathways through electronic excited state for the photochemical reaction of $SiCH_4$, the $SiCH_4$ of minima and transition state geometries were located on the ground state potential energy surface by combining with ADDF[100] and IRC calculations with B3LYP-D3 functionals and def2-svp basis set using Gaussian16 and developmental version of GRRM23.[101] **Figure 3.1** shows the reaction path for $SiCH_4$ where two products (P_1, P_2) are connected by four TSs. Three TSs (TS_1, TS_2, TS_3) are recognized that proton transform, which are examined by analyzing of frequencies. it is noted that planar reactant undergoes isomerization around

Si=C bond, passing through the TS_4 before reverting back to the original reactant. Moreover, two new dissociation pathways also have been explored by GRRM program[101], the original reactant is branched into two pathways due to the breaking of C=H bond and Si=H bond, formatting two dissociative products P_3 and P_4. Furthermore, the electronic structure calculations were carried out by active space (8,8) mulit-state second-order perturbation theory (MS-CASPT2) methods[102] with def2-svp basis set, using the OpenMolcas program package.[103] **Figure 3.2** shows relative energies of related electronic state of $SiCH_4$, the dissociative products CH_2+SiH_2, H+CH=SiH_2, CH_2=SiH+H, and the proton-transfer products CH=SiH_3, CH_3=SiH at CASPT2/def2-svp level. With the consideration of related electronic state of $SiCH_4$, planar reactant is prompt to first excited state from ground state at FC region roaming in the environment with 5.60 eV of excitation energy differ to experimental value of 4.83 eV, excited $SiCH_4$ molecules then is decay to ground state products. **Figure 3.3** shows molecular orbital at equilibrium geometry of ground state at MS-CASPT2 level. The π orbital and σ orbital is involved in activate space so that all possible reaction pathway can be considered in calculation.

In fact, on further optimization, three conical intersections are also located by OpenMolcas program at CASSCF/def2-svp between S_0 and S_1.There are three types of photochemical reaction processes, after exciting to the S_1 state form FC region, One of pathway is that excited $SiCH_4$ molecules dissociate into two cations CH_2^+ and SiH_2^+.Two pathways involve the excited $SiCH_4$ molecules dissociating into two dissociative products H+CH=SiH_2, CH_2=SiH+H with the breaking of C=H and Si=H bonds. The potential curves obtained though linear interpolation coordinate and spanning from equilibrium geometry to a distance of 4.0 Å, are illustrated in **Figure 3.4 (a) and Figure 3.4 (b)**. as the distance between C=H and Si=H bonds increase, two adjacent diabatic potential surface become degenerate, potentially leading to non-diabatic transitions during the photochemical dissociation process. Another two pathways involve excited $SiCH_4$ molecules undergoing proton-transfer from C atom and Si atom, respectively. the

potential curves obtained through linear interpolation coordinates, extending from the equilibrium geometry to a conical intersection, and subsequently proceeding to another equilibrium geometry, are depicted in **Figure 3.4 (c) and Figure 3.5 (d)**. A third pathway involves the excited $SiCH_4$ molecules decaying to original ground state reactant by rotating the CH_2 and SiH_2 around C=Si bond. The potential curves obtained through linear interpolation coordinate, rotating along the torsional dihedral angle H-C-Si-H form equilibrium geometry to a conical intersection, and subsequently undergoing to another isomer, are displayed in the **Figure 3.4 (e).**

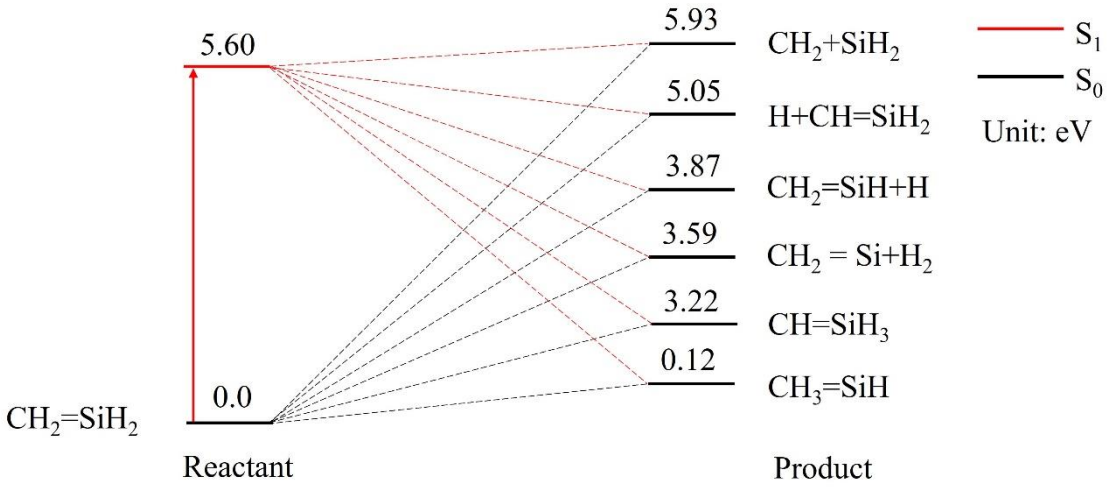

Figure 3.2 Relative energies of the electronic states of $SiCH_4$ and dissociative products CH_2+SiH_2, H+CH=SiH_2, CH_2=SiH+H, CH_2=Si+H_2, CH=SiH_3, CH_3=SiH at CASPT2/def2-svp level.

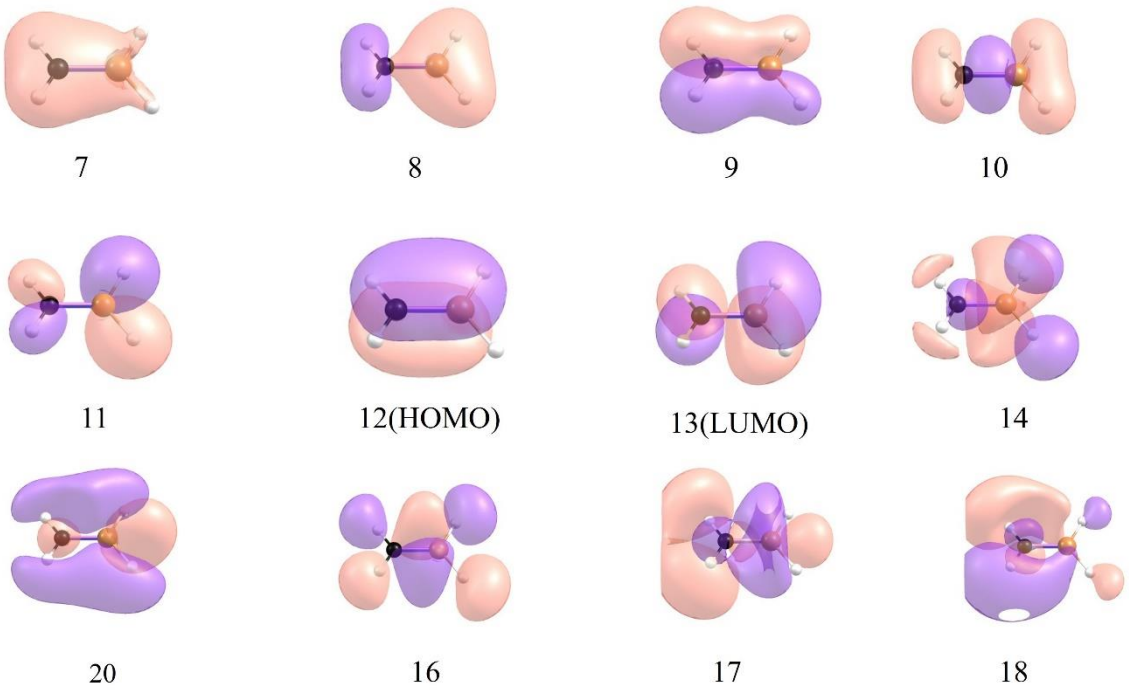

Figure 3.3 The natural orbitals of $SiCH_4$, from orbital 9 to orbital 16, are selected as the active orbitals.

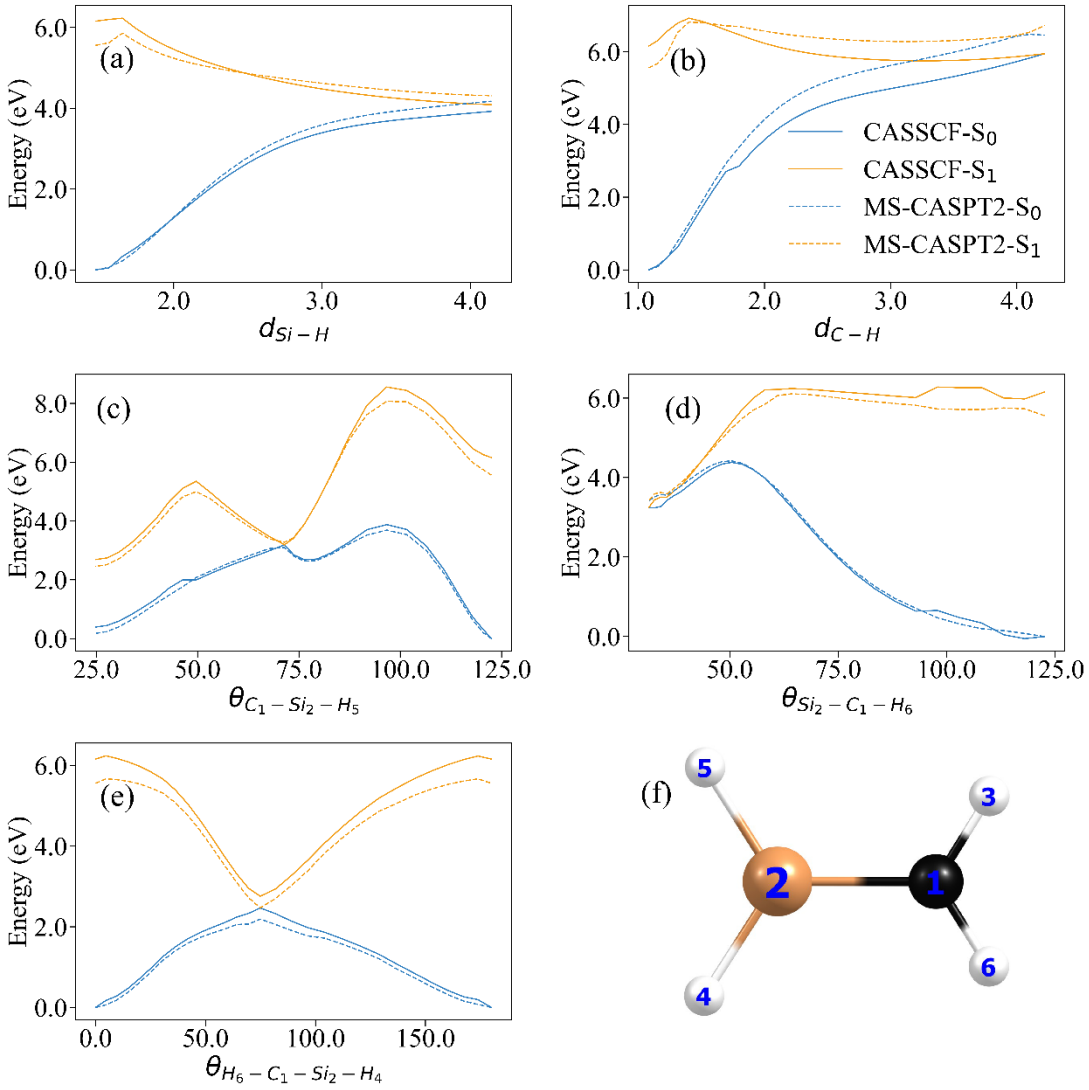

Figure 3.4 (a) Si-H dissociation starting from the equilibrium geometry to the distance of 4.0 Å. Energies are relative to the equilibrium geometry. (b) C-H dissociation starting from the equilibrium geometry to the distance of 4.0 Å. Energies are relative to the equilibrium geometry. (c) proton-transfer string from the C_1 to Si_2 (d) proton-transfer string from the Si_2 to C_1 (e) the rotation of $\theta_{H6\text{-}C1\text{-}Si2\text{-}H4}$ from 0° to 180° at MS-CASPT2/def2-svp level. (f) the equilibrium geometry of SiCH4 with key atoms labeled by number.

3.3.2 Surface hopping AIMD simulation for dissociation process

Trajectory surface hopping (TSH) simulation were systematically program to explore the photoisomerization process of $SiCH_4$. State-averaged complete activate space multiconfigurational self-consistent filed (SA-CASSCF) and multireference second-order perturbation (MS-CASPT2) method with def2-svp basis set were carried out for ground state(S_0) and first excited state(S_1) of silaethylene ($SiCH_4$). A CAS (8,8) complete activate space was chosen and two states calculated at the SA-CASSCF and MS-CASPT2 level with equal weights. All energies, gradients and nonadiabatic coupling vectors were calculated with the OpenMolcas package.[103] Initial conditions were generated by winger distribution at 0 K. In total 500 trajectories were performed at MS-CASPT2 level, a period of 100 fs was chosen for each trajectory with a time step 0.5 fs.

First of all, surface hopping AIMD simulations were conducted using both Tully's fewest-switch surface hopping (FSSH) and Zhu-Nakamura surface hopping (ZNSH) algorithm at SA-CASSCF/def2-svp level. The Tully's FSSH code was executed using the sharc program[104], while the ZNSH code was implemented using pymd, a program developed internally. **Figure 3.5 (a)** illustrates the population of S_1/S_0 of $SiCH_4$ obtained from FSSH at the SA-CASSCF/def2-svp level, where 400 trajectories were simulated, resulting in an approximate lifetime of 30.5 fs, on the other hand, **Figure 3.5 (b)** displays the population of S_1/S_0 of $SiCH_4$ obtained from ZNSH at the SA-CASSCF/def2-svp level, with 500 trajectories simulated, and an estimated lifetime of approximately 30.5 fs. Moreover, as can be seen that the shape of the population of FSSH is similar to ZNSH result. Consequently, the ZNSH algorithm implemented in pymd is reliable according to obtained from FSSH at SA-CASSCF/def2-svp level.

With consideration of the dynamical correlation effects, we ran 500 trajectories string form the S_1 excited state at MS-CASPT2/def2-svp level. 4 trajectories can be classified into any pathway, thus,496 trajectories were included to estimate the branching ratio. Among them, 101 trajectories did not decay to the ground state account for 20%,

$SiCH_4$ dissociate into two cations CH_2^+ and SiH_2^+ in 10 trajectories (2%), into dissociative products H+CH=SiH_2 in 43 trajectories (9%), into dissociative products CH_2=SiH+H in 157 trajectories (32%). For the proton-transfer products CH=SiH_3 and CH_3=SiH in 10 trajectories (2%) and 23 trajectories (5%), respectively. Furthermore, in the photoisomerization of $SiCH_4$, the rotation of SiH_2 and CH_2 around the alkene Si=C skeleton was observed in 143 trajectories, accounting for 29% of the total trajectories. The $SiCH_4$ also from the products of CH_2 = Si+H_2 account for 2%, the detail of branching ratio is summarized in the **Table 3.1** Based on the simulated trajectories, **Figure 3.5 (c)** displays the population of S_1/S_0 of $SiCH_4$, with 500 trajectories simulated, and a computed lifetime of approximately 48.5 fs.

To deeply understand the overall photochemical mechanism of $SiCH_4$ in details, the potential energy as function of time for seven example trajectories is presented in **Figure 3.6**. The changes of potential energy of two cations CH_2^+ and SiH_2^+ along a propagation trajectory combined with the variation of distance between Si and C atom is presented in **Figure 3.6 (a)**. as can be seen, with the dissociation of CH_2^+ and SiH_2^+, the distance between Si and C atom gradually increases from around 1.8 Å to more than 2.4 Å, while the diabetic potential energy surface is approaching until surface hopping occurs at t=96.5 fs ($S_1 \rightarrow S_0$), the trajectory eventually reaches the ground state, which can be regarded as the dissociation of dissociation of CH_2^+ and SiH_2^+ pathway.

For dissociative products H+CH=SiH_2 and CH_2=SiH+H, the changes of potential energy along example combined with the variation of distance between Si-C is presented in **Figure 3.6 (b)** and **Figure 3.6 (c)**. with the progradation of trajectory, the distance between C-H, Si and H atom as function of time is shown beside potential energy curves. The molecules run on the excitation potential energy surface after prompting to S_1 excited state. During the propagation of trajectory, Si-H and C-H distance increases from their initial stage. Molecules then decay to ground at 92.0 fs and 93.5 fs. For formation of CH_2 = Si+H_2, the changes of potential curves illustrate in the **Figure 3.6 (d)**, the distance of

H_4-H_5, Si-H_4 and Si-H_5 as function of time is shown beside potential curves, the distance of Si-H_4 and Si-H_5 increase from around 3.0 Å to around 4.0 Å, while the distance of H_4-H_5 decreases from around 3.0 Å to around 1.0 Å, which can be considered as CH_2 = Si+H_2 pathway. The surface hopping occurs at 63.0 fs. For proton-transfer products CH=SiH_3 and CH_3=SiH, the change of potential energy combined with the variation of angle $\theta_{Si2\text{-}C1\text{-}H3}$ and $\theta_{C1\text{-}Si2\text{-}H3}$ is shown in **Figure 3.6 (e)** and **Figure 3.6 (f)**. The angle $\theta_{Si2\text{-}C1\text{-}H3}$ and $\theta_{C1\text{-}Si2\text{-}H3}$ gradually decreases, eventually decay to ground state at 22.5 fs and 48.0 fs, respectively. For photoisomerization pathway, then change of potential energy is presented in **Figure 3.6 (g)**, with the propagation of example trajectories, the dihedral $\theta_{H4\text{-}Si2\text{-}C1\text{-}H6}$ increases from negative to positive degree, While the molecule back to ground state at 86.0 fs. Thus, overall products of $SiCH_4$ can be observed in the Zhu-Nakamura surface hopping simulation.

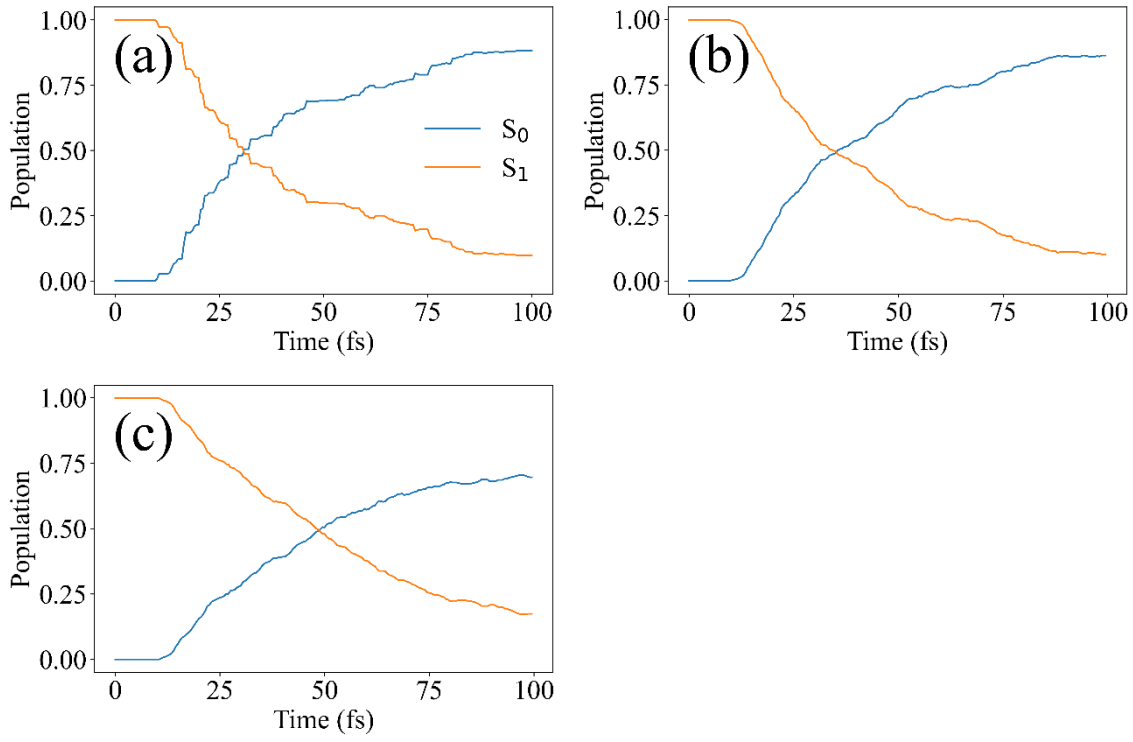

Figure 3.5 (a) the electronic state population of SiCH4 at SA-CASSCF/def2-svp using Tully's fewest-switch method in sharc program package, (b) at SA-CASSCF/def2-svp using Zhu-Nakamura method in our program (c) at MS-CASPT2/def2-svp using Zhu-Nakamura method in our program.

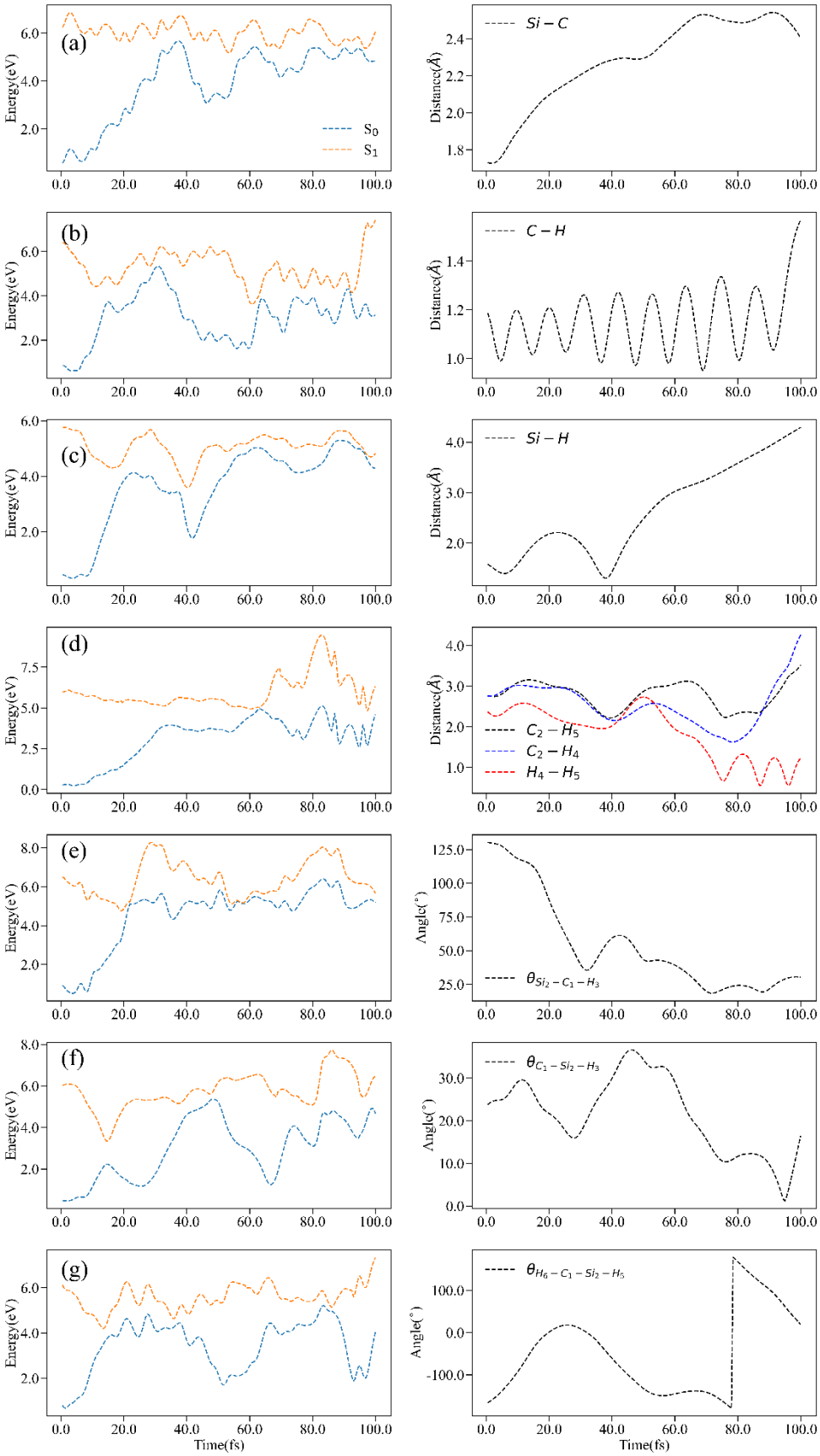
(a)
Energy(eV)
S_0
S_1
Distance(Å)
$Si-C$
(b)
$C-H$
(c)
$Si-H$
(d)
C_2-H_5
C_2-H_4
H_4-H_5
(e)
Angle(°)
$\theta_{Si_2-C_1-H_3}$
(f)
$\theta_{C_1-Si_2-H_3}$
(g)
$\theta_{H_6-C_1-Si_2-H_5}$
Time(fs)

Figure 3.6 (a) typical trajectory of Si-H dissociation (b) typical trajectory of C-H dissociation (c) typical trajectory of proton-transfer string from the C_1 to Si_2 (d) typical trajectory of proton-transfer string from the Si_2 to C_1 (e) typical trajectory of rotation of $\theta_{H6\text{-}C1\text{-}Si2\text{-}H4}$ from 0° to 180° (f) the equilibrium geometry of SiCH4 with key atoms labeled by number. (f)

Table 3.1 The branching ratio of various products at MS-CASPT2/def2-svp

	MS-CASPT2	
CH_2+SiH_2	10	0.02
H+CH=SiH_2	43	0.09
CH_2=SiH+H	157	0.32
CH_2 = Si+H_2	7	0.01
CH=SiH_3	10	0.02
CH_3=SiH	23	0.05
CH_2=SiH_2	143	0.29
other	4	
No Hopping	101	0.2
total	500	

3.4 Conclusions

In this study, ab initio dynamics simulation has been carried out for the multi-channel excited state reaction of $SiCH_4$ at the MS-CASPT2 level to calculate the branching ratio of the dissociative and proton-transform path. The Zhu-Nakamura method is employed to calculate the transition of the electronic state along the propagation of trajectory.

The complete the reaction pathway on the ground state, including four proton-transform paths and two dissociative paths. 500 trajectories are simulated with the initial condition that Wigner sampling is given to the respective normal vibrational modes of

$SiCH_4$ with random phases, and the molecule is stimulated to the S_1 state of $SiCH_4$. The rates of the respective dissociative products are estimated as CH_2=SiH+H (0.32), H+CH=SiH_2 (0.09), while the proton-transform products are CH=SiH_3 (0.02) and CH_3=SiH (0.05). this displays that our simulation with consideration of large CAS space (CAS (8,8)) and more dynamic correlation of MS-CASPT2 confirm more reaction channels. We believe that this work may deepen the insight and understanding of the photodynamic process of $SiCH_4$.

Chapter 4 Theoretical design of molecular motors

4.1 Introduction

Molecular motors[105–107] have the remarkable ability to induce mechanical rotation through precise movements of their constituent components, triggered by electronic or chemical stimuli, particularly the influence of light. The prospect of harnessing light as a potent energy source for molecular motors has garnered growing interest in recent years. This interest stems from the unique advantages of light-driven molecular motors (LDMRMs), where specific wavelengths of light can control their operation without the need for physical contact or dependence on the surrounding environment, all while minimizing the generation of waste byproducts.[4,5] LDMRMs operate through the photoisomerization of the alkene framework, with the two molecular motor subcomponents connected by a double C=C or C=N bond, enabling them to absorb activating light and achieve a full 360° rotation.[108–111]

Most LDMRMs traditionally rely on ultraviolet (UV, 100-400 nm) or visible (400-750 nm) light for their excitation. This approach comes with several drawbacks: UV light is undesirable for constructing nodular photoresponsivity systems;[107] UV light is less than ideal for constructing compact photoresponsive systems, and it can be detrimental to materials prone to degradation, while also posing a risk to cell health due to

photoreactions in some cellular components.[112] Consequently, shifting the absorption band of the chromophore to the visible or near-infrared region of the electromagnetic spectrum has become a central concern within the LDMRM field. Various strategies have been explored to achieve a redshift of the excitation wavelength for well-established LDMRMs. Among these approaches, the most effective is believed to be the fine-tuning of the highest occupied molecular orbital (HOMO) - lowest unoccupied molecular orbital (LUMO) band gap through structural modifications of the molecular motor. In 2003, the Feringa group introduced a groundbreaking concept by proposing a donor-acceptor functionalized LDMRM, enabling the absorption of photons at 430 nm through the introduction of a push-pull system in the lower half of the molecular motor, facilitating photoisomerization.[113] More recently, Leeuwen and colleagues[114] introduced a class of LDMRMs based on the push–pull system. The incorporation of a benzofluorenyl moiety into a standard molecular motor resulted in a considerable bathochromic shift, with λ_{max} transitioning from 395 nm of the parent motor to 420 nm due to enhanced π-conjugation. Pfeifer *et al.*[115] further delved into the structural redesign of the second-generation LDMRM based on a push–pull system, achieving an even more pronounced redshift in the maximum absorption wavelength by altering substituents in the stator and rotor. In their study, three push-pull motors and a tricyano-substituted motor (1s, 2s, 6s refer to **Figure 4.1**) were prepared, allowing for a comparative analysis of the impact of push-pull substitution on π-system extension by the CN-group in 6s.[115] The results revealed maximum absorption wavelengths of 422 nm (1s), 453 nm (2s), and 421 nm (6s), with quantum yields ranging from approximately 0.15~0.12. These findings underscore the potential for achieving a redshift in absorption wavelength through strategic structural design, such as the introduction of substituent groups[12,13].

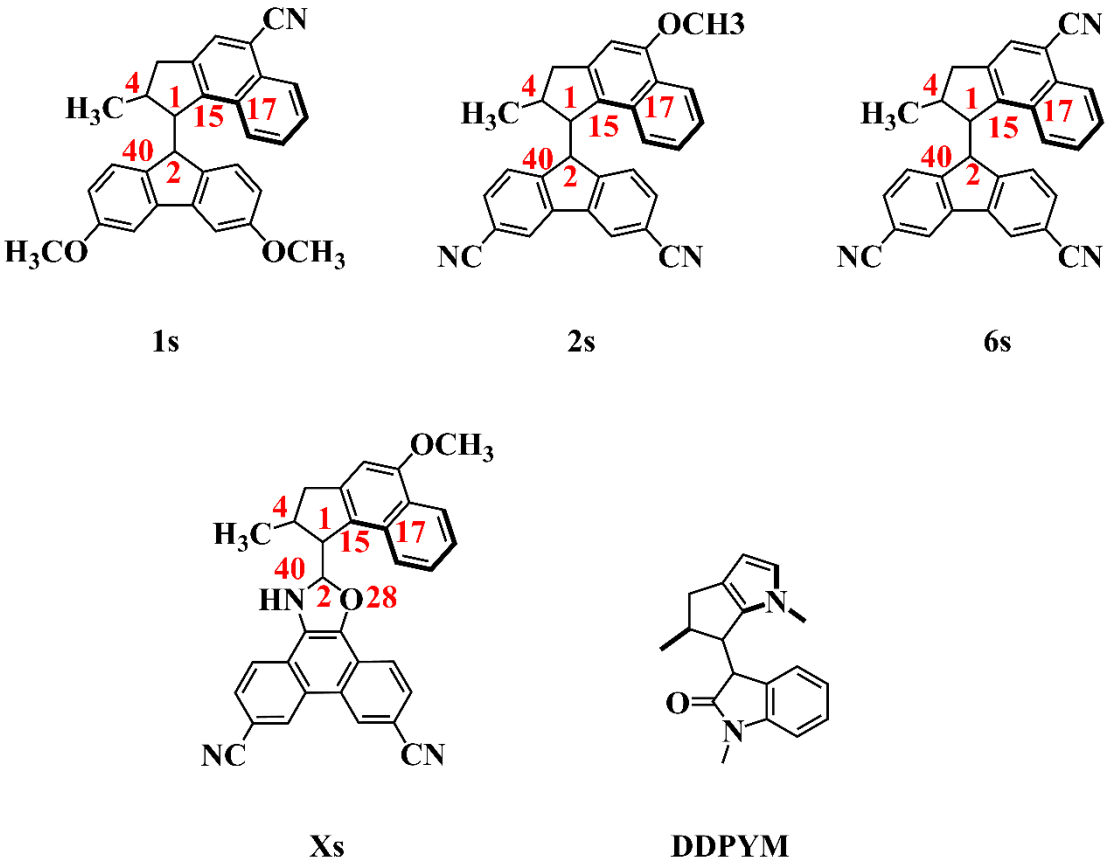

Figure 4.1 The geometry of rotary motor 1s, 2s, 6s, and the newly designed Xs, as well as DDPYM. Some atoms are labelled by red numbers.

Feringa-type molecular motors exist in two main configurations: 4-stroke (involving two steps of photoisomerization coupled with two steps of thermal helix inversion (THI)),[116,117] and 2-stroke (consisting of two photoisomerization steps only).[118] The timescales for the photoisomerization and THI steps span from nanoseconds to days and femtoseconds to picoseconds, respectively.[119,120] The rotation speed of a designed LDMRM is influenced by all the constituent steps in its rotation cycle, and the high energy barrier associated with the THI step hinders the overall rotation speed of LDMRMs. Hence, there exists considerable potential for enhancing the rotation speed by reducing the THI barrier.[107] Recently, a new family of fulgide-based LDMRMS was reported by Filatov *et al.*[121] They investigated the dynamics properties of these prototype molecules using a combination of quantum chemical calculations and trajectory surface hopping

(TSH) simulations with Tully's fewest switches algorithm.[122] The TSH method is a highly effective technique for exploring the elementary processes of excited-state dynamics by calculating potential gradients through electronic structure calculations to determine the forces acting on atoms, deriving classical trajectories through numerical solutions of Newton's equations of motion, and considering transitions between electronic states due to non-adiabatic couplings.[123,124] Theoretical simulations predicted a quantum efficiency of 0.55~0.68 for these prototype molecules, an ultrafast dynamics timescale of 200 to 300 fs, and a thermal helix potential barrier of 13.6 kcal/mol.

Several new designs of LDMRMs have been theoretically proposed to augment the rotation speed by minimizing the THI step. Filatov *et al.*[125] reported a new class of 2-stroke LDMRM capable of 360° rotation by reengineering the rotor blades and combining two photoisomerization steps. The TSH simulations predicted a photoisomerization process taking place within a timescale of 200 to 300 fs, demonstrating a notably high quantum yield of approximately 0.91-0.97. García-Iriepa *et al.*[126] proposed a 2-stroke photoreaction-only LDMRM that eliminates the THI step and achieves rapid rotation by introducing a chiral hydrogen bond environment. More recently, Ma *et al.*[127] introduced a new 3-stroke LDMRM capable of a full 360° rotation in two photoisomerization steps and one THI step, named DDIYs. TSH simulations at the semi-empirical OM2/MRCI level predicted ultrafast timescales (0.1 to 0.3 fs) for the two photoisomerization steps. They also designed an oxindole-based LDMRM, DDPYM,[128] with a push–pull character and minimal steric hindrance near the rotation axis, leading to faster and more concentrated electronic decay of the S_1 excited state compared to its parent molecule.

Consequently, significant research endeavors have been dedicated to shifting the absorption wavelength of molecular motors into the visible spectrum while upholding rotation speed and quantum yield. Drawing inspiration from the oxindole-based LDMRM, we introduce a new category of 4-stroke light-driven molecular motors, denoted as 2-((2S)-5-methoxy-2-methyl-2,3-dihydro-1H-cyclopenta[a]naphthalen-1-yl)-3-oxo-2,3-

dihydro-1H-dibenzo [e, g] indole-6,9-dicarbonitrile, or simply "Xs" (refer to **Figure 3.1**). Our molecule design draws from the second-generation LDMRMs established by Pfeifer *et al.*,[115] focusing on tuning the HOMO-LUMO energy gap and minimizing the THI barrier. This adaptation enables a 360° rotation that encompasses two-step photoisomerization (EP to ZM and ZP to EM) and two-step thermal helix inversion. The primary aim was to conduct a comprehensive assessment of key attributes, including the UV-visible (UV-vis) spectrum, time-resolved fluorescence emission spectrum, the THI barrier, quantum yield, and average lifetime. These comparative analyses allowed us to evaluate and validate the performance of the designed LDMRM. Furthermore, we conducted a detailed comparative analysis with a recently conceived oxindole-based LDMRM named "DDPYM" (refer to **Figure 3.1**). We believe that this innovatively designed LDMRM will serve as a catalyst for further experimental and theoretical research in this domain.

4.2. Computational Details

The equilibrium and transition state structures of LDMRMs 1s, 2s, 6s, and Xs in the ground state were optimized, and normal mode analyses were conducted through DFT calculations employing B3LYP-D3, CAMB3LYP-D3, M06-2X, and ωB97XD functionals along with 6-31G(d,p) basis sets. Additionally, the geometry optimization for isomers EP and ZP was carried out at the PBE0-D3/6-31G(d,p) level. UV-vis absorption spectra were calculated using TD-DFT at the same computational level. All DFT and TD-DFT calculations were executed using the Gaussian09 program.[129]

The OM2/MRCI method, recognized for its computational efficiency and accuracy in exploring excited state dynamics, has been widely used in the investigation of photochemical reactions,[130–141] as evident in benchmark papers.[142–146] In this study, the OM2/MRCI method, implemented in the MNDO99 program,[147] was utilized for excited-

state calculations and dynamics simulations of LDMRMs 1s, 2s, 6s, and Xs. The Lagrange-Newton approach[148] facilitated the identification of S_1/S_0 minimum energy conical intersections (MECIs) along the photoisomerization pathways. Multireference configuration interaction (MRCI) calculations were conducted for three reference states, encompassing the closed-shell ground-state, and single and double excitations from HOMO to LUMO. Considering the characteristics of ππ* electronic excitations and the convergence of the optimizations for MECIs, we selected active spaces (8,9), (10,10), (8,8), and (8,8) for the three substituent molecular motors, 1s, 2s, 6s, and Xs, respectively, in the OM2/MRCI calculations. To ensure the persistence of π orbitals within the active space throughout the calculation process, we identified and tracked the π-type population (PIPOP) using a threshold of 0.4.

The TSH simulations were conducted for molecular motors within the framework of the OM2/MRCI method utilizing Tully's fewest-switches algorithm.[122] Initial conditions were generated by the ground state equilibrium structure, with atomic velocities randomly distributed according to a Wigner distribution at 300 K. Geometries were selectively chosen using the filtering approach integrated into the MNDO program.[147] In this filtering approach, transition probabilities are calculated for structures generated via Wigner sampling, and structures are then selected as initial conditions based on a comparison between these transition probabilities and random numbers.[149] Wigner sampling is based on harmonic normal modes, and when it includes low-frequency modes, it samples structures that deviate from the equilibrium configuration. This can be problematic because in the actual potential energy surfaces of molecular systems, the effects of anharmonicity and mode coupling contribute, which reduces the accuracy of structural sampling along low-frequency modes. A simple workaround is to exclude these low-frequency modes from the sampling. However, more precise methods such as the quantum thermostat technique have been devised recently, and comparisons between these methods and experimental data are being made.[150] Although the molecular system

in the current study includes low-frequency modes, the purpose of the TSH simulations using OM2/MRCI is qualitative rather than quantitative, so we used conventional Wigner sampling to set the initial conditions. To enhance accuracy, the empirical decoherence correction proposed by Granucci *et al.*[151] (0.1 au) was applied. The Newton equation of motion was resolved employing a time step of 0.1 fs through the velocity-Verlet algorithm,[152] while the time-dependent electronic Schrödinger equation was solved with a time step 100 times smaller.

4.3 Results and discussion

4.3.1 Structures and potential energy profiles for molecular motor

Concerning the geometries of 1s, 2s, 6s, and Xs, we adopt the helicity definition proposed by Karnik *et al.*[153] According to conformation and helicity, two equilibrium geometries of different parent molecules, 1s, 2s, and 6s, are denoted as P and M, while four equilibrium geometries of Xs are labeled EP, ZM, ZP, and EM. **Figure 3.1** depict the most stable geometries for 1s,2s,6s, DDPYM (P) and Xs (EP), respectively. Supplementary **Figures 3.3, 3.5, 3.7,** and **3.9** present all stable geometries of 1s, 2s, 6s, and Xs, with corresponding structural parameters calculated at different levels outlined in **Tables 3.2, 3.5, 3.8, and 3.11**. It is evident that results from various calculation levels are in agreement with each other. The dihedral angles C_{40}-C_2-C_1-C_{15} and C_2-C_1-C_{15}-C_{17} are employed to characterize the steric bulkiness in the fjord region for 1s-P, 2s-P, 6s-P, Xs-EP, and Xs-ZP. Tables S1, S2, S3 and S4 (refer to ESI) indicate that the dihedral angles for 1s-P, 2s-P, 6s-P are all smaller than those for Xs-EP and Xs-ZP, suggesting that the steric bulkiness in the fjord region is less pronounced for Xs-EP and Xs-ZP compared to 1s-P, 2s-P and 6s-P.

Figures 4.2, 4.4, 4.6 and 4.8 illustrate schematic diagrams of potential energy profiles for the rotation cycle of the molecular motors 1s, 2s, 6s and Xs, respectively. **Table 4.13**

presents the calculated energy barriers for 1s, 2s, 6s (between M and P), and Xs (between ZM and ZP and between EM and EP) in the ground state, calculated using the OM2/MRCI method. The optimized transition state geometries are depicted in **Figures 4.3, 4.5, 4.7 and 4.9**, and corresponding structural parameters are provided in **Tables 4.2, 4.5, 4.8, and 4.11**. The OM2/MRCI results align well with those obtained through DFT calculations. As depicted in **Figures 4.2, 4.4, 4.6, and 4.8**, the molecular motor undergoes photoexcitation to the FC region (P isomer for 1s and EP and ZP isomers for Xs). Subsequently, the molecular motor rotates counterclockwise around the C=C double bond, decaying to the ground state via S_1/S_0 CIs, and eventually reaching stable M isomers for 1s, 2s, 6s and ZM or EM isomers for Xs. Over time, the stable M isomers of 1s, 2s, 6s and ZM or EM isomers of Xs traverse the THI barrier and isomerize to P' of 1s, 2s, 6s and ZP of EP isomers for Xs. **Table 4.13** reveals that the relative values of THI barriers for 1s, 2s, 6s, and Xs are consistent regardless of the method used. The THI barriers of the newly designed molecular motor Xs are notably lower than those of 1s, 2s, and 6s, suggesting a potentially higher rotational speed for Xs compared to 1s, 2s, and 6s. In comparison to DDPYM, the THI barriers of Xs are higher than DDPYM between ZM and ZP, while THI barriers between EM and EP are lower. This implies that the rotational speed of Xs may differ from DDPYM depending on the specific isomerization pathway, with Xs being faster for EM to EP and potentially slower for ZM to ZP.

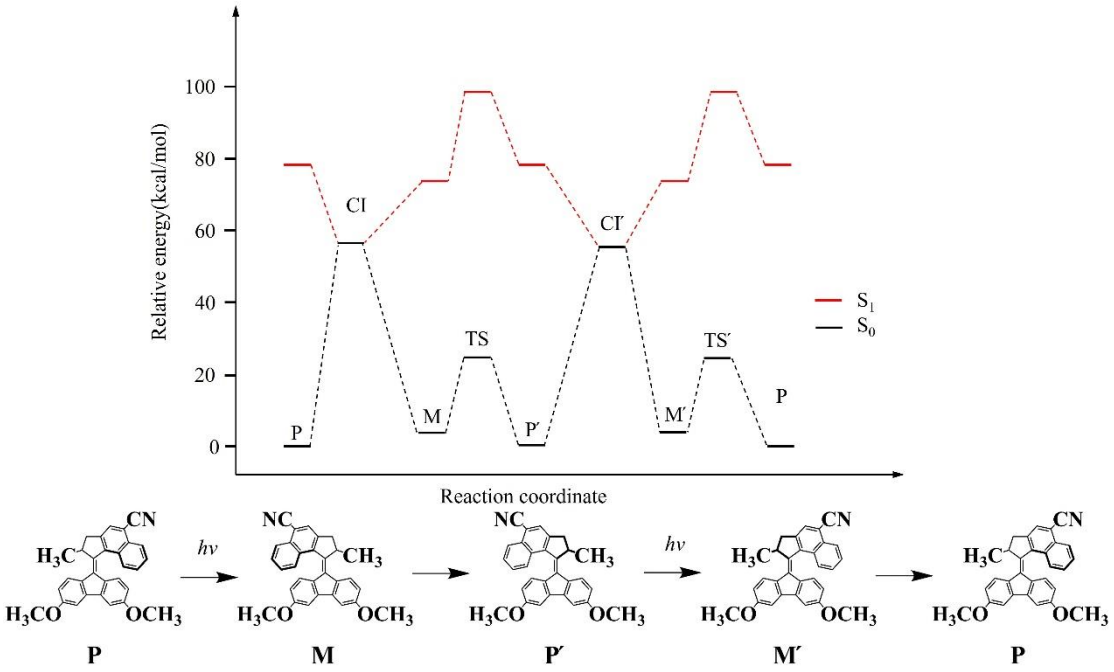

Figure 4.2 The energy profiles of S_0 and S_1 states of a rotation cycle for the molecular motor 1s (P → M→ P' → M' → P) at the OM2/MRCI level; CI and TS denote conical intersection and transition state, respectively.

Table 4.1 Energies of the relevant structures in the ground state for 1s, calculated by the OM2/MRCI method (in eV), and by the B3LYP-D3, CAMB3LYP-D3, M06-2X, and wB97XD methods with 6-31G(d,p) basis sets (in Hartree). The energies relative to P are also given in parenthesis (in kcal/mol).

	OM2/MRCI	B3LYP-D3	CAMB3LYP-D3	M062X	ωB97XD
P	-5045.166	-1362.32954	-1361.56497	-1361.70764	-1361.82290
M	-5045.081	-1362.32354	-1361.55784	-1361.70076	-1361.81584
	(2.0)	(3.8)	(4.5)	(4.3)	(4.4)
TS	-5044.222	-1362.28838	-1361.52354	-1361.66602	-1361.78155
	(21.8)	(25.8)	(26.0)	(26.1)	(26.0)

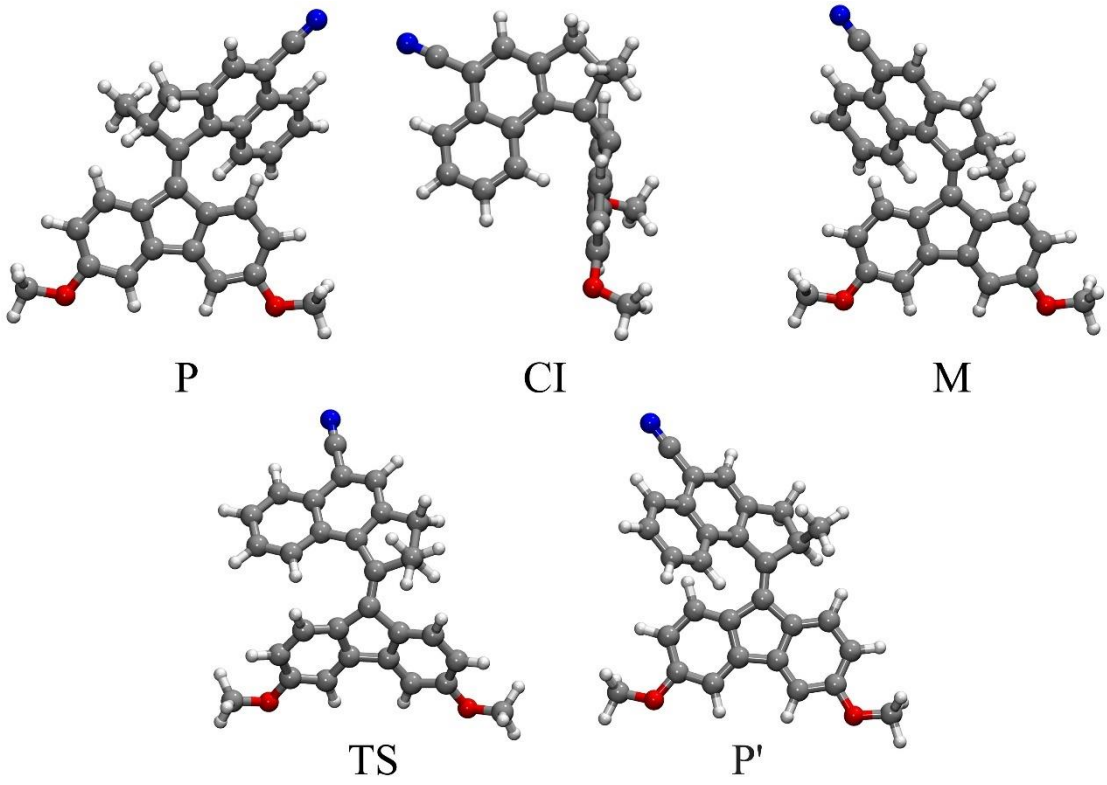

Figure 4.3 Optimized structures of minima, one conical intersection, and one transition state along the reaction pathway of molecule 1s calculated at the OM2/MRCI level.

Table 4.2. Geometrical parameters of optimized equilibrium and transition state structures in the ground state for 1s, calculated by the OM2/MRCI method, using the MNDO99 program,[147] and by B3LYP-D3, CAMB3LYP-D3, M06-2X, and ωB97XD methods with 6-31G(d,p) basis sets, using the Gaussian09 program.[129] The bond lengths are given in Å, while bond angles and dihedral angles are given in degrees.

		OM2/MRCI	B3LYP-D3	CAMB3LYP-D3	M06-2X	ωB97XD
P	C1-C2	1.35804	1.36772	1.3547	1.35744	1.35552
	C40-C2-C1	126.9	126.535	126.386	126.096	126.427
	C2-C1-C4	125.904	124.632	124.769	124.59	125.032
	C40-C2-C1-C4	21.785	21.118	20.416	19.829	20.451
	C40-C2-C1-C15	-170.138	-169.548	-170.758	-170.663	-171.08
	C2-C28-C40-C1	-0.527	-1.359	-1.35	-1.507	-1.365
	C2-C1-C15-C17	40.462	40.548	41.468	40.602	42.032
M	C1-C2	1.36331	1.3761	1.36139	1.36391	1.36196
	C40-C2-C1	127.978	127.949	128.215	128.366	128.128

	C2-C1-C4	124.41	124.504	125.061	124.928	125.402
	C40-C2-C1-C4	147.441	145.218	146.286	146.458	145.783
	C40-C2-C1-C15	-25.392	-29.015	-27.457	-26.842	-27.091
	C2-C28-C40-C1	-1.381	-1.183	-1.202	-1.38	-1.275
	C2-C1-C15-C17	-26.879	-27.786	-29.552	-29.826	-30.36
TS	C1-C2	1.36446	1.38357	1.36968	1.37336	1.37064
	C40-C2-C1	120.986	122.114	121.732	121.299	121.68
	C2-C1-C4	117.947	117.969	117.835	117.555	117.85
	C40-C2-C1-C4	-24.731	-24.094	-22.119	-21.646	-22.346
	C40-C2-C1-C15	142.51	139.727	144.791	145.794	144.687
	C2-C28-C40-C1	-9.315	-8.102	-8.168	-8.204	-8.312
	C2-C1-C15-C17	19.901	23.183	22.516	20.848	22.417
P'	C1-C2	1.35804	1.36772	1.3547	1.35744	1.35552
	C40-C2-C1	127.6	128.319	128.66	128.724	128.576
	C2-C1-C4	125.903	124.632	124.769	124.59	125.032
	C40-C2-C1-C4	-156.883	-155.427	-156.12	-156.326	-156.049
	C40-C2-C1-C15	11.203	13.907	12.706	13.182	12.419
	C2-C28-C40-C1	0.526	1.359	1.35	1.507	1.365
	C2-C1-C15-C17	40.461	40.548	41.468	40.602	42.032

Table 4.3. Geometrical parameters of the CI structure between S_0 and S_1 states for 1s calculated by the OM2/MRCI method. The bond lengths are given in Å, while bond angles and dihedral angles are given in degrees.

CI	C1-C2	1.41331
	C40-C2-C1	96.940
	C2-C1-C4	115.996
	C40-C2-C1-C4	-112.117
	C40-C2-C1-C15	54.979
	C2-C28-C40-C1	-35.041
	C2-C1-C15-C17	19.312

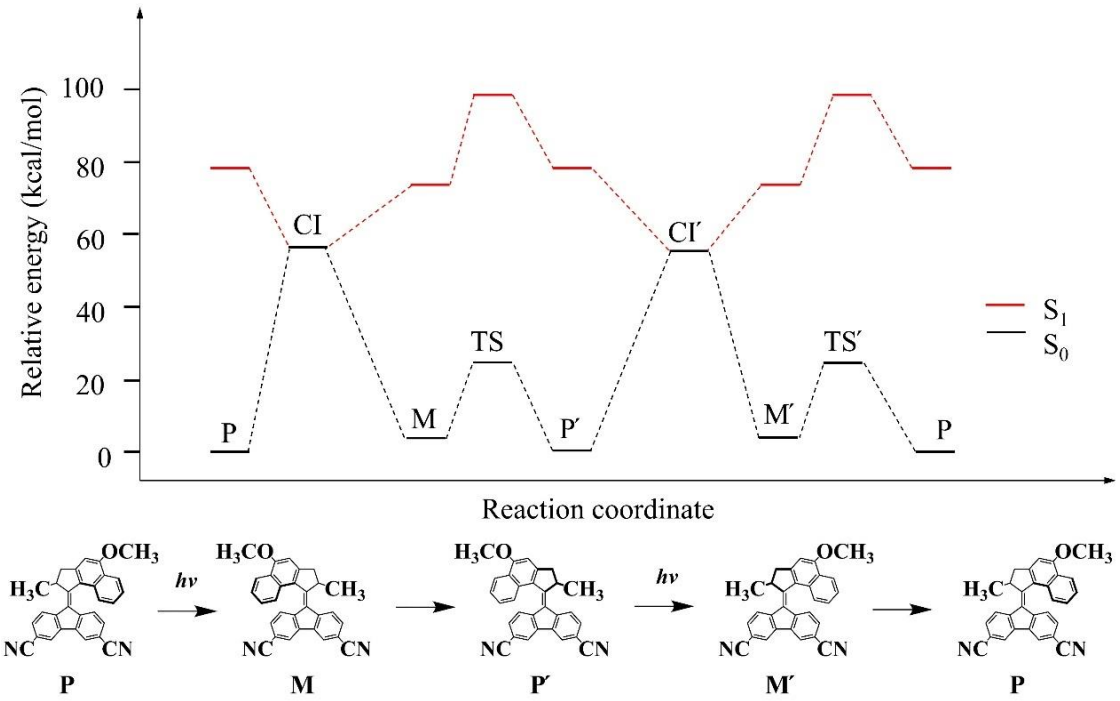

Figure 4.4 The energy profiles of S_0 and S_1 states of a rotation cycle for the molecule 2s (P → M→ P' → M' → P) at the OM2/MRCI level; CI and TS denote conical intersection and transition state, respectively.

Table 4.4 Energies of the relevant structures in the ground state for 2s, calculated by the OM2/MRCI method (in eV), and by the B3LYP-D3, CAMB3LYP-D3, M06-2X, and ωB97XD methods with 6-31G(d,p) basis sets (in Hartree). The energies relative to P are also given in parenthesis (in kcal/mol).

	OM2/MRCI	B3LYP-D3	CAMB3LYP-D3	M062X	ωB97XD
P	-4882.130	-1340.04773	-1339.28776	-1339.44615	-1339.54261
M	-4882.057 (1.7)	-1340.04351 (2.7)	-1339.28239 (3.4)	-1339.44095 (3.3)	-1339.53729 (3.3)
TS	-4881.165 (22.3)	-1340.00606 (26.2)	-1339.24581 (26.3)	-1339.40409 (26.4)	-1339.50077 (26.3)

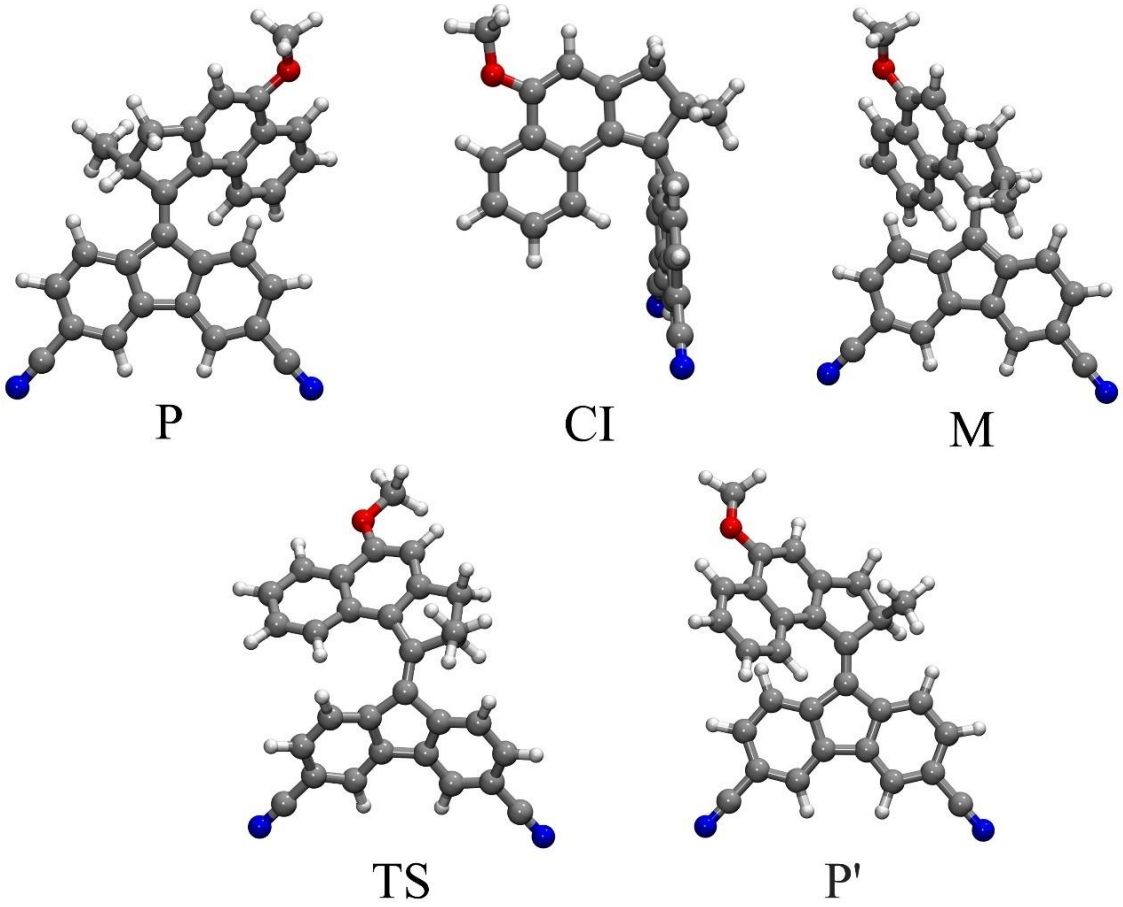

Figure 4.5 Optimized structures of minima, one conical intersection, and one transition state along the reaction pathway of molecule 2s calculated at the OM2/MRCI level.

Table 4.5 Geometrical parameters of optimized equilibrium and transition state structures in the ground state for 2s, calculated by the OM2/MRCI method, using the MNDO99 program,[147] and by B3LYP-D3, CAMB3LYP-D3, M06-2X, and ωB97XD methods with 6-31G(d,p) basis sets, using the Gaussian09 program.[129] The bond lengths are given in Å, while bond angles and dihedral angles are given in degrees.

		OM2/MRCI	B3LYP-D3	CAM-B3LYP-D3	M06-2X	ωB97XD
P	C1-C2	1.36244	1.37408	1.36111	1.36373	1.36217
	C40-C2-C1	127.136	126.811	126.682	126.466	126.733
	C2-C1-C4	125.498	124.365	124.468	124.204	124.61
	C40-C2-C1-C4	21.189	21.188	20.288	19.633	20.533
	C40-C2-C1-C15	-169.491	-167.68	-168.969	-169.132	-168.652
	C2-C28-C40-C1	-0.94	-1.486	-1.542	-1.686	-1.297

	C2-C1-C15-C17	39.236	37.796	38.809	37.881	38.548
M	C1-C2	1.367	1.38365	1.3698	1.37196	1.37077
	C40-C2-C1	127.561	127.504	127.705	127.775	127.747
	C2-C1-C4	124.112	123.731	124.076	123.962	124.088
	C40-C2-C1-C4	146.833	144.009	145.301	145.919	145.078
	C40-C2-C1-C15	-26.653	-30.574	-29.107	-28.197	-28.967
	C2-C28-C40-C1	-1.713	-1.343	-1.319	-1.293	-1.425
	C2-C1-C15-C17	-26.159	-25.278	-26.561	-26.616	-26.635
TS	C1-C2	1.37	1.39052	1.37641	1.37956	1.37751
	C40-C2-C1	121.347	121.658	121.385	121.007	121.391
	C2-C1-C4	117.714	117.878	117.644	117.349	117.701
	C40-C2-C1-C4	-25.973	-25.947	-24.752	-23.953	-25.633
	C40-C2-C1-C15	140.72	139.347	142.667	143.871	141.809
	C2-C28-C40-C1	-9.361	-9.179	-9.323	-9.34	-9.508
	C2-C1-C15-C17	19.445	21.305	20.293	19.016	19.298
P'	C1-C2	1.36243	1.37408	1.36112	1.36373	1.36217
	C40-C2-C1	127.214	127.734	128.023	128.027	127.944
	C2-C1-C4	125.499	124.365	124.468	124.204	124.61
	C40-C2-C1-C4	-156.435	-155.071	-155.798	-156.111	-156.18
	C40-C2-C1-C15	12.872	16.061	14.945	15.125	14.636
	C2-C28-C40-C1	0.949	1.486	1.543	1.687	1.297
	C2-C1-C15-C17	39.256	37.796	38.809	37.88	38.547

Table 4.6 Geometrical parameters of the CI structure between S_0 and S_1 states for 2s calculated by the OM2/MRCI method. The bond lengths are given in Å, while bond angles and dihedral angles are given in degrees.

CI	C1-C2	1.41136
	C40-C2-C1	116.416
	C2-C1-C4	118.624
	C40-C2-C1-C4	-115.421
	C40-C2-C1-C15	61.837
	C2-C28-C40-C1	-25.085
	C2-C1-C15-C17	3.152

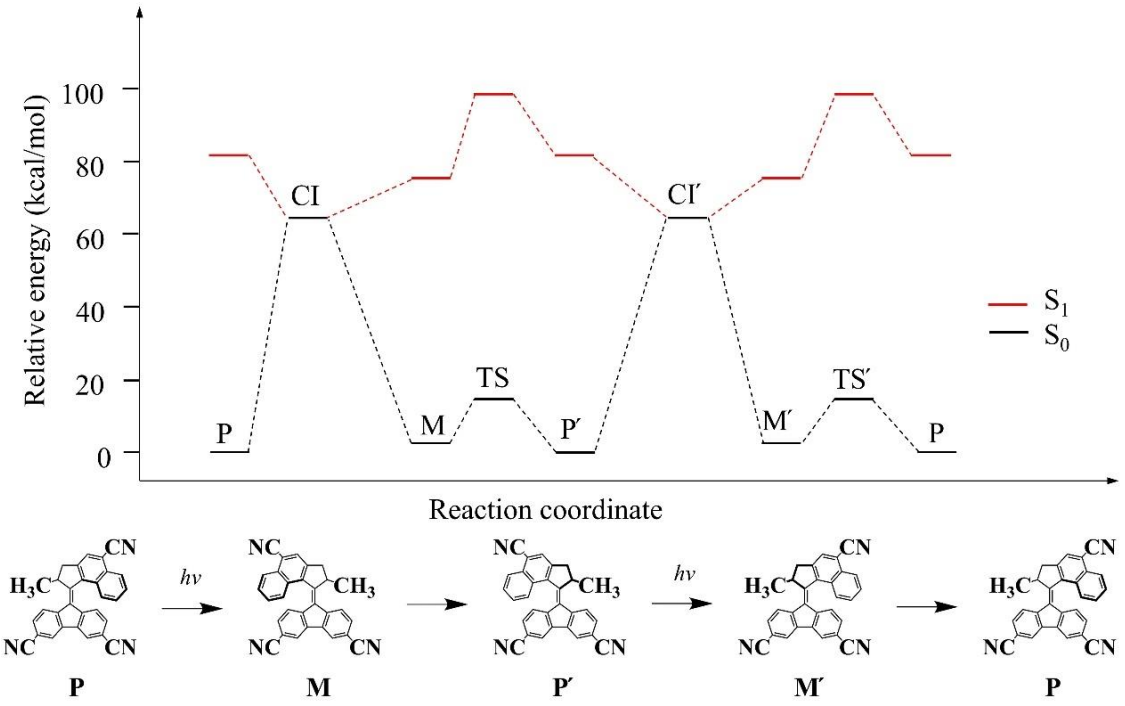

Figure 4.6 The energy profiles of S_0 and S_1 states of a rotation cycle for the molecule 6s (P → M→ P' → M' → P) at the OM2/MRCI level; CI and TS denote conical intersection and transition state, respectively.

Table 4.7 Energies of the relevant structures in the ground state for 6s, calculated by the OM2/MRCI method (in eV), and by the B3LYP-D3, CAMB3LYP-D3, M06-2X, and ωB97XD methods with 6-31G(d,p) basis sets (in Hartree). The energies relative to P are also given in parenthesis (in kcal/mol).

	OM2/MRCI	B3LYP-D3	CAMB3LYP-D3	M062X	ωB97XD
P	-4718.473	-1317.75644	-1317.00065	-1317.17537	-1317.25304
M	-4718.389 (1.9)	-1317.75117 (3.3)	-1316.99421 (4.0)	-1317.16911 (3.9)	-1317.24659 (4.0)
TS	-4717.522 (21.9)	-1317.71460 (26.3)	-1316.95834 (26.5)	-1317.13286 (26.7)	-1317.21080 (26.5)

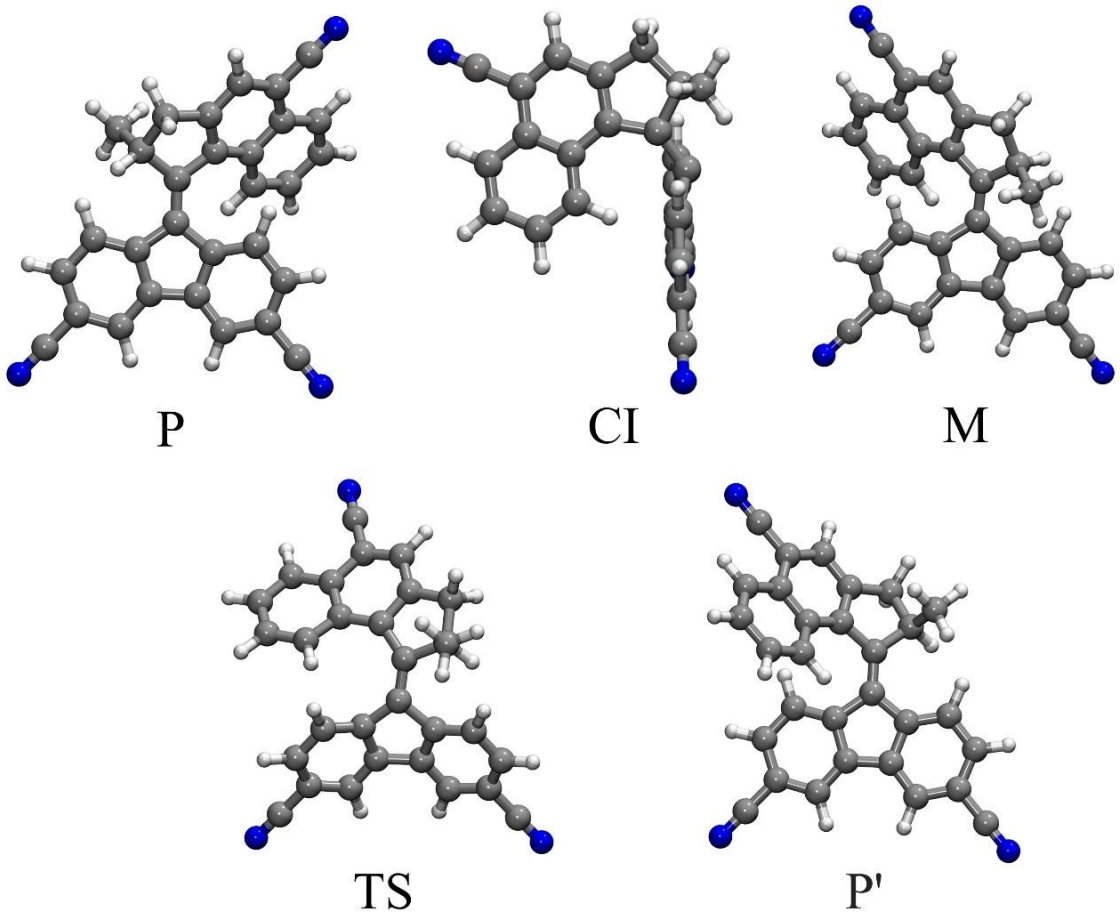

Figure 4.7 Optimized structures of minima, one conical intersection, and one transition state along the reaction pathway of molecule 6s calculated at the OM2/MRCI level.

Table 4.8 Geometrical parameters of optimized equilibrium and transition state structures in the ground state for 6s, calculated by the OM2/MRCI method, using the MNDO99 program,[147]and by B3LYP-D3, CAMB3LYP-D3, M06-2X, and ωB97XD methods with 6-31G(d,p) basis sets, using the Gaussian09 program.[129] The bond lengths are given in Å, while bond angles and dihedral angles are given in degrees.

		OM2/MRCI	B3LYP-D3	CAM-B3LYP-D3	M06-2X	WB97XD
P	C1-C2	1.35898	1.36989	1.35707	1.35968	1.35804
	C40-C2-C1	126.835	126.579	126.42	126.241	126.426
	C2-C1-C4	125.955	124.703	124.834	124.667	124.999
	C40-C2-C1-C4	21.6	21.599	20.799	20.296	20.941
	C40-C2-C1-C15	-169.998	-168.293	-169.6	-169.462	-169.603
	C2-C28-C40-C1	-0.882	-1.347	-1.405	-1.44	-1.294

	C2-C1-C15-C17	40.284	39.438	40.506	39.352	40.588
M	C1-C2	1.36383	1.3787	1.36441	1.36678	1.36501
	C40-C2-C1	127.85	127.689	127.928	128.025	127.857
	C2-C1-C4	124.585	124.304	124.786	124.65	125.075
	C40-C2-C1-C4	146.698	144.398	145.497	146.125	144.741
	C40-C2-C1-C15	-26.35	-29.937	-28.508	-27.649	-28.44
	C2-C28-C40-C1	-1.707	-1.211	-1.24	-1.191	-1.479
	C2-C1-C15-C17	-26.792	-26.783	-28.357	-28.262	-29.206
TS	C1-C2	1.36663	1.38642	1.37254	1.37609	1.37341
	C40-C2-C1	121.58	121.673	121.396	120.999	121.469
	C2-C1-C4	118.444	118.203	117.954	117.69	118.095
	C40-C2-C1-C4	-24.553	-25.939	-24.65	-24.364	-26.086
	C40-C2-C1-C15	140.401	138.229	141.927	142.268	139.706
	C2-C28-C40-C1	-8.77	-8.808	-8.871	-8.964	-9.125
	C2-C1-C15-C17	21.484	22.235	21.217	19.69	20.136
P'	C1-C2	1.35898	1.36989	1.36989	1.35968	1.35804
	C40-C2-C1	127.541	128.028	128.028	128.329	128.304
	C2-C1-C4	125.958	124.703	124.703	124.667	124.998
	C40-C2-C1-C4	-156.177	-154.997	-154.997	-156.057	-155.769
	C40-C2-C1-C15	12.228	15.112	15.112	14.186	13.688
	C2-C28-C40-C1	0.879	1.347	1.347	1.44	1.294
	C2-C1-C15-C17	40.287	39.438	39.438	39.353	40.588

Table 4.9. Geometrical parameters of the CI structure between S_0 and S_1 states for 6s, calculated by the OM2/MRCI method. The bond lengths are given in Å, while bond angles and dihedral angles are given in degrees.

C1-C2	1.41232
C40-C2-C1	103.484
C2-C1-C4	116.705
C40-C2-C1-C4	-114.918
C40-C2-C1-C15	55.426
C2-C28-C40-C1	-32.841
C2-C1-C15-C17	12.953

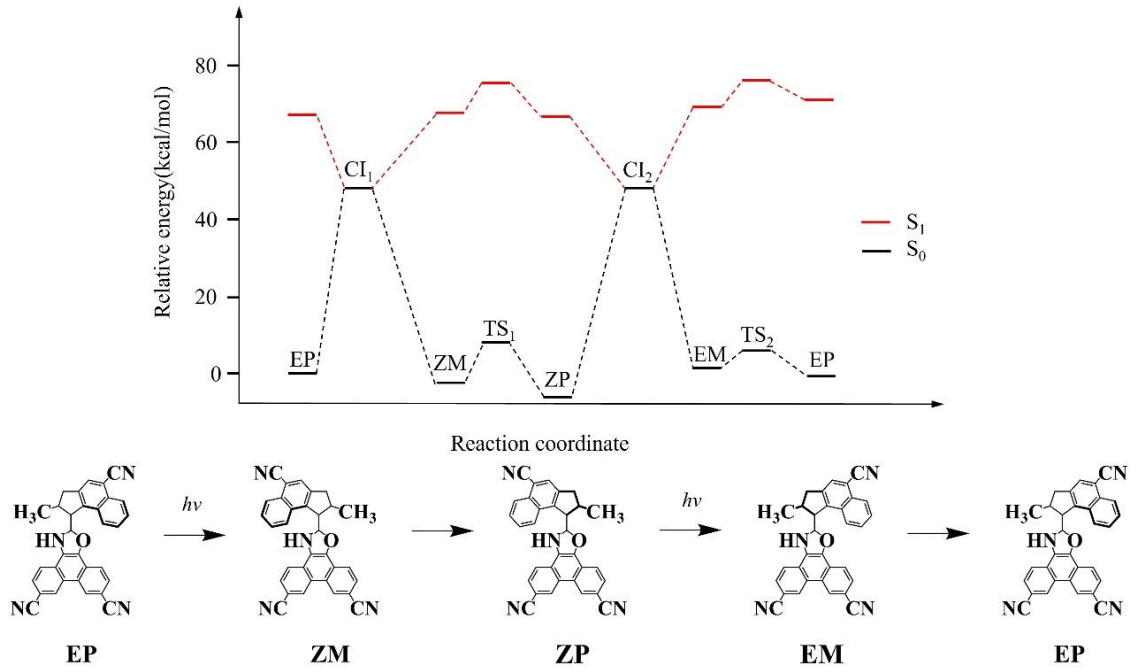

Figure 4.8 The energy profiles of S_0 and S_1 states of a rotation cycle for the molecular motor Xs (EP → ZM→ ZP → EM → EP) at the OM2/MRCI level; CI and TS denote conical intersection and transition state, respectively.

Table 4.10 Energies of the relevant structures in the ground state for Xs, calculated by the OM2/MRCI method (in eV), and by the B3LYP-D3, CAMB3LYP-D3, M06-2X, and ωB97XD methods with 6-31G(d,p) basis sets (in Hartree). The energies relative to EP are also given in parenthesis (in kcal/mol).

	OM2/MRCI	B3LYP-D3	CAMB3LYP-D3	M062X	ωB97XD
EP	-5823.673	-1584.97270	-1584.09429	-1584.26499	-1584.37052
ZM	-5823.81815 (-3.4)	-1584.97501 (-1.5)	-1584.10671 (-7.8)	-1584.27422 (-5.8)	-1584.38103 (-6.6)
TS1	-5823.645 (0.7)	-1584.96585 (4.3)	-1584.09820 (-2.5)	-1584.26679 (-1.1)	-1584.37327 (-1.7)
ZP	-5823.935 (-6.0)	-1584.98174 (-5.7)	-1584.11394 (-12.3)	-1584.28305 (-11.3)	-1584.38954 (-11.9)
EM	-5823.588 (2.0)	-1584.96833 (2.7)	-1584.10007 (-3.6)	-1584.26987 (-3.1)	-1584.37562 (-3.2)
TS2	-5823.499 (4.0)	-1584.95836 (9.0)	-1584.08996 (2.7)	-1584.25845 (4.1)	-1584.36531 (3.3)

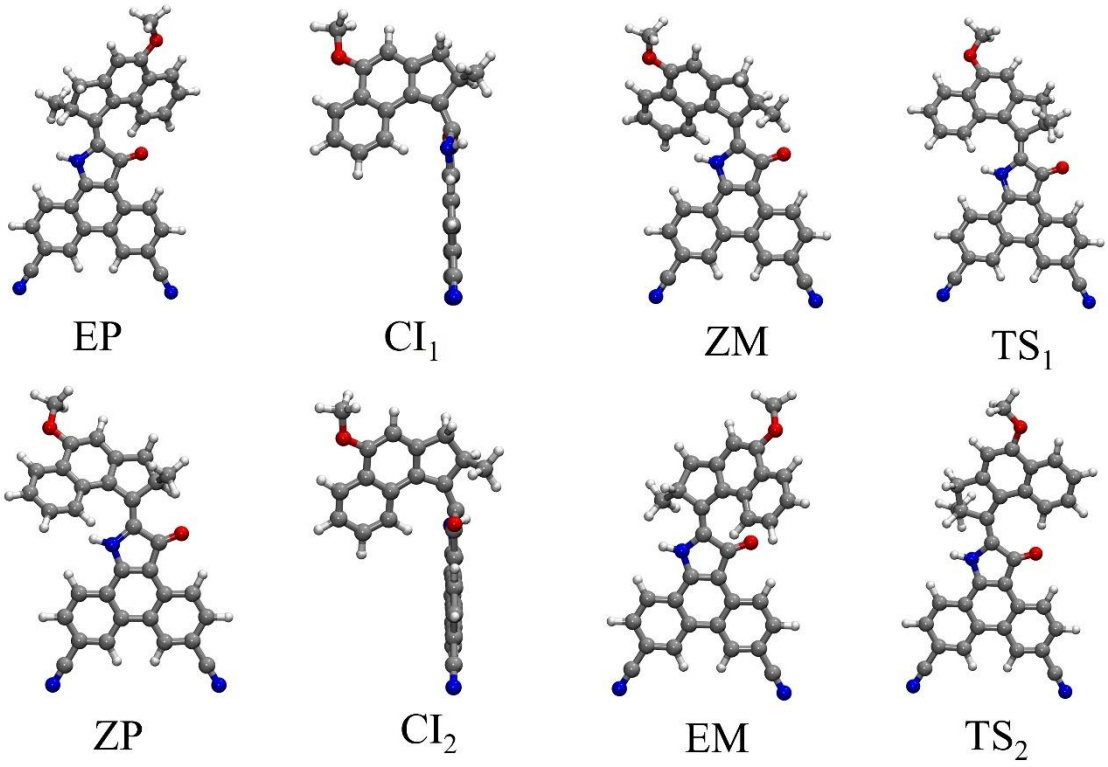

Figure 4.9 Optimized structures of minima, conical intersections, and transition states along the reaction pathway of molecule Xs calculated at the OM2/MRCI level.

Table 4.11 Geometrical parameters of optimized equilibrium and transition state structures in the ground state for Xs, calculated by the OM2/MRCI method, using the MNDO99 program,[147] and by B3LYP-D3, CAMB3LYP-D3, M06-2X, and wB97XD methods with 6-31G(d,p) basis sets, using the Gaussian09 program.[129] The bond lengths are given in Å, while bond angles and dihedral angles are given in degrees.

		OM2/MRCI	B3LYP-D3	CAM-B3LYP-D3	M06-2X	WB97XD
EP	C1-C2	1.36942	1.36419	1.35219	1.35451	1.3543
	C40-C2-C1	121.753	122.046	122.228	122.385	121.928
	C2-C1-C4	129.564	130.965	131.198	130.97	131.214
	C40-C2-C1-C4	10.601	10.096	9.477	8.684	9.52
	C40-C2-C1-C15	-177.726	-176.97	-177.985	-179.27	-178.09
	C2-C28-C40-C1	4.06	5.214	5.091	5.511	5.218
	C2-C1-C15-C17	30.966	30.427	31.366	31.89	32.103
ZM	C1-C2	1.36982	1.36793	1.35618	1.35758	1.35802

	C40-C2-C1	123.841	126.638	127.098	123.916	123.588
	C2-C1-C4	125.563	130.516	130.624	125.645	126.056
	C40-C2-C1-C4	163.12	162.916	163.705	160.136	160.544
	C40-C2-C1-C15	-5.823	-7.113	-6.271	-9.365	-9.637
	C2-C28-C40-C1	-1.487	-0.683	-0.67	-1.135	-1.457
	C2-C1-C15-C17	-30.039	-13.217	-13.117	-29.498	-28.605
TS1	C1-C2	1.37169	1.37165	1.36005	1.3624	1.36188
	C40-C2-C1	129.854	128.315	128.556	128.58	128.137
	C2-C1-C4	134.649	135.526	135.399	135.434	135.358
	C40-C2-C1-C4	-179.489	-177.662	-178.657	-179.469	-177.655
	C40-C2-C1-C15	-5.088	-4.575	-3.711	-2.785	-4.958
	C2-C28-C40-C1	-2.398	-3.361	-3.566	-3.971	-3.793
	C2-C1-C15-C17	17.746	12.818	13.355	12.946	14.367
ZP	C1-C2	1.36593	1.36178	1.35035	1.35287	1.35223
	C40-C2-C1	126.864	126.493	126.903	127.077	126.389
	C2-C1-C4	128.289	129.523	129.547	129.44	129.162
	C40-C2-C1-C4	-170.801	-168.852	-169.122	-169.133	-169.63
	C40-C2-C1-C15	-4.392	1.501	1.182	0.826	-0.04
	C2-C28-C40-C1	0.09	-1.672	-1.634	-2.086	-1.752
	C2-C1-C15-C17	33.045	27.369	27.583	27.084	28.015
EM	C1-C2	1.37008	1.36667	1.35423	1.35638	1.35703
	C40-C2-C1	124.427	124.101	124.568	124.636	124.16
	C2-C1-C4	125.925	127.795	127.852	127.672	127.634
	C40-C2-C1-C4	-15.286	-15.552	-14.147	-14.313	-15.487
	C40-C2-C1-C15	171.35	170.469	172.936	172.656	170.871
	C2-C28-C40-C1	-3.854	-4.841	-4.687	-4.786	-4.726
	C2-C1-C15-C17	-30.243	-30.551	-33.004	-33.14	-31.639
TS2	C1-C2	1.38233	1.3852	1.37165	1.37442	1.37376
	C40-C2-C1	118.168	117.287	117.477	117.364	117.307
	C2-C1-C4	136.885	138.813	139.096	139.301	138.927
	C40-C2-C1-C4	-5.25	-8.432	-8.136	-7.905	-8.523
	C40-C2-C1-C15	171.155	170.772	171.432	172.254	170.103
	C2-C28-C40-C1	-2.147	-1.858	-2.007	-1.917	-2.227
	C2-C1-C15-C17	13.135	7.982	7.181	7.099	8.624

Table 4.12 Geometrical parameters of the CI_1 and CI_2 structures between S_0 and S_1 states for Xs, calculated by the OM2/MRCI method. The bond lengths are given in Å, while bond angles and dihedral angles are given in degrees.

		OM2/MRCI
CI_1	C1-C2	1.40915
	C40-C2-C1	124.397
	C2-C1-C4	130.702
	C40-C2-C1-C4	-118.012
	C40-C2-C1-C15	74.254
	C2-C28-C40-C1	21.238
	C2-C1-C15-C17	-8.935
CI_2	C1-C2	1.40818
	C40-C2-C1	125.556
	C2-C1-C4	130.535
	C40-C2-C1-C4	118.805
	C40-C2-C1-C15	-76.244
	C2-C28-C40-C1	-20.878
	C2-C1-C15-C17	12.413

Table 4.13 The THI barriers for 1s, 2s, 6s, and Xs at the levels of OM2/MRCI, B3LYP-D3, CAMB3LYP-D3, M06-2X, and wB97XD. The energy is given in kcal/mol.

		OM2/MRCI	B3LYP-D3	CAMB3LYP-D3	M062X	wB97XD
1s	M → P'	19.80	22.06	21.52	21.80	21.52
2s	M → P'	20.59	23.50	22.95	23.13	22.92
6s	M → P'	20.01	22.95	22.51	22.75	22.46
Xs	ZM → ZP	4.00	5.74	5.33	4.66	4.87
	EM → EP	2.05	6.26	6.35	7.17	6.47
DDPYM[128]	ZM → ZP	2.00				
	EM → EP	8.80				

4.3.2 Absorption spectrum

To evaluate the performance of the newly designed Xs molecular motor, we conducted calculations of Ultraviolet-visible (UV-vis) absorption spectra using the TDDFT method.

These calculations were carried out for the optimized structures of 1s, 2s, 6s, Xs, and DDPYM at the PBE0-D3 level. The $S_0 \rightarrow S_1$ excitation energy was homogeneously broadened with a full width at half maximum (FWHM) of 0.5eV using Gaussian function expansion. The absorption wavelengths (in nm) and excitation energies (in eV) for the S_1 state calculated by TDDFT and OM2/MRCI are shown in **Table 4.14**, and the corresponding absorption spectra derived from the excited states of $S_1 - S_6$ are depicted in **Figure 4.10 (a)**, while the excited state energy are shown in **Table 4.15**. The corresponding experimental absorption spectra for 1s, 2s, and 6s[115] are also presented in **Figure 4.10 (b)** for comparison. In **Figure 4.10 (a)**, molecular motors 1s, 2s, 6s, and Xs exhibit absorption peaks ranging from 350 to 600 nm. The maximum absorption wavelengths for motors 1s, 2s, and 6s, calculated using TDDFT, are 445.28, 422.21, and 425.22 nm, respectively. These values align well with the corresponding experimental data, even though the maximum absorption wavelengths for 1s and 2s have been reversed. We have also performed TDDFT calculations considering solvent effects on the excitation energy of the S_1 state and compared these results with those obtained in the gas phase shown in **Table 4.16**. Conversely, the newly designed motor Xs shows maximum absorption wavelengths (EP and ZP) at 482.98 nm and 465.76 nm, respectively. Notably, these values represent a significant redshift when compared to the absorption wavelengths of 1s, 2s, and 6s. Furthermore, in comparison to the EP and ZP values of DDPYM, motor Xs exhibits a substantial redshift of 89.98 nm and 129.76 nm, respectively.

The absorption spectra and overall UV-vis spectra generated from Wigner sampling at the OM2/MRCI level were also calculated and are shown in **Figure 4.11 (a)** and **Figure 4.11 (b)**, respectively, with maximum absorption wavelengths listed in **Table 4.14**. The absorption spectra of 1s, 2s, 6s, and Xs span from 250 to 550 nm, qualitatively aligning with TDDFT calculations. Notably, the maximum absorption wavelength of Xs (EP and ZP) is greater than that observed for 1s, 2s, and 6s, which can also be recognize in **Figure 4.11 (b)**. The consistency between the several sets of results indicates that the newly

designed motors exhibit a significant redshift in the UV-vis absorption spectrum. To further elucidate the reason for the redshift of Xs, we examined the relevant frontier molecular orbitals. As illustrated in **Figure 4.12**, the HOMO-LUMO energy gap of molecular motor Xs is notably low compared to the substituent motors 1s, 2s, and 6s. The structural modification of Xs has reduced the HOMO-LUMO energy gap by altering the HOMO and LUMO charge distribution. Consequently, the maximum wavelengths of the UV-vis absorption spectra of the newly designed molecular motor Xs were red-shifted to 482.98 and 465.76 nm.

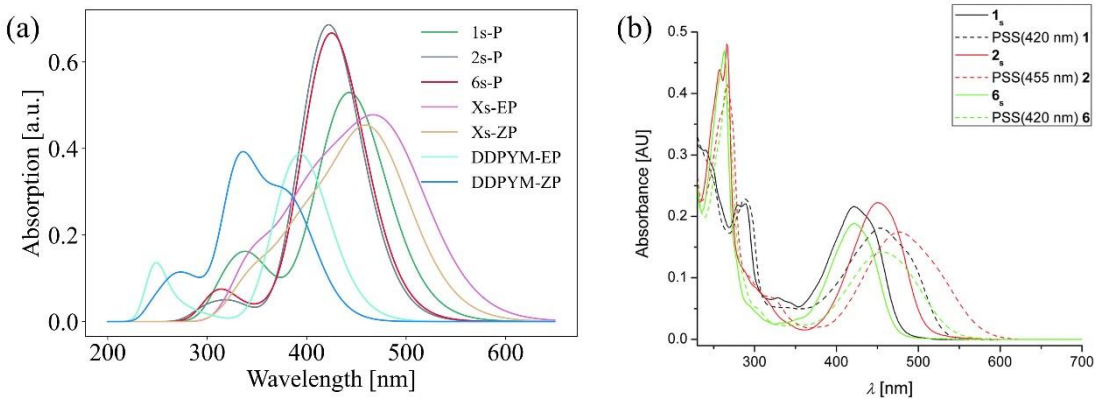

Figure 4.10 (a) UV-Vis spectra and equilibrium structures of 1s, 2s, 6s, Xs, and DDPYM determined in the gas phase by TDDFT calculations at the PBE0-D3/6-31G(d,p) level. (b) The experimental spectra for 1s, 2s, and 6s, taken from Ref. 11 (Chem. Sci., 2019, 10, 8768) (Solid lines: UV-vis spectra of 1s, 2s, and 6s in dichloromethane solvent. Dashed lines: UV-vis spectra after irradiation to photo-stationary states (PSS) with 420 nm (1s, 6s) and 455 nm (2s) light).

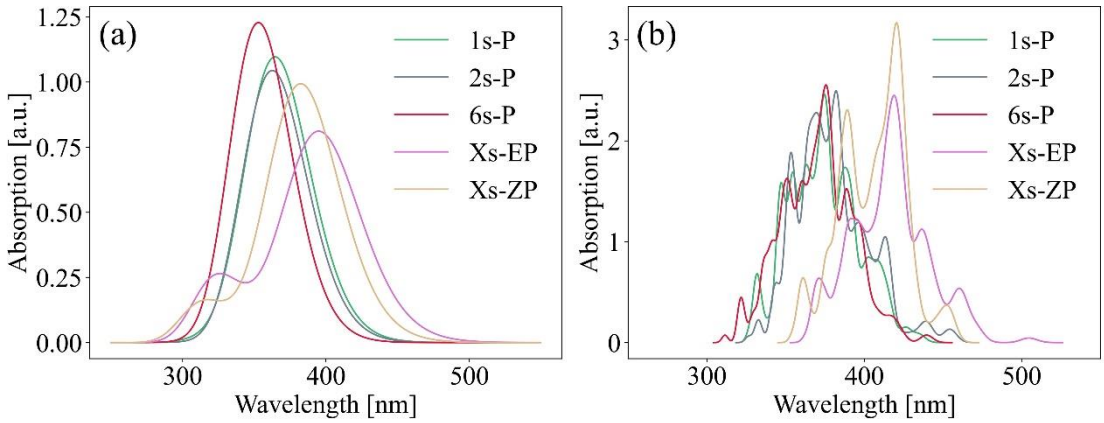

Figure 4.11 The UV-vis spectra calculated for 1s, 2s, 6s, and Xs at the OM2/MRCI level: (a) generated from the absorption at the equilibrium structure; (b) generated from 200 geometries around equilibrium structures from Wigner sampling. The $S_0 \rightarrow S_1$ excitation energy has been broadened to a full width at half maximum (FWHM) of 0.05 eV using the Newton-X 2.6 program[154]. By comparing panels (a) and (b), one can observe the extent to which the absorption spectra are influenced by molecules whose structures are distributed near the equilibrium structure via Wigner sampling. Although multiple peaks appear for each molecule, the peaks showing the maximum absorption intensity do not deviate significantly from the equilibrium structure.

Table 4.14 The absorption wavelengths (in nm) and excitation energies (in eV) for the S_1 state of the molecules 1s, 2s, 6s, Xs, and DDPYM, calculated using two methods: TDDFT with PBE0-D3/6-31G(d,p) and OM2/MRCI. The experimental data for 1s-P, 2s-P, and 6s-P measured in dichloromethane (DCM) solvent[115] are also presented.

		TDDFT	OM2/MRCI	Exp.
1s	P	445.28/2.78	364.5/3.40	422/2.94
2s	P	422.21/2.94	362.5/3.42	453/2.74
6s	P	425.22/2.92	353.0/3.51	421/2.95
Xs	EP	482.98/2.57	395.0/3.14	
	ZP	465.76/2.66	382.5/3.24	
DDPYM	EP	385.99/3.21		
	ZP	383.00/3.23		

Table 4.15 Excitation energies (in eV) and oscillator strengths of the electronic states, ranging from S1 to S6, for 1s-P, 2s-P, 6s-P, Xs-ZP, and Xs-EP, using the PBE0-D3/6-31G(d,p) level of theory. Based on the oscillator strengths obtained, the primary excited state for is identified as S1.

	1s-P	2s-P	6s-P	Xs-EP	Xs-ZP
S_1	2.78/0.4930	2.94/0.6858	2.92/0.6656	2.57/0.3928	2.66/0.4190
S_2	2.99/0.0553	3.39/0.0002	3.11/0.0005	2.90/0.2101	3.07/0.1746
S_3	3.55/0.1094	3.76/0.0258	3.46/0.0213	3.15/0.1635	3.17/0.0410
S_4	3.78/0.0453	3.84/0.0149	3.88/0.0298	3.39/0.0286	3.44/0.0109
S_5	3.90/0.0505	4.04/0.0006	3.99/0.0292	3.57/0.1123	3.52/0.0897
S_6	4.02/0.0026	4.15/0.0292	4.04/0.0185	3.74/0.0261	3.78/0.0284

Table 4.16 The absorption wavelengths (in nm) and excitation energies (in eV) for the S1 state of the molecules 1s-P, 2s-P, 6s-P, Xs-EP, and Xs-ZP, calculated by TDDFT and TDDFT(DCM) with PBE0-D3/6-31G(d,p). TDDFT(DCM) refers to the values calculated using the Polarizable Continuum Model (PCM) to include the effects of the dichloromethane (DCM) solvent. The experimental data for 1s-P, 2s-P, and 6s-P measured in DCM solvents[115] are also presented. When comparing the calculated values with experimental data, they generally align well. Specifically, for 2s-P, the results incorporating solvent effects show a particularly close match with experimental values.

	TDDFT	TDDFT(DCM)	Exp.
1s-P	445.28/2.78	463.46/2.68	422/2.94
2s-P	422.21/2.94	447.24/2.77	453/2.74
6s-P	425.22/2.92	443.54/2.79	421/2.95
Xs-EP	482.98/2.57	499.28/2.48	
Xs-ZP	465.76/2.66	487.28/2.54	

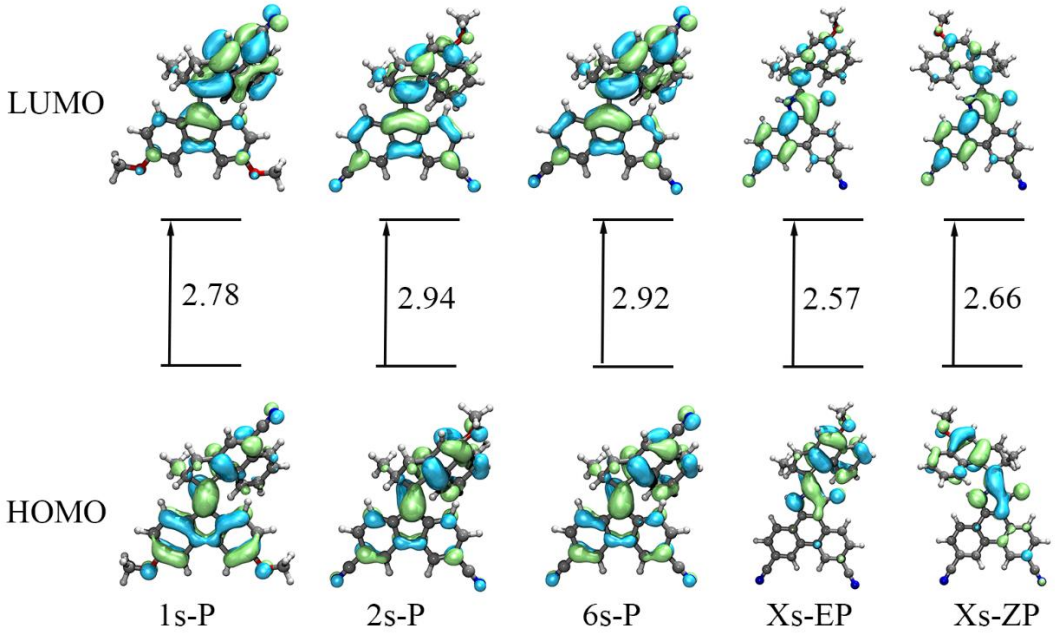

Figure 4.12 The HOMO and LUMO of motor 1s-P, 2s-P, 6s-P, Xs-EP, and Xs-ZP, calculated at the PBE0-D3/6-31G(d,p) level with unit in eV.

4.3.3 Trajectory surface hopping simulations

Trajectory surface hopping (TSH) simulations were systematically conducted to explore the photoisomerization processes of 1s, 2s, 6s, and Xs. Initially, for each system, the CI of S_1/S_0 was optimized at the OM2/MRCI level. The relevant geometric structure data are summarized in **Tables 4.3, 4.6, 4.9 and 3.12. Figures 4.3, 4.5, 4.7** illustrate that the obtained S_1/S_0 CI points for 1s, 2s, and 6s are distinguished by different dihedral angles $\theta_{4\text{-}1\text{-}2\text{-}28}$ and $\theta_{15\text{-}1\text{-}2\text{-}28}$. For Xs, the four S_1/S_0 CI points, denoted as CI_1 and CI_2, are identified based on the dihedral angles $\theta_{4\text{-}1\text{-}2\text{-}28}$ and $\theta_{15\text{-}1\text{-}2\text{-}28}$ (refer to **Figure 4.1** for key atomic labels), as shown in **Figure 4.9**. The CI geometries obtained for 1s, 2s, 6s, and Xs all exhibit pronounced pyramidalization at the carbon atoms of the stator-axle, a phenomenon reported in other molecular motor studies.[107,127,131,155,156] To directly observe

the pyramidalization phenomenon during dynamics simulations, the time dependence of the dihedral angles $\theta_{4\text{-}1\text{-}2\text{-}28}$, $\theta_{15\text{-}1\text{-}2\text{-}28,}$ $\theta_{2\text{-}40\text{-}28\text{-}1}$ for 1s, 2s, 6s, and Xs in one representative trajectory is presented in **Figures 4.13, 4.14, 4.15 and Figure 4.16.**

To deepen our understanding of the photoisomerization process in 1s, 2s, and 6s, we have detailed the behavior of crucial angles, specifically, $\theta_{2\text{-}40\text{-}28\text{-}1}$, $\theta_{4\text{-}1\text{-}2\text{-}28}$, and $\theta_{15\text{-}1\text{-}2\text{-}28}$, across characteristic trajectories. These figures reveal the dihedral angles $\theta_{4\text{-}1\text{-}2\text{-}28}$ evolving from initial setups to the conical intersection points at 1821.3, 1157.5 and 2949.1 fs, respectively, before hopping to the S_0 state. Throughout this decay, the dihedral angle $\theta_{4\text{-}1\text{-}2\text{-}28}$ shows a decrease marked by minor fluctuations, in contrast to the dihedral angle $\theta_{15\text{-}1\text{-}2\text{-}28}$, which exhibits a steady increase. Approaching the conical intersection, the angle $\theta_{2\text{-}40\text{-}28\text{-}1}$ shifts abruptly, showing dynamic shifts akin to precessional motion. After internal conversion to the S_0 state, there's a sequential decrease in $\theta_{4\text{-}1\text{-}2\text{-}28}$ and increase in $\theta_{15\text{-}1\text{-}2\text{-}28}$, leading both angles to settle into slight oscillations within the M region - signaling the end of the photoisomerization journey. In molecular dynamics (MD) simulations, we use the velocity-Verlet algorithm, which largely preserves total energy if appropriate time steps are utilized. However, when performing TSH calculations for excited states based on multi-configurational and multi-reference wavefunctions, structural changes during MD calculations can cause the orbitals within the active space to swap with outer orbitals, or states included in the state averaging to swap with external states, which can potentially disrupt the conservation of total energy. In this study, using the OM2/MRCI method, we observe cases where energy conservation is compromised due to such reasons. Significant discrepancies are particularly evident for 1s. To gain a thorough insight into the isomerization mechanism of the Xs, we explore two representative trajectories, namely EP → ZM and ZP → EM, which represent pivotal transitions within the molecular motor's isomerization processes. Starting with EP → ZM, the journey begins as the EP isomer is energetically uplifted to the S_1 state, setting the molecular motor on a path across the excited-state potential energy landscape until it descends back to the ground state at 713.9

fs. Illustrated in **Figure 4.16** (b-d), this path witnesses the dihedral angle $\theta_{4\text{-}1\text{-}2\text{-}28}$, a critical link between the rotor and stator, ascend from its optimized EP form, experiencing fluctuations to stabilize at a 20° inclination by 713.9 fs. Concurrently, the dihedral angle $\theta_{15\text{-}1\text{-}2\text{-}28}$ exhibits a gradual decrement. Notably, the dihedral angle $\theta_{2\text{-}40\text{-}28\text{-}1}$ sees a swift increase, heralding the trajectory's venture into the CI region, alongside a pronounced pyramidalization at the carbon atom nestled within the stator-axle. The culmination of this photoisomerization sequence is signified by the dihedral angles $\theta_{4\text{-}1\text{-}2\text{-}28}$ and $\theta_{15\text{-}1\text{-}2\text{-}28}$ achieving equilibrium. Turning our focus to the ZP → EM transition depicted in **Figure 4.16 (f-h)**, the narrative unfolds with the dihedral angle $\theta_{4\text{-}1\text{-}2\text{-}28}$ embarking from its initial stance, navigating through CI geometries at 1798.0 fs, before gracefully transitioning to the ground state. This relaxation phase sees the dihedral angle $\theta_{15\text{-}1\text{-}2\text{-}28}$ diminish from the ZP isomer's 170°, alongside a significant swell in the dihedral angle $\theta_{2\text{-}40\text{-}28\text{-}1}$, a movement that underscores the carbon atom's pyramidalization at the stator-axle. Impressively, the dihedral angle $\theta_{4\text{-}1\text{-}2\text{-}28}$ escalates from a modest 20° in ZP to a striking 170° throughout the ZP → EM isomerization, leading to a successful conclusion as the dihedral angles $\theta_{4\text{-}1\text{-}2\text{-}28}$ and $\theta_{15\text{-}1\text{-}2\text{-}28}$ stabilize at predetermined coordinates, effectively charting the isomerization's course. Summarily, As the trajectories approach the CI region, the dihedral angle $\theta_{2\text{-}40\text{-}28\text{-}1}$ (1s, 2s, 6s) reaches about 30°, and the dihedral angle $\theta_{2\text{-}40\text{-}28\text{-}1}$ (Xs-EP, Xs-ZP) also gradually increase to about 20°. This observation indicates that the pyramidalization of carbon atoms at the stator-axle becomes evident in the dynamic's simulations.

For 1s, 2s, 6s, Xs (EP), and Xs (ZP), 400 structures were generated, respectively, using Wigner sampling. Through the filtering approach, about 70% of these structures were selected. From the chosen structures, 175, 242, 233, 220, and 179 structures, respectively, were selected as initial conditions for trajectory calculations, and we conducted TSH simulations from the S_1 excited state. The simulation times were 5.0, 2.5, 5.0, 1.5, and 3.0 ps for each molecular species. Isomerization to M was achieved for 1s, 2s, and 6s by counterclockwise rotation around the

central C=C double bond, with quantum yields of approximately 0.78, 0.6, and 0.67, respectively. For Xs, the photoisomerization process was investigated for EP and ZP starting from the S_1 excited state, with quantum yields of approximately 0.55 and 0.37 for EP → ZM and ZP → EM, respectively. In the case of DDPYM, the quantum yield for the transition from EP to ZM is 0.52, and for the transition from ZP to EM is 0.36. which is comparable to Xs. **Figure 4.17** illustrates the time evolution of the S_0 and S_1 state populations for 1s, 2s, 6s, Xs-EP, and Xs-ZP. The average lifetimes of the S_1 state for each molecular species are calculated to be 2.56, 1.16, 2.40, 0.85, and 1.85 ps, respectively. **Table 4.17** presents the number of trajectories, quantum yields, and lifetimes. The newly designed molecular motor Xs exhibits a slight decrease in the quantum yield of the photoisomerization reaction compared to 1s, 2s, and 6s. The time evolution of the population reveals that the average lifetime of the EP → ZM isomerization of Xs is extremely short compared to 1s, 2s, and 6s, and the ZP → EM isomerization reaction is also significantly shorter than that of 1s and 6s. Indeed, when comparing the simulated average lifetimes of DDPYM for the EP → ZM (0.27) and ZP → EM (0.44), it becomes evident that the lifetimes in DDPYM are significantly shorter than those in Xs. This suggests that Xs may exhibit longer-lived excited states compared to DDPYM.

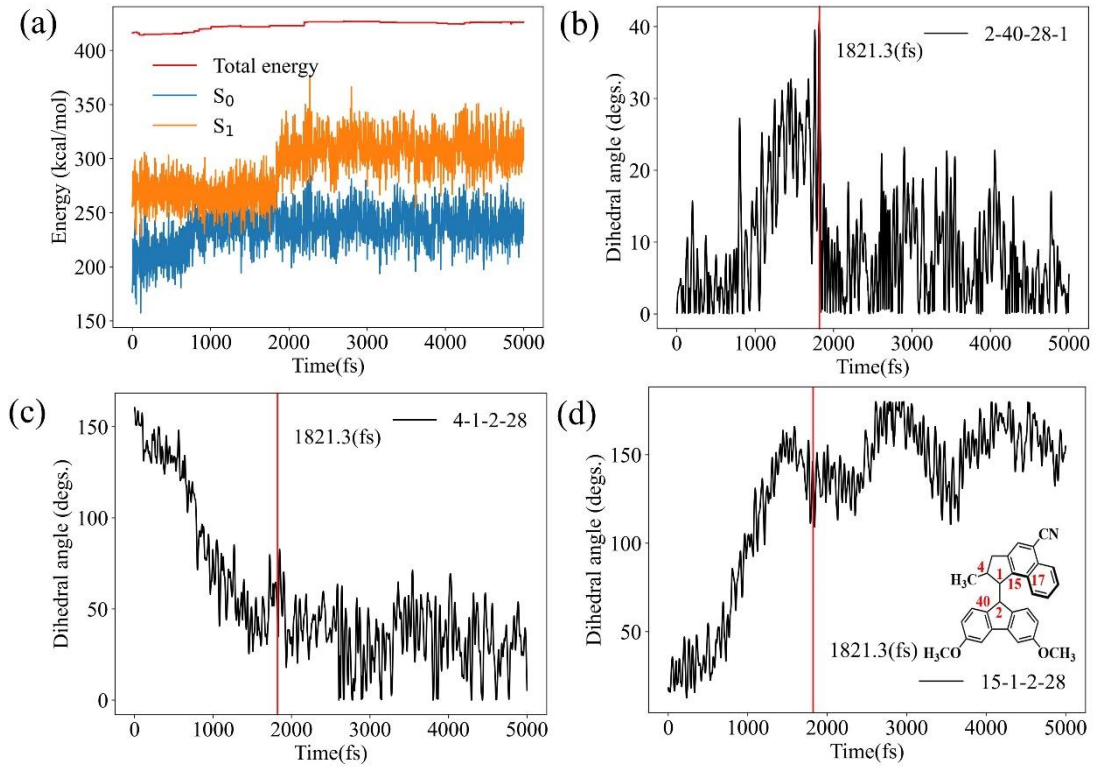

Figure 3.13 (a) Variation of S_0 and S_1 energies and (b-d) variations of the dihedral angles $\theta_{2\text{-}40\text{-}28\text{-}1}$, $\theta_{4\text{-}1\text{-}2\text{-}28}$, and $\theta_{15\text{-}1\text{-}2\text{-}28}$, along a typical trajectory for 1s.

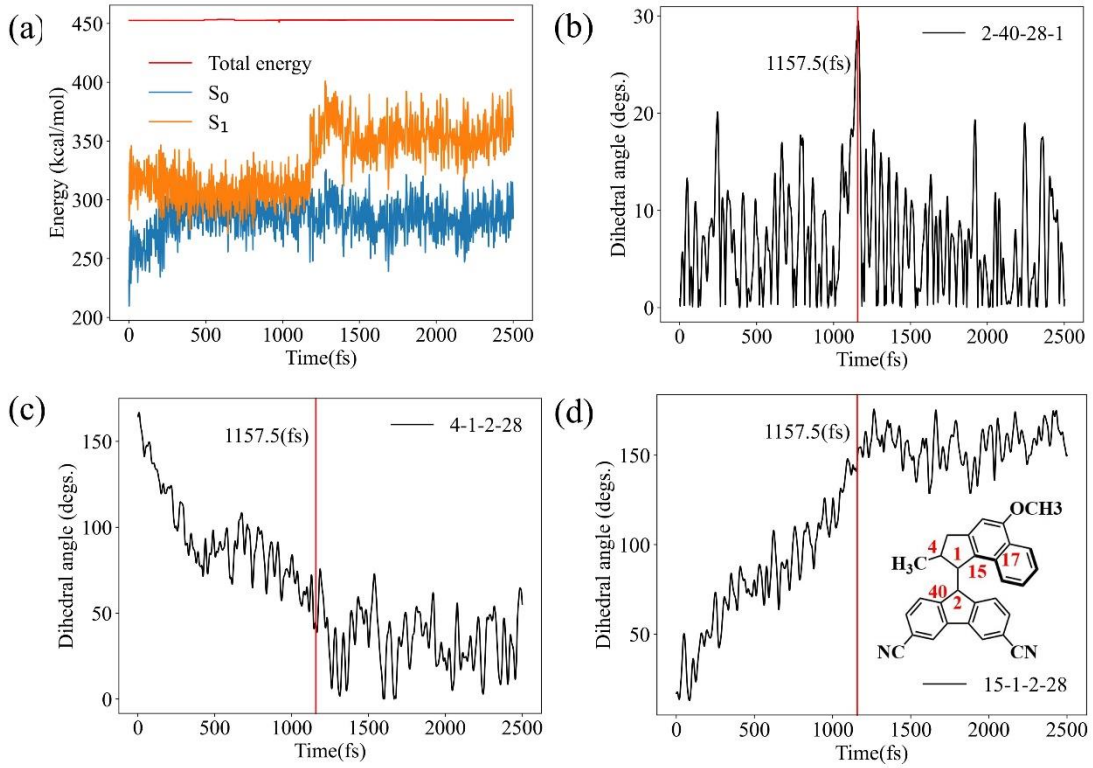

Figure 4.14 (a) Variation of S_0 and S_1 energies and (b-d) variations of the dihedral angles $\theta_{2\text{-}40\text{-}28\text{-}1}$, $\theta_{4\text{-}1\text{-}2\text{-}28}$, and $\theta_{15\text{-}1\text{-}2\text{-}28}$, along a typical trajectory for 2s.

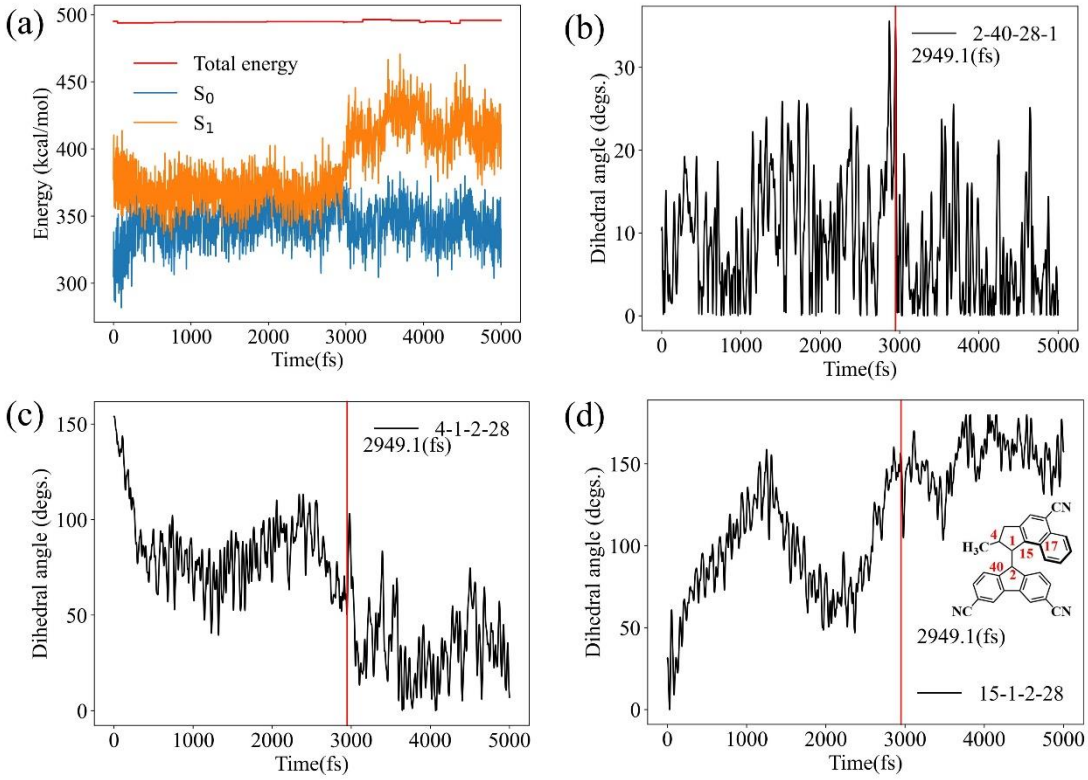

Figure 4.15 (a) Variation of S_0 and S_1 energies and (b-d) variations of the dihedral angles $\theta_{2\text{-}40\text{-}28\text{-}1}$, $\theta_{4\text{-}1\text{-}2\text{-}28}$, and $\theta_{15\text{-}1\text{-}2\text{-}28}$, along a typical trajectory for 6s.

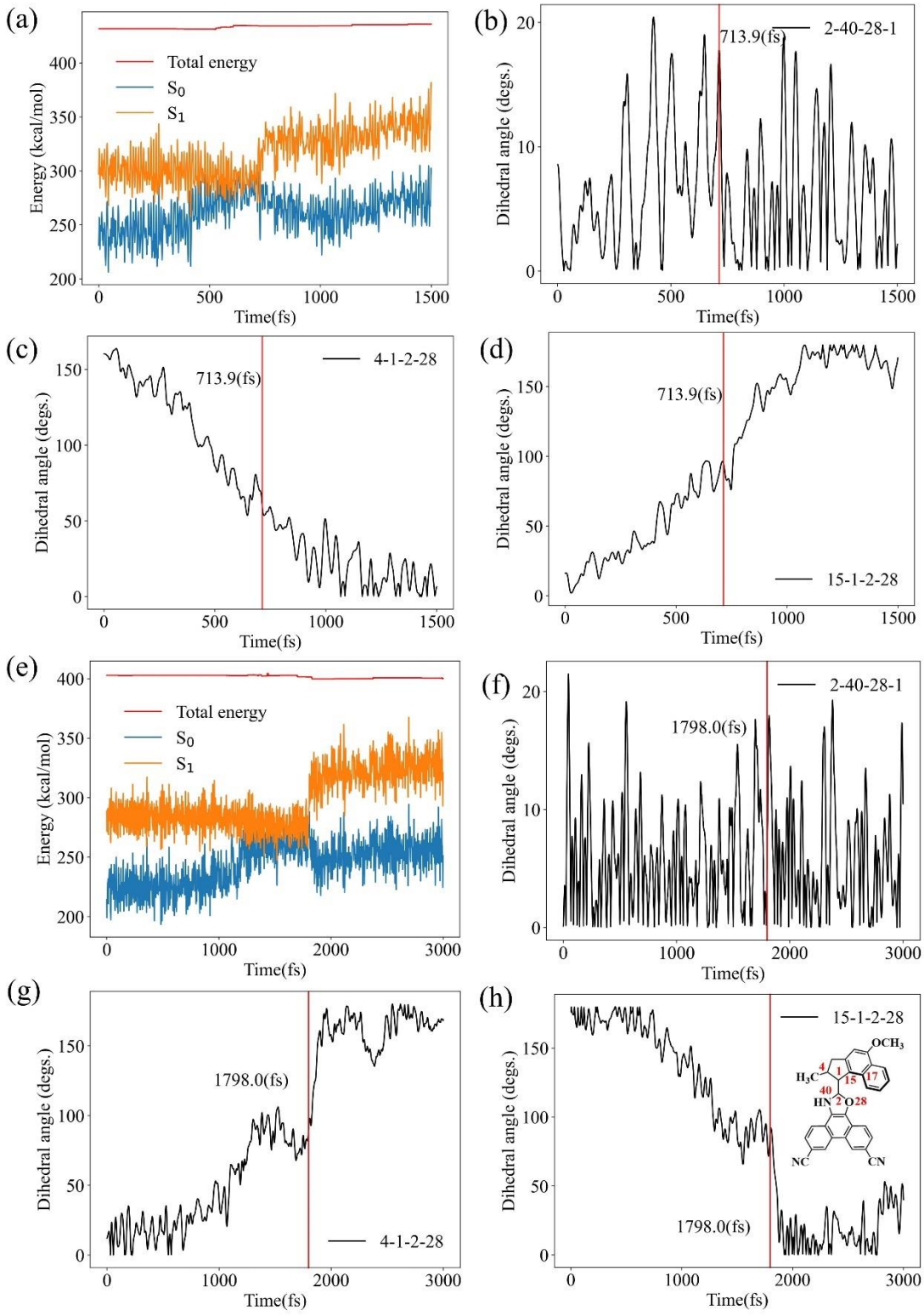

Figure 4.16 (a) Variation of S_0 and S_1 energies and (b-d) variations of the dihedral angles $\theta_{2\text{-}40\text{-}28\text{-}1}$, $\theta_{4\text{-}1\text{-}2\text{-}28}$, and $\theta_{15\text{-}1\text{-}2\text{-}28}$, along a typical trajectory for Xs-EP; (e) Variation of S_0 and S_1 energies and (f-h) variations of the dihedral angles $\theta_{2\text{-}40\text{-}28\text{-}1}$, $\theta_{4\text{-}1\text{-}2\text{-}28}$, and $\theta_{15\text{-}1\text{-}2\text{-}28}$,

along a typical trajectory for Xs-ZP.

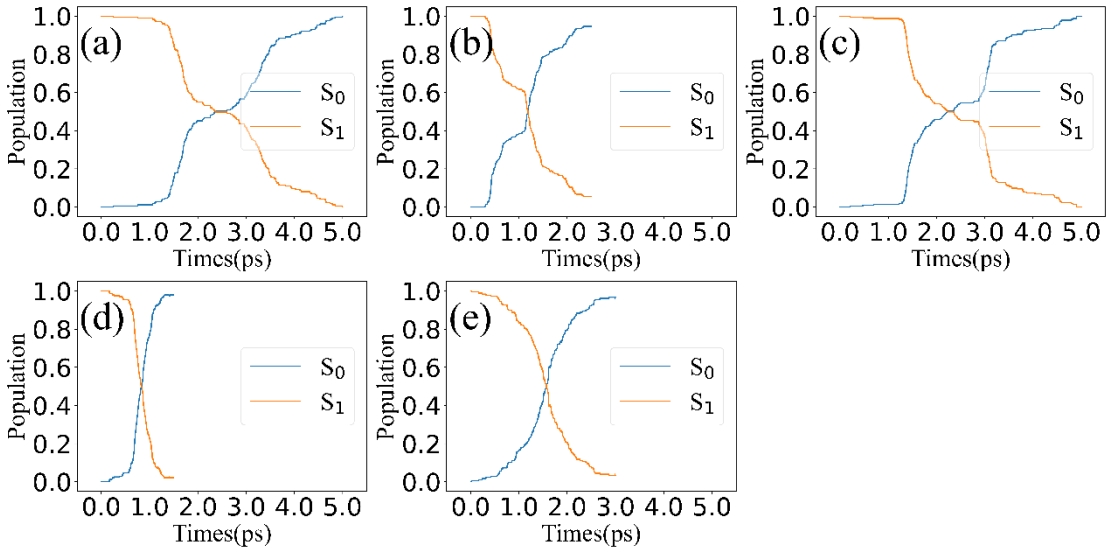

Figure 4.17 The average population of electronic states S_0 and S_1 over simulation time in the photoisomerization process starting from (a) 1s-P, (b) 2s-P, (c) 6s-P, (d) Xs-EP, and (e) Xs-ZP isomers.

Table 4.17 The simulated quantum yields and average lifetimes for the photoisomerization of 1s, 2s, 6s, and Xs.

		Number of trajectories	Quantum yields	Average lifetime (ps)
1s	P-M	175	0.78	2.56
2s	P-M	242	0.60	1.16
6s	P-M	233	0.67	2.40
Xs	EP-ZM	220	0.55	0.85
	ZP-EM	179	0.37	1.58
DDPYM[128]	EP-ZM	238	0.52	0.27
	ZP-EM	221	0.36	0.44

To provide further insight into the reduced lifetime of Xs-EP and Xs-ZP compared

to 1s, 2s, and 6s, we conducted nonadiabatic dynamics simulations of the photoisomerization process to compute the "dark state" duration. The dark state duration was determined based on the obtained average lifetime and the time-dependent fluorescence emission spectrum presented in **Figures 3.18, 3.19, 3.20, 3.21, and 3.22,** with the corresponding data listed in **Table 3.18**. It is important to note that the term "dark state" in this context does not refer to a new electronic state but rather signifies a "dark region" with low oscillator strength on the excited state.[131] The computational details of the time-dependent fluorescence emission spectrum and a more comprehensive description of the computational results are described in this part. As indicated in **Table 4.18**, the "dark state" durations for 1s, 2s, and 6s are 1.86, 0.90, and 2.06 ps, respectively, which are significantly longer than those for Xs-EP and Xs-ZP at 0.09 and 0.26 ps. This observation may elucidate why the average lifetime of the EP → ZM process for XS is extremely shorter than that for 1s, 2s, and 6s, and the ZP → EM process is also significantly shorter than that for 1s and 6s. The slightly higher average lifetime of ZP → EM process for Xs compared to 2s may be attributed to the steric bulkiness in the fjord region of Xs-ZP (C40-C2-C1-C15 is -4.4°, C2-C1-C15-C17 is 33.0° based on OM2/MRCI level), which is less than that of 2s-P (C40-C2-C1-C15 is 12.9° and C2-C1-C15-C17 is 39.3° based on OM2/MRCI level). This difference in steric hindrance implies that the rotation from Xs-ZP to the CIs will take more time than for 2s, even though the "dark state" duration is significantly reduced for Xs-ZP compared to 1s-P.

The time-resolved fluorescence emission spectrum during the P → M (1s, 2s, 6s) and EP → ZM, ZP → EM (Xs) photoisomerization processes were computed using 175, 242, 233 trajectories for 1s-P, 2s-P, 6s-P, respectively, and 220 and 179 trajectories for Xs-EP and XS-ZP within our simulations. These calculations stem from nonadiabatic dynamics simulation outcomes, factoring in state energy, oscillator strengths, and the instantaneous electronic state of all trajectories throughout the simulation. To calculate the fluorescence intensity at each point in time, we employed a 10 fs time step,

aggregating the oscillator strengths of all trajectories that remained in the excited state at that moment. It's worth mentioning that this calculation approach is succinctly outlined here; for a more comprehensive theoretical framework, readers are encouraged to consult the works of Lan *et al*.[157] and Jin *et al.*[158]

The emission intensity $II(\omega,t)^{emission}$ at time *t* is calculated as follows:

$$I(\omega,t)^{emission} \propto \omega^3 \sum_{i=1}^{N_1} f(\omega_i,t)\delta(\omega-\omega_i)$$

Here, $f(\omega_i,t)$ represents the oscillator strength of the *i*th trajectory at time *t*, and N_1 is the number of trajectories remaining in the S_1 excited state. The cumulative emissions over time and frequency domains are given by:

$$I(t)^{emission} = \int I(\omega,t)^{emission} d\omega$$

and

$$I(\omega)^{emission} = \int I(\omega,t)^{emission} dt$$

The two-dimensional contour plot displaying the fluorescence emission intensity across both time and frequency domains are shown in **Figures 4.18 (a), 4.19 (a), and 4.20 (a)** for 1s-P, 2s-P, and 6s-P, and in **Figures 4.21 (a)** and **4.22 (a)** for Xs-EP and Xs-ZP. These plots reveal ultrafast quenching of fluorescence emissions before 700, 260, 340 fs for 1s-P, 2s-P, and 6s-P, and 760, 1320 fs for Xs-EP and Xs-ZP, alongside a noticeable red-shift in the emission photon's wavenumber. Additionally, the figures include wavelength-resolved fluorescence emission spectra at various times: 100-650, 50-250, 80-300 fs for 1s-P, 2s-P, and 6s-P, and 100-750, 100-1200 fs for Xs-EP and Xs-ZP. Taking **Figure 4.18 (b)** as an instance, the central wavenumber of the emission spectrum shifts from about 1.50×10^4 cm^{-1} at 100 fs to roughly 0.25×10^4 cm^{-1} at 650 fs, with the intensity at the latter time point being significantly diminished (approximately one-sixth of its initial value). This observation underscores the red-shift and quenching of the fluorescence

emission spectrum. Given the fluorescence emission quenching times of around 700, 260, 340 fs for 1s-P, 2s-P, 6s-P, and 760, 1320 fs for Xs-EP and Xs-ZP, which are considerably shorter than the lifetimes of the S_1 excited state (2560, 1160, 2400 fs for 1s-P, 2s-P, 6s-P, and 850, 1580 fs for Xs-EP and Xs-ZP respectively), it is inferred that a "dark state" plays a role during the photoisomerization processes of these molecules. The durations of the "dark state" in the photoisomerization process, determined through nonadiabatic dynamics simulations for 1s-P, 2s-P, 6s-P, Xs-EP, and Xs-ZP, are detailed in **Table 4.18**. It's found that the "dark state" durations for 1s, 2s, and 6s span 1.86, 0.90, and 2.06 ps, markedly longer than the 0.09 and 0.26 ps for Xs-EP and Xs-ZP, respectively.

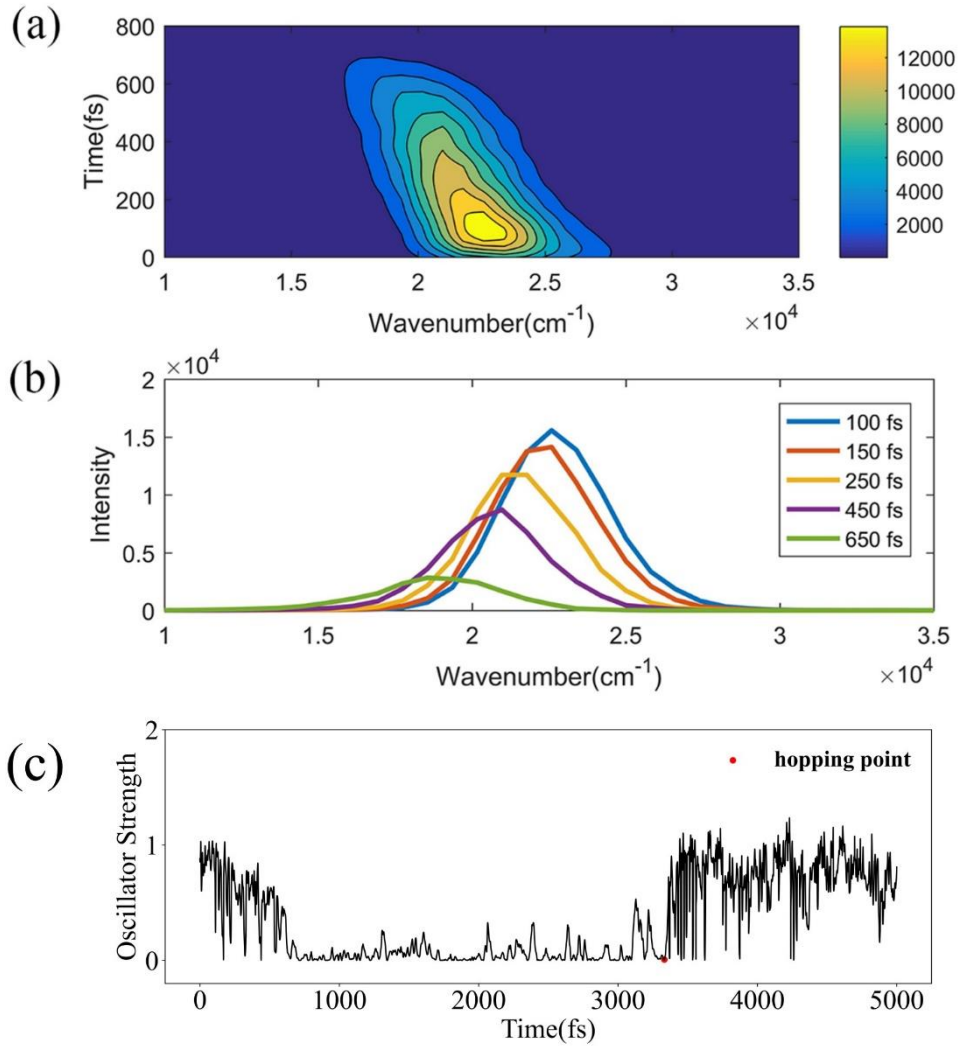

Figure 4.18 The simulated time-dependent fluorescence emission spectrum of 1s: (a) a

two-dimensional contour plot that illustrates the emission intensity in relation to both the simulation time and the wavenumber of photons; (b) fluorescence emission spectrum at various times; (c) The oscillator strength between the ground state (S_0) and the first excited state (S_1). The hopping time is displayed by a red point.

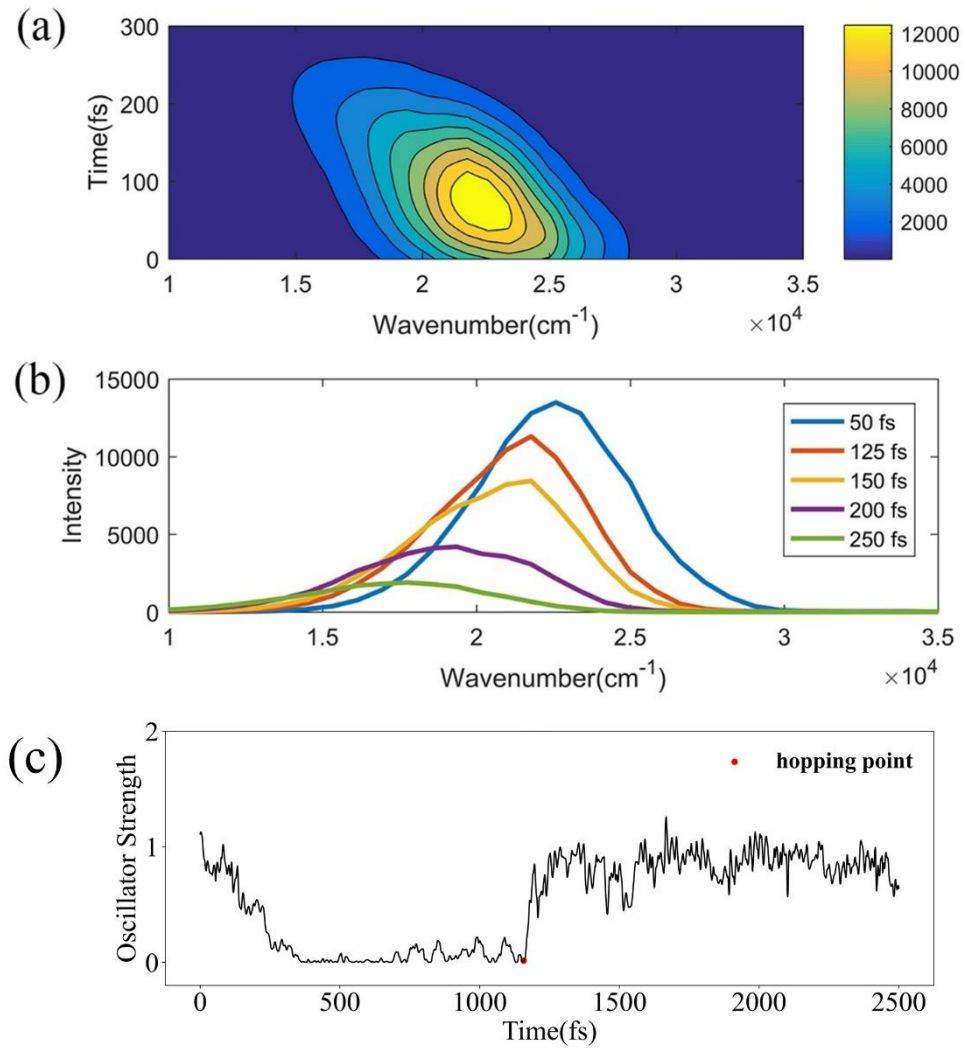

Figure 4.19 The simulated time-dependent fluorescence emission spectrum of 2s: (a) a two-dimensional contour plot that illustrates the emission intensity in relation to both the simulation time and the wavenumber of photons; (b) fluorescence emission spectrum at various times; (c) The oscillator strength between the ground state (S_0) and the first excited state (S_1). The hopping time is displayed by a red point.

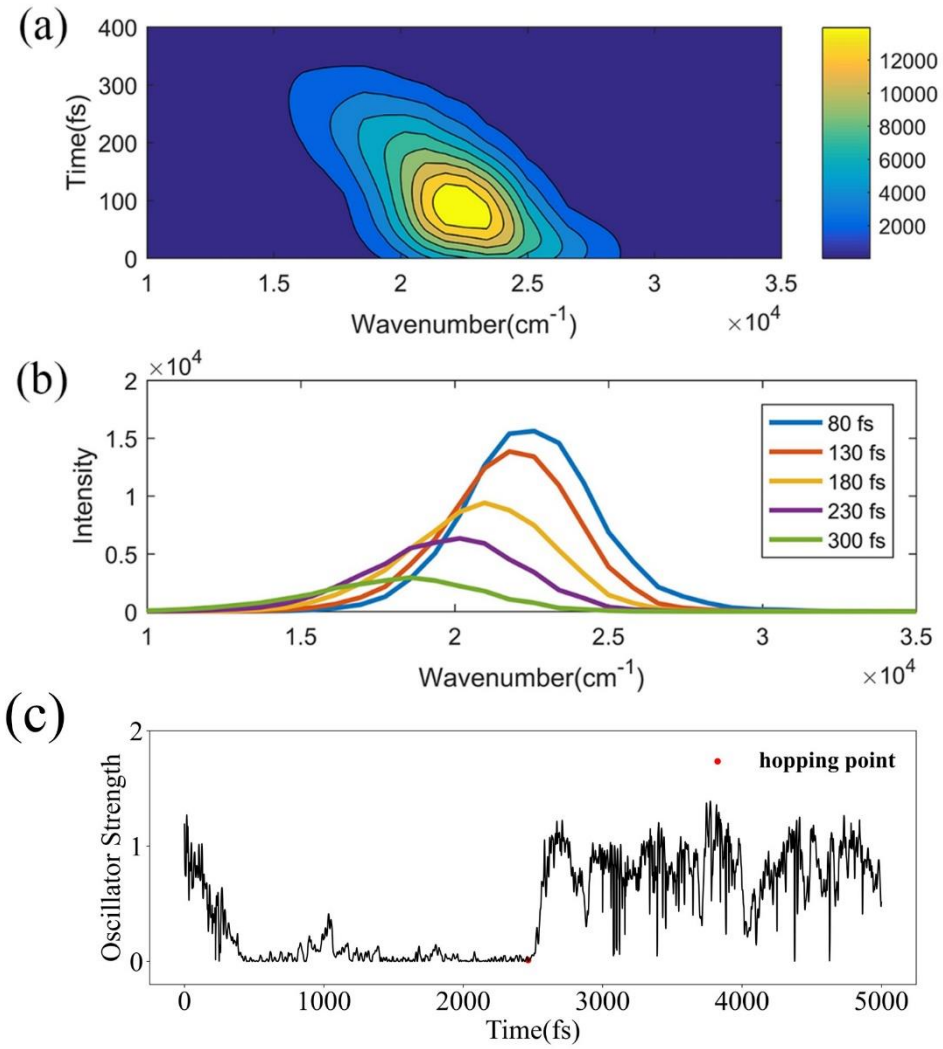

Figure 4.20 The simulated time-dependent fluorescence emission spectrum of 6s: (a) a two-dimensional contour plot that illustrates the emission intensity in relation to both the simulation time and the wavenumber of photons; (b) fluorescence emission spectrum at various times; (c) The oscillator strength between the ground state (S_0) and the first excited state (S_1). The hopping time is displayed by a red point.

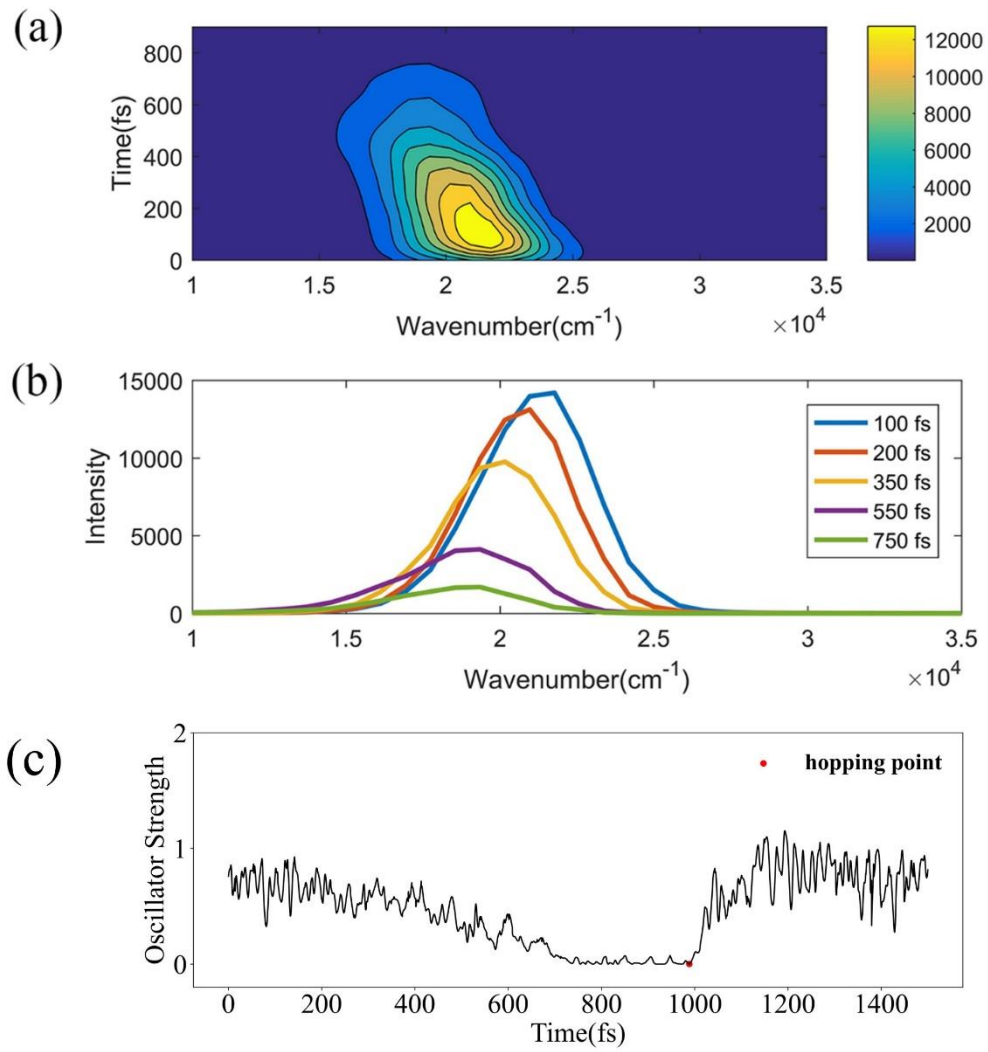

Figure 4.21 The simulated time-dependent fluorescence emission spectrum of Xs-EP: (a) a two-dimensional contour plot that illustrates the emission intensity in relation to both the simulation time and the wavenumber of photons; (b) fluorescence emission spectrum at various times; (c) The oscillator strength between the ground state (S_0) and the first excited state (S_1). The hopping time is displayed by a red point.

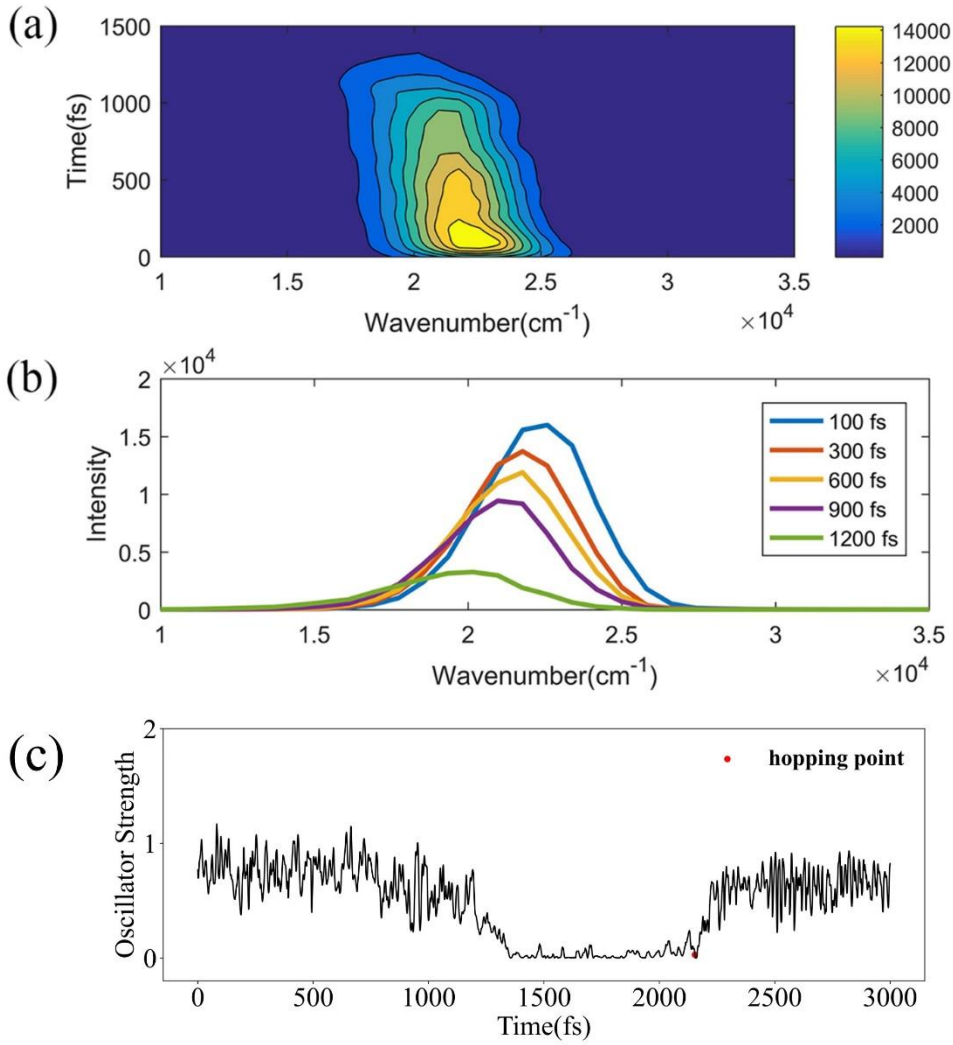

Figure 4.22 The simulated time-dependent fluorescence emission spectrum of Xs-ZP: (a) a two-dimensional contour plot that illustrates the emission intensity in relation to both the simulation time and the wavenumber of photons; (b) fluorescence emission spectrum at various times; (c) The oscillator strength between the ground state (S_0) and the first excited state (S_1). The hopping time is displayed by a red point.

Table 4.18 The average lifetime, the time of fluorescence emission quenching, and dark state duration for four motors.

		Average lifetime (ps)	Time of fluorescence emission quenching (ps)	Dark state duration (ps)
1s	P	2.56	0.70	1.86
2s	P	1.16	0.26	0.90
6s	P	2.40	0.34	2.06
Xs	EP	0.85	0.76	0.09
	ZP	1.58	1.32	0.26

4.4 Conclusions

In this study, we have introduced a novel molecular motor featuring unidirectional rotational motion through theoretical design. The comprehensive exploration began with the determination of all geometries encompassing conformational changes and the CI point during the photoisomerization rotation of molecular motors, namely 1s, 2s, 6s, and Xs, utilizing both OM2/MRCI and DFT calculations. The optimization of transition state geometries involved various theoretical methods, revealing the occurrence of two THI barriers during anticlockwise rotation. Significantly, the newly designed molecular motor Xs was identified to possess an exceptionally lower THI barrier compared to 1s, 2s, and 6s, suggesting a substantial acceleration in its rotational speed in comparison to the aforementioned motors. The study further delved into the Uv-vis absorption spectrum and frontier orbitals, which were calculated at the PBE0-D3 level. The results indicated a noteworthy red-shift in the maximum absorption wavelength of the newly designed molecular motor Xs, consistent with OM2/MRCI results. Additionally, a conspicuous reduction in the HOMO-LUMO gap was observed, contributing to the overall red-shifting of the Uv-vis absorption spectrum.

TSH simulations at the OM2/MRCI level were employed to investigate the photoisomerization process of 1s, 2s, 6s, and Xs. Remarkably, it was observed that the average lifetime of EP → ZM for Xs is shorter than that of 1s, 2s, and 6s molecular motors.

Similarly, ZP → EM is shorter than for 1s and 6s but slightly longer than 2s, with no significant impairment in the quantum yield of the newly designed molecular motor. Calculated time-dependent fluorescence emission spectrum results demonstrated that the "dark state" duration of 1s, 2s, and 6s is significantly longer than that of Xs-EP and Xs-ZP.

In summary, the computational results indicate that the newly proposed light-driven molecular rotary motor Xs exhibits a low thermal helix potential barrier and a simultaneous red-shift in visible light absorption wavelength. In comparison to DDPYM, improvements have been observed in both the UV-visible absorption spectrum and the THI barrier. This work is anticipated to stimulate further research into the design and synthesis of new families of molecular rotary motors.

Chapter 5 Theoretical study of NH_2^+

5.1 Introduction

Dissociative recombination (DR) is an essential process in astrophysical plasmas found in the upper atmosphere, interstellar medium, and planetary magnetospheres and plays a significant role in the evolution of ionization and chemistry in these environments. DR is a chemical reaction in which a positive molecular ion recombines with a free electron and breaks into two or more neutral atomic or molecular combinations. Therefore, studying the branching ratios of DR is essential for understanding the evolution of interstellar molecular species.[159–161] DR reactions can be classified into direct and indirect processes.[162] In the direct process, molecular ions are directly stimulated from the ground state of the cation to the dissociative excited states of the neutral species, while in the indirect process, molecules hop from the ground state of the cation to the dissociative excited state via the Rydberg excited state of the neutral species located below the ground state of the cation. These processes have been regarded as a tremendous challenge in experimental and theoretical studies because they proceed in highly-excited electronic states, including Rydberg and ionized continuum states.[163]

In theoretical studies, multichannel quantum defect theory (MQDT)[164,165] can effectively describe the Rydberg state electrons involved in the DR reaction. Tashiro and Kato[166] studied the DR of H_3^+ using quantum dynamics and showed that the Rydberg state plays a pivotal role in the predissociation of H_3. For H_2O, Nkambule[167] computed a combination of electronic structure and scattering calculations along with quasidiabtic potential energy surfaces for both bound Rydberg and electronic resonant states at the multireference configuration-interaction level to determine cross sections resulting from the indirect mechanism of the DR reaction. In dynamics applications, we have used surface-hopping ab initio molecular dynamics (SH-AIMD) simulations to study the branching ratios and nonadiabatic dynamics of the DR reactions for $HCNH^+$[168] H_3O^+[169]

HD_2O^+[170] and CH_3^+[13] The study of $HCNH^+ + e^-$ shows that the dissociation products HNC and HCN are produced at approximately the same branching ratio. This result suggests that $HCNH^+$ is a precursor for both HNC and HCN in interstellar space, confirmed by quantum wave-packet simulations on the same system in two-dimensional configuration space[171] In the study on $H_3O^+ + e^-$, two Rydberg excited states and three valence excited states were included in the SH-AIMD simulations, and the experimental branching ratios were qualitatively reproduced in the simulations.[169] In addition, a similar approach was employed in the DR reaction of HD_2O^+ to investigate isotope effects on branching ratios and dynamics.[170] The simulations showed that the leaving D atom tends to have more considerable kinetic energy than the leaving H atom. In the latest study on the direct process of the CH_3^+ DR reaction, 96% of the trajectories led to CH_2 + H, while 4% to CH + 2H, CH + H_2, and C + H_2 + H, which is different from the experimental observation. Then, by incorporating the Rydberg state's approximate potential energy surface into the indirect process simulation, we reproduced the experimental branching ratio of the products.[172]

Recently, dimensionality reduction methods such as linear algorithms like principal component analysis (PCA)[173,174] and classical multidimensional scaling (CMDS)[175,176] as well as nonlinear algorithms like ISOMAP[177] and Locally Linear Embedding (LLE)[178] have been applied to analyze and visualize the trajectory evolution. Lan *et al.*[179] employed the ISOMAP and CMDS methods to investigate the behavior of molecular motion in nonadiabatic dynamics simulations. Their study revealed the reactive coordinates that cause nonadiabatic decay for the $CH_2NH_2^+$ and PΦB systems. The results showed that ISOMAP and CMDS can compress information on patterns of molecular motion in nonadiabatic dynamics, taking symmetry into account. Le *et al.*[180] applied PCA and UMAP[181] methods to identify the reaction coordinates of solvent molecules involved in chemical reactions. This demonstrates that both PCA and UMAP can locate the appropriate water from the solution and the specific solvent molecules participating in the

reaction. In our previous work, we used the CMDS method to visualize intrinsic reaction coordinates (IRCs) and reaction path networks consisting of equilibrium and transition state geometries connected by IRCs of $OH^- + CH_3F \rightarrow CH_3OH + F^-$ and Au_5 cluster;[182] a reduced dimensional map shows the appropriate location in low-dimensional coordinate space for each structure to describe the reaction process. Based on this CMDS, the reaction space projector (ReSPer) method[183] was developed, and the photoreaction dynamics of stilbene was studied using a "multi-state energy landscape" constructed with this method. This successfully explained the previously established photoreaction processes of cis-stilbene and 1,1′-dimethyl-cis-stilbene, providing valuable insights into photochemical reactions.[184]

Moreover, Li *et al.*[185] used the ISOMAP and LLE methods to analyze the reactive and non-reactive trajectories of the multichannel reaction $NH^+ + H_2 \rightarrow N + H_3$ / $NH_2^+ +$ H simulated by Quasi-classical-trajectory (QCT)[186,187] calculations on potential energy surfaces. With the help of the trajectory analysis, it was shown that the competition between the two H-atom abstraction reactions is due to two different capture paths. Furthermore, the specificity of this reaction's vibrational and rotational modes was studied using the initial state-selected QCT method; the results showed that vibration and rotation could promote different channels by enhancing the effective capture of H-H bond stretching vibrations.[188] Hence, the dimensionality reduction method is expected to be effective for analyzing factors affecting DR reaction products' branching ratio in the dynamics process.

The DR reaction of NH_2^+ also plays a crucial role in interstellar chemistry. Relevant experimental results suggest that N + H + H is the primary dissociation product of NH_2^+. The total branching ratios of the DR of NH_2^+ for all the possible product channels are reported as follows[189]

$$NH_2^+ + e^- \rightarrow [NH_2]^* \rightarrow \begin{cases} N + H_2 & (0.00) \\ NH + H & (0.34) \\ N + H + H & (0.66) \end{cases}$$

In this study, SH-AIMD simulations based on the Zhu-Nakamura method are employed to simulate the direct process of the DR reaction for NH_2^+ and to discuss the branching ratio of NH_2^+ in the electronic excited state. We first examine the mechanism of this reaction by calculating the energy diagrams of the relevant species in the ground and excited states. The momentum at the hopping points of all trajectories is then analyzed using CMDS to explore the relationship between the momentum distribution and the variational mode. This approach not only elucidates the role of the momentum distribution at the hopping points in the dynamic processes and enhance our comprehension of DR reaction but also marks the pioneering application of the CMDS method for analyzing momentum distribution.

5.2. Computational Details

5.2.1 Zhu-Nakamura-based SH-AIMD

The Zhu-Nakamura-based SH-AIMD method has been applied in the exploration of photochemical reactions,[190–196] and reported benchmark shows an excellent accuracy.[197] The avoided crossing point along trajectory propagation was detected and global nonadiabatic switching probability are given by:

$$P^{\mathrm{ZN}} = exp\left[-\frac{\pi}{4\sqrt{a^2}}\sqrt{\frac{2}{b^2+\sqrt{|b^4\pm 1|}}}\right] \qquad 5.2.1$$

Two unitless parameters effective coupling and effective collision energy can be expressed as follows:

$$a^2 = \frac{\hbar^2}{2\mu}\frac{\sqrt{|F_1F_2|}|F_1-F_2|}{2{V_{12}}^3} \qquad 5.2.2$$

and

$$b^2 = (E_t - E_X)\frac{|F_2-F_1|}{\sqrt{|F_1F_2|}(2V_{12})} \qquad 5.2.3$$

where F_1 and F_2 are the forces of two diabatic potential energy surfaces, V_{12} is the diabatic coupling, and μ is the reduced mass of the diatomic molecule. E_X is the energy at the

crossing point, and it is the sum of potential energy and kinetic energy component in the direction of the nonadiabatic coupling vector. At the avoided crossing point, the multidimensional forces acting on the system are converted into one-dimensional forces in eq (2) and eq (3) given by:

$$\frac{|F_2-F_1|}{\sqrt{\mu}} = \sqrt{\sum_{i=1}^{N}\frac{1}{m_i}\sum_{\alpha=x,y,z}\left(F_2^{i\alpha}-F_1^{i\alpha}\right)^2} \qquad 5.2.4$$

and

$$\frac{\sqrt{F_2F_1}}{\sqrt{\mu}} = \sqrt{\left|\sum_{i=1}^{N}\frac{1}{m_i}\sum_{\alpha=x,y,z}F_2^{i\alpha}F_1^{i\alpha}\right|} \qquad 5.2.5$$

where N is the number of nuclei in a molecule with the mass m_i, a stand for x, y, and z component of Cartesian coordinates for the ith nucleus. Detailed description along with definition of hopping direction and momentum change can be found in ref.[198]

5.2.2 CMDS method

Dimension reduction converts the high-dimensional data set $A_{md'}$ into low-dimensional data space $z_{md'}$ while preserving the original data distribution.

$$A = \begin{bmatrix} a_{11} & \cdots & a_{1d} \\ \vdots & \ddots & \vdots \\ a_{m1} & \cdots & a_{md} \end{bmatrix} \qquad 5.2.6$$

$$Z = \begin{bmatrix} z_{11} & \cdots & z_{1d'} \\ \vdots & \ddots & \vdots \\ z_{m1} & \cdots & z_{md'} \end{bmatrix} \qquad 5.2.7$$

where m is the number of data points, d is the dimension of the originally high-dimensional space, and d' is the dimension of the newly low-dimensional space ($d' < d$. In the present study, the originally high-dimensional data sets consist of the momentum at the surface hopping points. The $3N$ Cartesian coordinates, Cartesian coordinates momentum, normal coordinates, mass-weighted normal mode Cartesian coordinates momentum of the NH_2^+ system constitute the row vector in matrix A, respectively. The input matrix A needs to be transformed into a distance matrix D, which can be expressed

as:

$$\begin{bmatrix} d_{11} & \cdots & d_{1d} \\ \vdots & \ddots & \vdots \\ d_{m1} & \cdots & d_{md} \end{bmatrix} \quad 5.2.8$$

where each element d_{ij} represents the distance between two coordinates or momentums of the original high-dimensional space, can be defined as:

$$d_{ij} = \sqrt{\sum_{k=1}^{3N} \left(Q_i^k - Q_j^k\right)^2} \quad 5.2.9$$

Q_i^k and Q_j^k denote the kth (mass-weighted normal mode Cartesian/Cartesian) coordinate or (mass-weighted normal mode Cartesian/Cartesian) momentum of the ith and jth geometry, and the distance of a pair of molecular (mass-weighted normal mode Cartesian/Cartesian) coordinate or (mass-weighted normal mode Cartesian/Cartesian) momentum Q_i and Q_j are estimated by the root-mean-square deviation (RMSD). The orientation of coordinates and momentum are determined through use of quaternions algorithm[199] , ensuring that both coordinates and momentum maintain the same orientation as the equilibrium structure.

To get the inner matrix B, Yong-householder transformation (or double centering) was applied to calculate internal matrix B.

$$B = -\frac{1}{2}\left(E - \frac{1}{n}1\right) D^2 \left(E - \frac{1}{n}1\right)^T \quad 5.2.10$$

where E is the identity matrix (or unit matrix) for dimension n,1 is one's matrix. Since the inner matrix is a real symmetric, positive definite matrix, thus we know that it will have real eigenvalues. Then, the eigenvalues of matrix B are decomposed:

$$B = V\Lambda V^T = V\Lambda^{\frac{1}{2}}\Lambda^{\frac{1}{2}}V^T \quad 5.2.11$$

$$Z = \Lambda^{\frac{1}{2}}V^T \quad 5.2.12$$

This study reduced high-dimensional space (mass-weighted normal mode

Cartesian/Cartesian) coordinate and (mass-weighted normal mode Cartesian/Cartesian) momentum into two dimensions. Thus, the reduced coordinate and momentum components PC_1 and PC_2, related to the two largest eigenvalues and their eigenvectors, are the two most important dimensions in the reduced space Z; after the dimensionality reduction, the evolution with snapshots of each coordinate and momentum becomes a scatter distribution in the XY line plot. The distribution of data points in the reduced dimensional coordinate and momentum space can provide a direct view of the coordinate and momentum distinction in the original high-dimensional momentum space. All analysis codes were written in Python language.

5.3 Results and discussion

5.3.1 Electronic structure and energy diagram for DR reaction of $NH_2^+ + e^-$

In the DR process, NH_2^+ captures a free electron roaming in the environment, formatting the excited states of NH_2, then NH_2 was dissociated into products. To investigate the possible reaction pathways through electronic excited states for the DR reaction of $NH_2^+ + e^-$, the electronic structure calculations were carried out by the full valence state-averaged complete active space multiconfigurational self-consistent field (SA-CASSCF) and multireference Rayleigh-Schrödinger second-order perturbation theory (CASPT2) methods[200] with the SapporoTZP2012 basis set, using the Molpro 2012 program package. It is shown that the ground state of NH_2^+ is the triplet state, with the singlet state lying above approximately 1.46 eV at the CASPT2 level. **Figure 5.1** shows electronic configurations of the triplet and singlet states with molecular orbitals at the equilibrium geometry of the triplet ground state of NH_2^+ at the CASSCF level (r(NH) = 1.057 Å and a(NHN) = 153.083 degrees). With the collision of an electron and NH_2^+, the additional electron is captured by NH_2^+ and entered one of the virtual valence orbitals of the NH_2 molecule. The CASPT2 energies at the NH_2^+ triplet geometry indicates that the

nine valence-excited states of NH_2 are related to the DR of NH_2^+. **Figure 5.2** shows the relative energies of the related electronic states of NH_2, NH_2^+, and the dissociative products, N + H + H, NH + H, and N + H_2 at the SA-CASSCF and CASPT2 levels, in which the energy of NH_2 cation is zero. SA-CASSCF gives a poor estimation of the relative energy of NH_2^+ and NH_2 because of no consideration of the dynamical correlation effects. Regarding the electronic states of NH_2, the SA-CASSCF energies are qualitatively in agreement with the CASPT2 energies, as shown in **Figure 5.2**. Therefore, SA-CASSCF method with the SapporoTZP2012 basis set was employed in the surface hopping AIMD simulations.

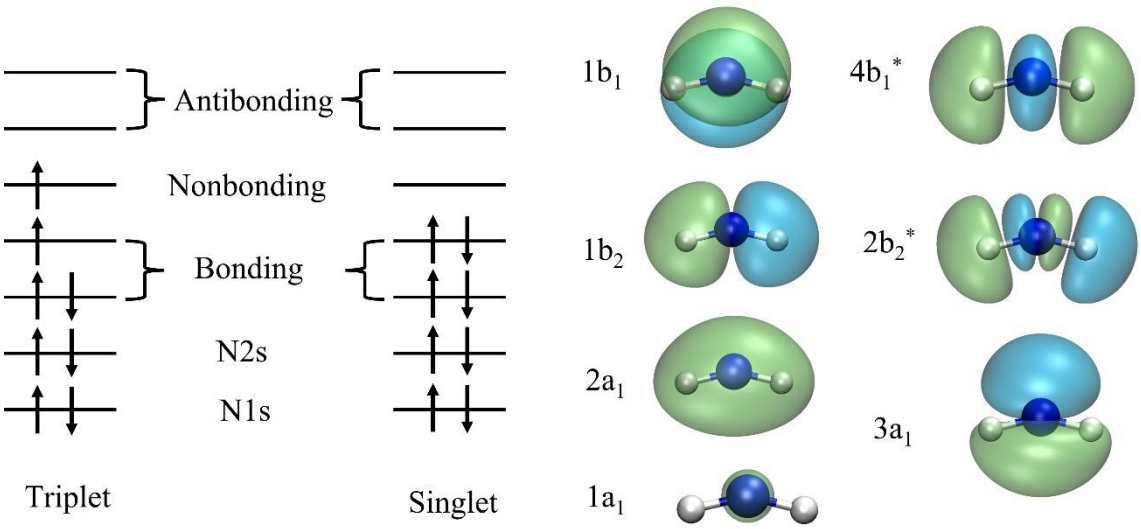

Figure 5.1. The electronic configurations of the triplet and singlet states of NH_2^+ with molecular orbitals.

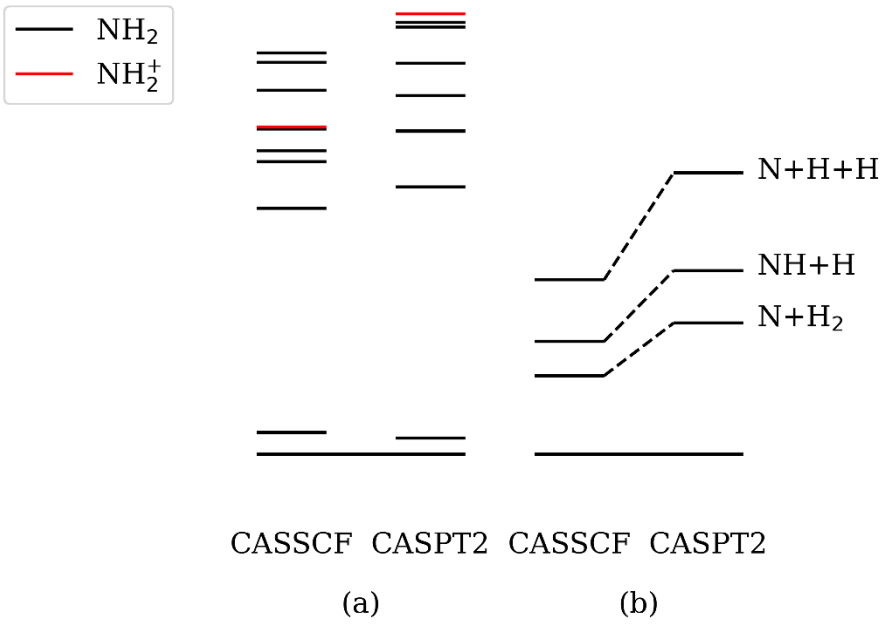

Figure 5.2 Relative energies of (a) the electronic states of NH_2 and NH_2^+, and (b) the dissociative products N + H + H, NH + H, N + H_2 at the SA-CASSCF and CASPT2 levels.

4.3.2 Surface hopping AIMD simulation for dissociation process

The DR reactions in interstellar space should occur under very low-temperature conditions. Therefore, initial conditions for the dynamic's simulations were generated based on the ground state equilibrium structure, and atomic velocities were randomly obtained by a Wigner distribution at 0 K. The simulation starts from the ninth excited PES of neutral NH_2, which corresponds to the NH_2^+ cation, and transitions to the ninth excited state without a change of energy after capturing a free electron. The SA-CASSCF calculations were carried out, in which nine excited states are averaged with equal weights, and full-valence orbitals are included in the active space. The surface hopping AIMD simulations were performed for the excited states of the NH_2 starting from 1000 initial conditions of C_1 symmetry in which each trajectory was run over 100 fs with a fixed time step of 0.1 fs. In the present simulation, the trajectory propagation along the PES

sometimes encounters convergence problems because the character of significant orbitals and low-lying electronic states can change in different regions of the configurational space, which was restricted by the active space and the number of averaged states. The nine electronic states often come close to each other, resulting in no convergence in the SA-CASSCF calculation. To avoid the difficulty in the convergence along the trajectory, we reduced the number of averaged states in SA-CASSCF calculations after hopping to a lower excited state. The criterion was established for the dissociative products involved to determine the branching ratio of the final products as follows:

(1) NH+H: One N-H bond exceeds 1.5 Å while the other N-H bonds are less than 1.5 Å.

(2) N+H+H: Two N-H bond exceeds 1.5 Å while the H-H bond exceeds 1.5 Å.

(3) N+H_2: Two N-H bond exceeds 1.5 Å while the H-H bond is less than 1.5 Å.

Surface hopping AIMD simulations were systematically performed for the dissociation process of NH_2 after capturing a free electron. We ran 1000 trajectories starting from the eighth excited state; 62 trajectories did not occur dissociation reaction; thus, 938 trajectories were included to estimate the branching ratio. Among them, NH_2 dissociates into NH + H in 234 trajectories (25%), into N + H + H in 648 trajectories (73%), and into N + H_2 in 20 (2%). The branching ratio of the dissociative products has been quantitatively reproduced in the present simulation compared with experimental value[189] NH+H (34%), N+H+H (66%), N+H_2(0%), which can be used to discuss the dynamic tendency.

To understand the dissociation process of NH_2 in detail, The changes of potential energies of the ground state and eight excited states of NH_2 → NH+H along one example trajectory are presented in **Figure 5.3 (a)**, and the variation tendency of the distance between N_1-H_2, N_1-H_3, H_2-H_3 is plotted in **Figure 5.3 (b)**. As can be seen, the surface hopping simulation was started from the eighth excited state, and the distance between N_1-H_2 and N_2-H_3 gradually increased from 1.2 Å and 2.0 Å to more than 8 Å while the

distance of N_1-H_3 was unchanged with slight oscillations. For the potential energy, with the approaching of the potential energy of excited states, the excited state transition occurs as an excited state at t = 32.6 fs (8 → 7), t = 42.6 fs (7 → 6), t = 43.2 fs (6 → 5) and t = 44.4 fs (5 → 4) respectively. After hopping to the seventh excited state at 32.6 fs, the number of averaged states was reduced from 9 to 8, so the adiabatic energies are not continuous. The discontinuous point in adiabatic potential energy was also observed at t = 42.6 fs, where the character of the sixth excited state changes with the seventh excited state not included in the state average. The average states were reduced from 6 to 5 at t = 43.2 fs because surface hopping occurred. The trajectory eventually reaches the fourth excited state at t = 44.4 fs, which can be considered the dissociation process for NH_2 forming of NH + H was accomplished.

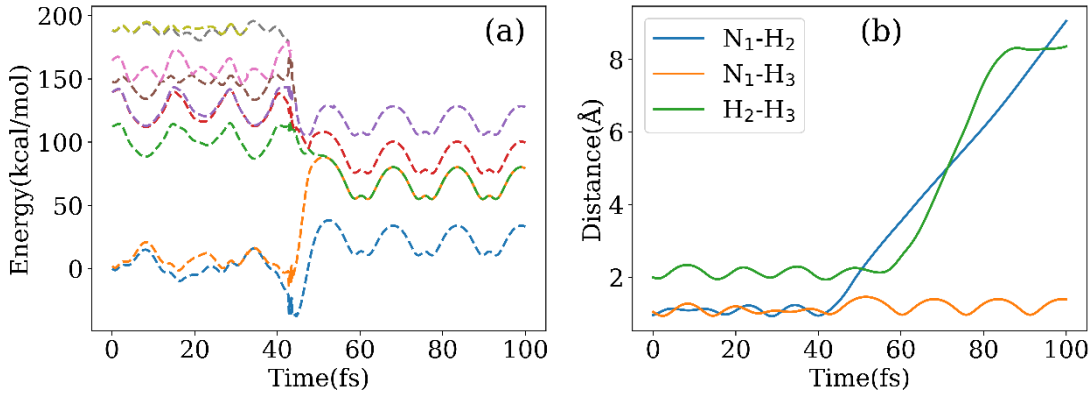

Figure 5.3 (a) The potential energy change for dissociating NH_2 → NH + H reaction channel, (b) the N_1-H_2, H_1-H_2, H_2-H_3 interatomic distance along NH_2 → NH + H reaction trajectory.

To illustrate the dissociation process of NH_2 → N + H + H, we show the changes of potential energies along one example trajectory in **Figure 5.4 (a),** including the ground state and eight excited states. The distance between each atom as the function of time is shown in **Figure 5.4 (b)**. For the dissociation process of NH_2 → N + H + H, the molecule runs on the excitation potential energy surface when the NH_2 is pumped to the eighth

excited state. During the trajectory propagation, N_1-H_2, N_1-H_3, and H_2-H_3 distance increases from their initial distance of 1.2, 1.2, and 2.0 Å to 3.4, 5.0, and 6.0 Å. Meanwhile, with the departure of H_2 and H_3, the potential energy difference between the eighth and seventh excited states is gradually decreased, and the surface hopping occurs at t = 24.1 fs (8 → 7), t = 37.1 fs (7 → 6), t = 48.7 fs (6 → 5), respectively. After hopping to the seventh excited state at 24.1 fs, the number of average states was reduced from 9 to 8; thus, the discontinuous adiabatic potential energies point was observed at t = 24.1 fs, then the excited state transition occurs at t = 37.1 fs where the averaged states change with that the seventh excited state is not involved in the state average. The propagation of the trajectory eventually reaches the fifth excited state at t = 48.7 fs, and the dissociation process of NH_2 → N + H + H was accomplished. One can see that the four adiabatic states of NH_2 → N + H + H comes close to each other drastically, as shown in **Figure 5.4 (a)**, which indicates that the electronic configuration was changed with the increase of distance between each atom for NH_2, and residual states become degenerate in the final state of trajectory. The propagation of trajectories always gets a convergence problem at such degeneracy regions due to spin symmetry.

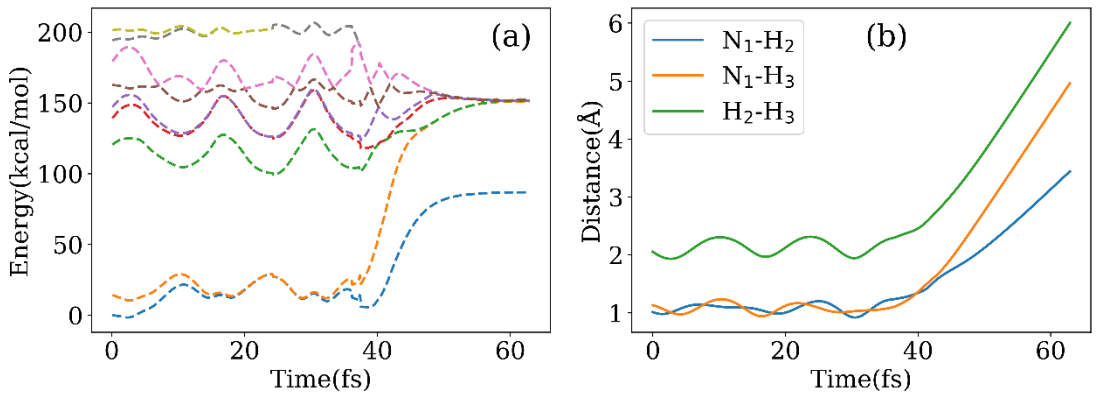

Figure 5.4 (a) The change of potential energy for dissociating NH_2 → N + H + H reaction channel, (b) the N_1-H_2, H_1-H_2, H_2-H_3 interatomic distance along NH_2 → N + H + H reaction trajectory.

5.3.3 CMDS analysis for initial conditions and hopping points

In present simulations, the experimental branching ratio of the NH_2 dissociation reaction has been qualitatively reproduced, and the dissociation product N + H_2 should be ignored because of its small proportion. First, the distribution pattern of all initial coordinates, initial momentum, initial normal coordinates, and initial normal mode momentum was investigated by the CMDS method, as shown in **Figure 4.5** The blue and red point corresponds to products N + H + H and NH + H, respectively. It is observed that reduced dimensional coordinate and momentum displays a disorder distribution in low-dimensional space; this suggests that random initial coordinates, initial momentum, initial normal coordinates, and initial normal mode momenta may not significantly contribute to the NH_2 dissociation reaction, which also can be recognized by the density of distribution pattern along the PC_1 and PC_2.

However, in further trajectory analysis, a fascinating distribution pattern in the low-dimensional space spanned by two reduced dimensional momenta was presented by the CMDS analysis of the hopping point in the trajectory propagation, as depicted in **Figure 5.6 (a)**. The first hopping point of all trajectories was plotted after CMDS calculations, with the blue point representing the trajectory leading to product N + H + H and the red point corresponding to product NH + H. One can see that the reduced dimensional momentum of all hopping points has been classified into two regions by the density of distribution pattern along the PC_1. In **Figure 5.6 (b)**, the color map illustrates the distribution of reduced-dimensional momentum alongside kinetic energy. This visualization emphasizes the identification of two distinct regions within the reduced-dimensional momentum. Specifically, the left region demonstrates lower kinetic energy compared to the right region. In **Figure 5.6 (c)**, the reduced-dimensional momentum of the second hopping point is depicted. Similarly, the two distinct colors signify two different products, and the color map represents kinetic energy. Notably, the classification tendency is evident in the second hopping point across all trajectories. Moving on to the

analysis of the momentum for the third hopping point in all trajectories, the CMDS method was applied, as illustrated in **Figures 5.6 (e)** and **5.6 (f)**. The obtained reduced-dimensional momentum for the third hopping point reveals a discernible classification tendency for all trajectories. Thus, it is evident that a certain factor influences the classification tendency of the hopping points along PC_1.

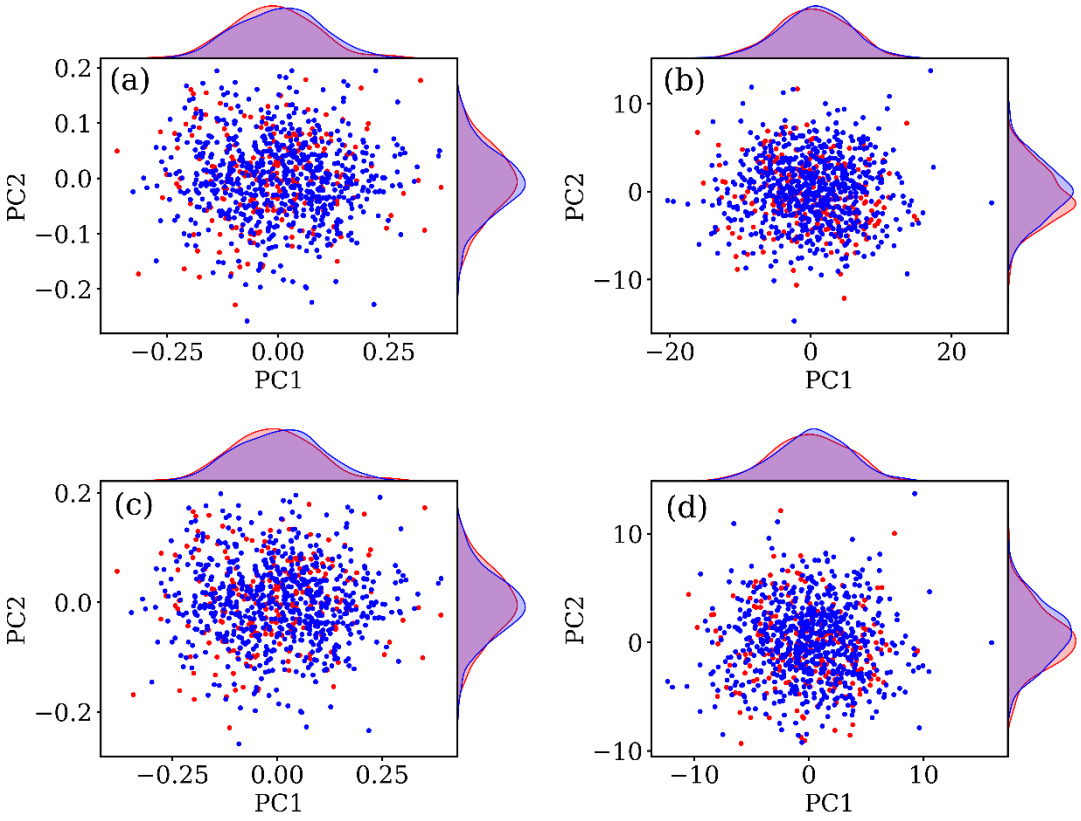

Figure 5.5 CMDS analysis of the (a) initial coordinate, (b) initial momentum, (c) initial mass-weighted normal mode coordinate, and (d) initial mass-weighted normal mode coordinate momentum.

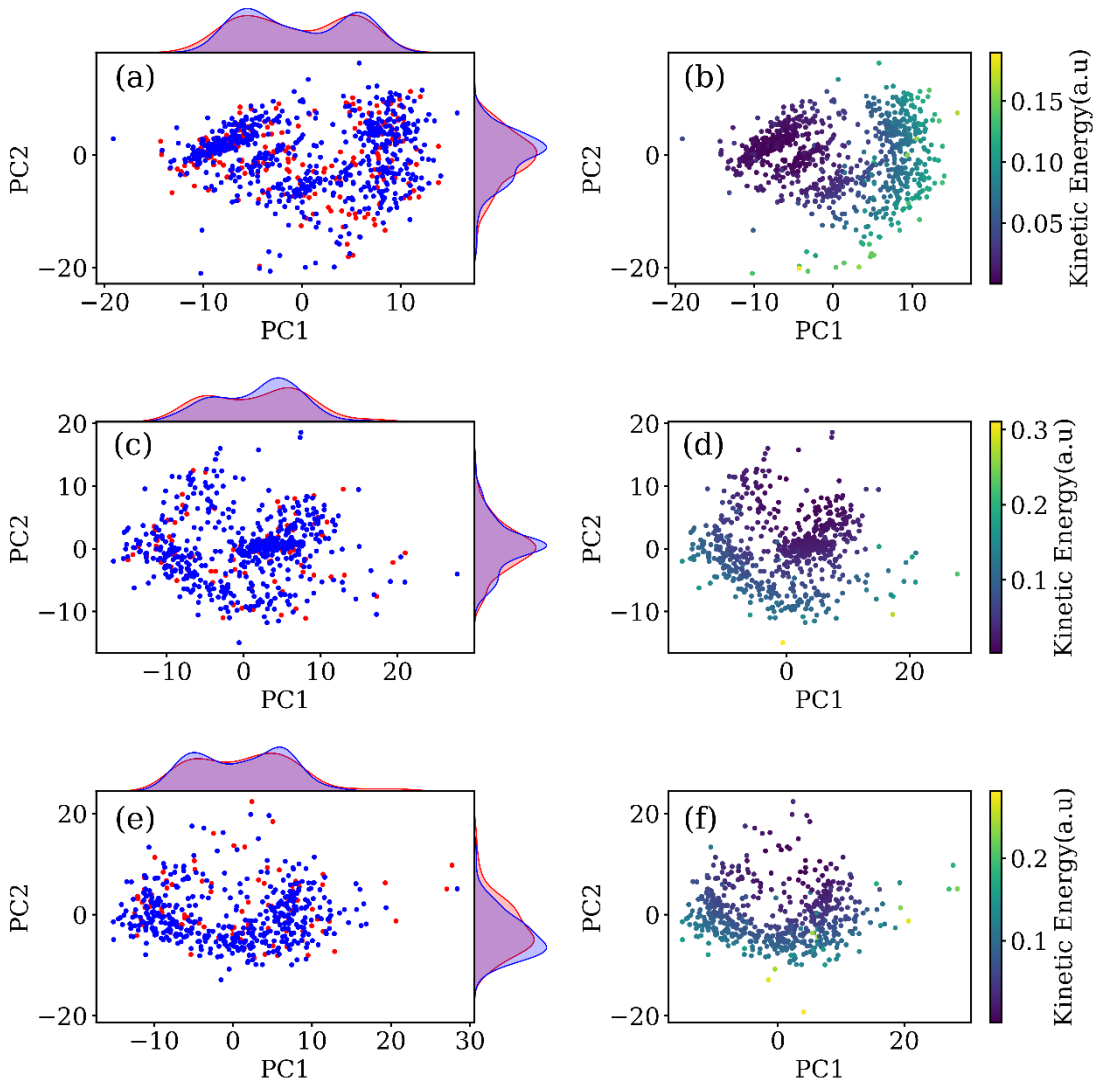

Figure 5.6 (a, c, e) CMDS analysis of the 1st, second, and third hopping point momentum for dissociation reaction of NH_2^++e^-. (b, d, f) CMDS analysis of the 1st, second, and third hopping point momentum for dissociation reaction of NH_2^++e^- with kinetic energy.

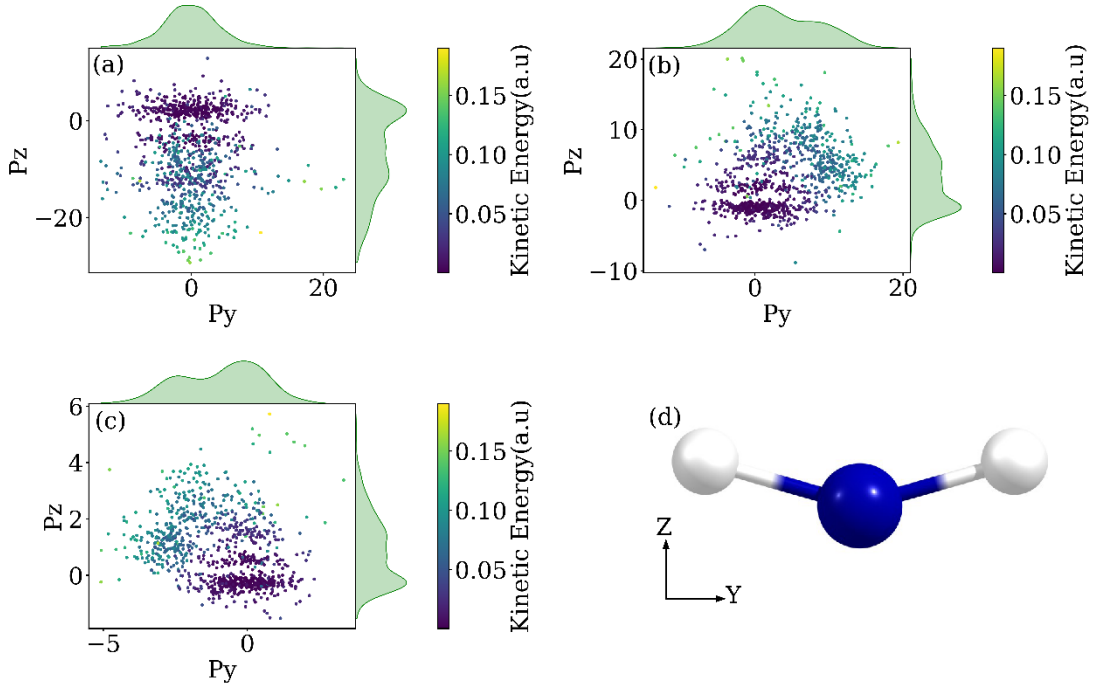

Figure 5.7 (a) The X and Z direction of the N_1 atom of momentum at first hopping points for the dissociation reaction of $NH_2^+ + e^-$, (b) the X and Z direction of the H_2 atom of momentum at first hopping points, (c) the X and Z direction of H_3 atom of momentum at first hopping points. (d) All first hopping points for dissociation reaction of $NH_2^+ + e^-$ with a coordinate axis.

Given that the classification tendency of the momentum for the first hopping point is more pronounced than that of the other two hopping points, the momentum of N_1, H_2, and H_3 along Y and Z directions at first hopping point is presented in **Figures 5.7 (a)**, **(b)** and **(c)**, while equilibrium geometries are shown in **Figure 5.7 (d)**. The coordinate and momentum of the X direction can be set to zero because the dissociation reaction occurs only on the plane. As shown in **Figure 5.7 (a)**, **(b)** and **(c)** the Py axis indicates the momentum of the N_1, H_2 and H_3 atom along the Y direction, and the Pz axis represents the momentum of the N_1 atom along the Z direction, and **Figure 5.7 (d)** presents the orientation of angle H_2-N_1-H_2 for equilibrium geometries.

The distribution of N_1 atom momentum can be clustered in two centers, in which the top half of **Figure 5.7 (a)** represents the momentum of N_1 along the Z positive direction, and the bottom half is the momentum of N_1 along the Z negative direction. For the $NH_2 \rightarrow NH + H$ reaction channel, when NH_2 molecule run to the first hopping point if the momentum direction of N_1 is orientated to the positive direction of Z, which is beneficial to N_1 atom approach H_2 or H_3 of the positive orientation of hopping point geometries, and vice versa. For the $NH_2 \rightarrow N + H + H$ pathway, when the NH_2 molecule ran to the first hopping point if the momentum direction of N_1 is orientated to the negative direction of Z, which is beneficial to N_1 atom departure H_2 and H_3.

The distribution of H_2 and H_3 in **Figures 5.7 (b)** and **5.7 (c)** indicates a noticeable trend in classification. Specifically, the lower right corner of **Figure 5.7 (b)** and the lower left corner of **Figure 5.7 (c)** correspond to the momentum of H_2 and H_3 along the negative Z direction. Conversely, the upper left corner of **Figure 5.7 (b)** and the upper right corner of **Figure 5.7 (c)** depict the momentum in the positive Z direction. For the $NH_2 \rightarrow NH + H$ reaction channel, an important observation arises during the NH_2 molecule's movement towards the first hopping point. When the momentum directions of H_2 and N_1 coincide, indicating an approach towards each other, and concomitantly, the momentum directions of H_3 and N_1 diverge, signifying a movement away from each other, it proves advantageous for the formation of the NH + H product. For the $NH_2 \rightarrow N + H + H$ pathway, When the momentum direction of N_1 and H_2 is pointing away from each other, and simultaneously the momentum direction of N_1 and H_2 is also oriented away from each other, which is beneficial to form N + H + H product. This insight underscores the significance of the momentum directions in influencing the reaction pathway and product outcome at the first hopping point.

According to the obtained momentum distribution for these three atoms, the momentum distribution of the H_2 and H_3 atom is similar to the reduced dimensional momentum of **Figure 5.6 (a)**, but the distribution direction. It implies that the momentum

direction of H_2 and H_3 can be regarded as the essential component of reduced dimensional momentum space according to the principle of the CMDS method. Thus, all trajectories' CMDS analysis hopping points extracted two significant momentum distribution patterns. This provides a straightforward way to build the primary momentum direction responsible for the dissociation product and the three atoms' momentum distribution at the first hopping point may contribute to one reason for the momentum direction distribution classification tendency.

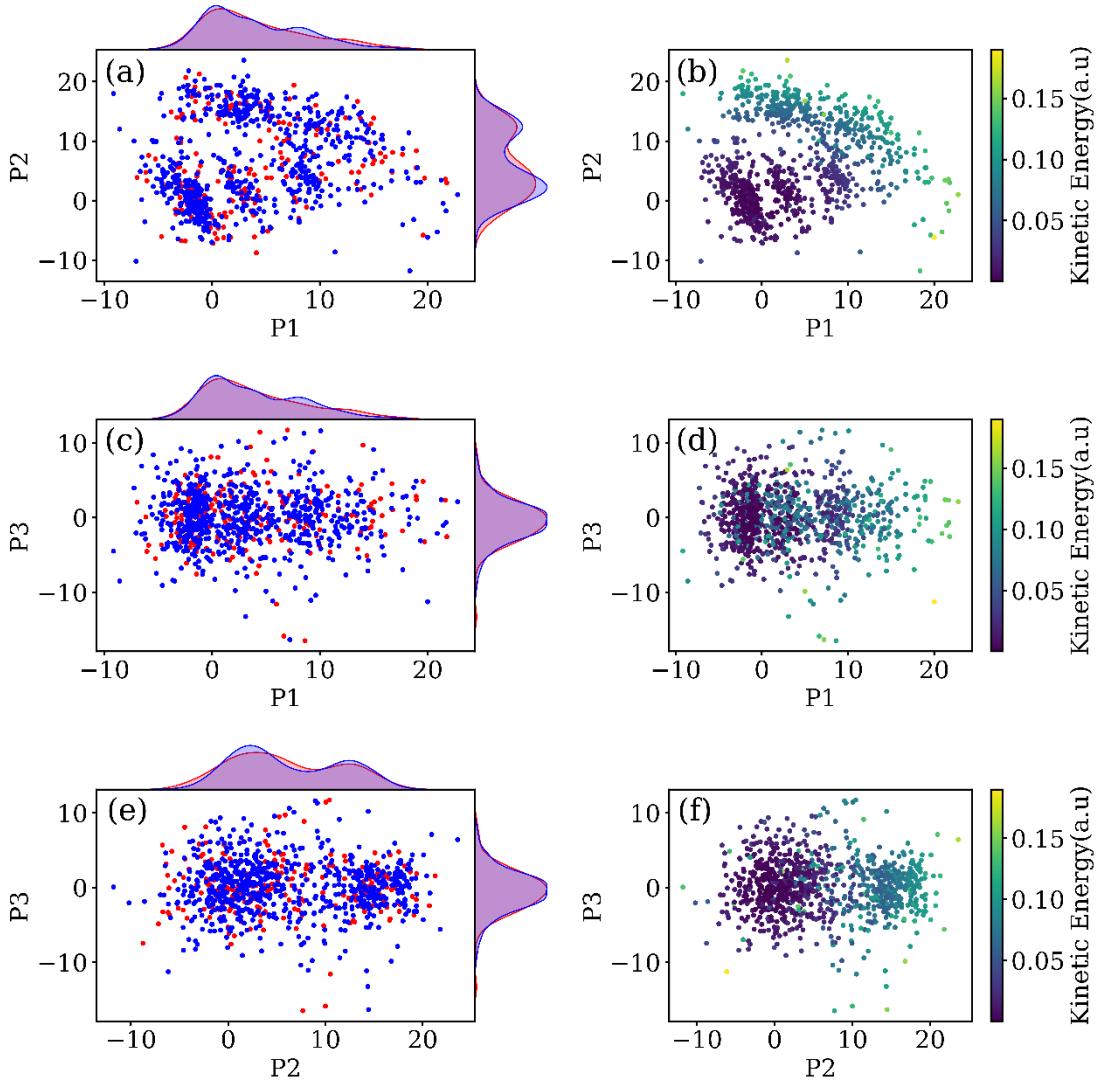

Figure 5.8 (a, c, e) the distribution of normal mode coordinate momentum along three vibrational directions, (b, d, f) the distribution of normal mode coordinate momentum along three vibrational directions with kinetic energy.

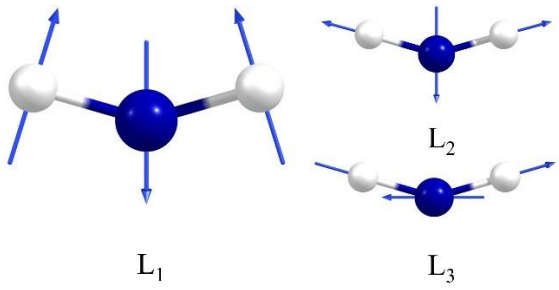

Figure 5.9 The ground state variational mode of NH_2 at equilibrium coordinate along L_1(scissoring), L_2(symmetric stretching), and L_3(asymmetric stretching).

Figure 5.8 presents the mass-weighted normal mode coordinates momentum of the first hopping point between each pair of modes. Additionally, **Figure 5.9** corresponds to the ground state variational modes of NH_2^+ at equilibrium coordinates along L_1 (scissoring), L_2 (symmetric stretching), and L_3 (asymmetric stretching). This visual representation provides a more intuitive perspective on the classification tendency of the hopping points. Similarly, it is observed that the mass-weighted normal mode coordinate momentum of the first hopping point is divided into two cluster centers along P_2 in **Figure 5.8 (a)**, **Figure 5.8 (e)** because of obvious peak of density distribution along P_2. Specifically, the internal motion L2 (symmetric stretching) of the NH_2^+ molecule can influence the momentum direction of both H_2 and H_3 through symmetric stretching as it traverses the potential energy surface. This additional perspective offers another means of elucidating the observed classification tendency in momentum distribution at the hopping point.

5.4 Conclusions

In this work, ab initial surface hopping simulation has been carried out for the

dissociative recombine reaction $NH_2^+ + e^-$ at the SA-CASSCF level to estimate the branching ratio of the dissociative products. The Zhu-Nakamura-based surface hopping has been applied to deal with the transition of the electronic state along the trajectory propagation, which simulates analytical nonadiabatic switching probability by the gradients of electronic adiabatic potential energy surfaces and their gradients. The energy diagram for the compounds, including the ground state of NH_2^+, the ground and excited states of NH_2, H + H + H, NH + H, and N + H_2, have been calculated at CASSCF and CASPT2 levels. The CASSCF and CASPT2 methods give the qualitatively energetic except for the energy level of NH_2^+. One thousand trajectories are simulated with the initial conditions that Wigner sampling is given to the respective normal vibrational modes of NH_2^+ with random phases, and the molecule is stimulated to the eighth excited of NH_2. The rates of the respective dissociative products are estimated as NH + H (25%), N + H + H (73%), and N + H_2 (2%), while the corresponding experimental ratio was reported as NH + H (34%), N + H + H (66%), N + H_2 (0%), which is qualitatively reproduced by directed trajectory simulations.

Moreover, the CMDS analysis of the hopping point was performed to explore the inner relation between the hopping point's momentum direction and the variational mode. While the CMDS method has traditionally been applied to analyze the conformation evolution of the coordinate in the ground state or nonadiabatic dynamics simulations. Our current work represents our initial efforts to use the CMDS approach to analyze the momentum distribution in nonadiabatic dynamics. This study displays that it is possible to build an inner connection between the momentum of hopping point and variational mode by extracting the molecule's primary momentum direction. The dimensionality reduction analysis of the hopping point's momentum during NH_2^+ dissociation reveals that several molecular momentums may contribute to the observed classification tendency, particularly the momentum direction of H_2 and H_3 at the hopping point. We believe this work may deepen the insight and understanding of the nonadiabatic dynamics process of

dissociative recombination reactions.

Chapter 6 General conclusion

Excited state reactions encompass a wide range of phenomena such as photochemical reactions and excited state dissociation reactions. When a chemical reaction involves electronic excited states, the nonadiabatic process leads to the transition of electronic state between different potential energy surfaces, corresponding to a breakdown of the Born-Oppenheimer approximation (BOA) and demanding a treatment of both the nuclei and the electrons. There are many chemical problems that involve excited electronic states from photochemistry to chemical synthesis, with applications in renewable energy and bioimaging. Therefore, it is a major challenge in the theoretical field to describe the behavior of both electrons and nuclei in the context of nonadiabatic effects and excited state chemical reactions. The trajectory surface hopping (TSH) dynamics can meet the challenge of simulating dynamics beyond the BOA, in which the electron is described under the quantum mechanics framework and nuclei is treated classically. The trajectories propagate on multi-state potential energy surfaces (PESs), resulting in complex changes in reaction processes along different degrees of freedom in geometries. This complexity makes it challenging to gain a deep understanding of the nature of excited state reactions and can lead to the omission of several crucial details of the dynamic processes. The classical Multidimensional Scaling (CMDS) method is a kind of dimensionality reduction method, which can be applied to analyze the trajectories of TSH for gaining a deeper understanding of dynamic processes.

Chapter 1 provides a general introduction, outlining the background of this thesis. In Chapter 2, I present the fundamental theory and concepts of excited state reaction dynamics simulation and the CMDS method.

In Chapter 3, the complete reaction route map of $SiCH_4$ on ground state is explored by the ADDF method, identifying two new dissociative reaction paths at B3LYP/def2-

svp level, including two dissociation reaction paths and four proton-transform paths. The photodynamic of $SiCH_4$ was investigated by means of Zhu-Nakamura based method surface hopping dynamics at MS-CASPT2/def2-svp level. Atomic coordinates and velocities are sourced from the zero-point vibrational state of $SiCH_4$, while the electronic state aligns with the S_1 state of $SiCH_4$.The resulting branching ratio of the dissociative products and proton-transform products shows different reaction paths, which can deepen the insight and understanding of the photodynamic process of $SiCH_4$.

In Chapter 4, the complete picture of the excited state chemical reaction of light-driven molecular rotary is obtained by a systematic theoretical study. According to the dynamic simulation results, we have advanced the field of light-driven molecular rotary motors (LDMRMs) by achieving two pivotal goals: lowering the thermal helix inversion (THI) barrier and extending the absorption wavelength into the visible spectrum. This study involves the structural reengineering of a second-generation visible LDMRM, resulting in the synthesis of a novel class, specifically, 2-((2S)-5-methoxy-2-methyl-2,3-dihydro-1H-cyclopenta[a]naphthalen-1-yl)-3-oxo-2,3-dihydro-1H-dibenzo[e,g]indole-6,9-dicarbonitrile. This redesigned motor stands out with its two photoisomerization stages and two thermal helix inversions, featuring exceptionally low THI barriers (4.00 and 2.05 kcal/mol at the OM2/MRCI level for the EM → EP and ZM → ZP processes, respectively). Moreover, it displays absorption wavelengths in the visible light range (482.98 and 465.76 nm for the EP and ZP isomers, respectively, at the TD-PBE0-D3/6-31G (d, p) level), surpassing its predecessors in efficiency, as indicated by the narrow HOMO-LUMO energy gap. Ultrafast photoisomerization kinetics (approximately 0.8-1.6 ps) and high quantum yields (around 0.3-0.6) are observed through trajectory surface hopping simulations. Additionally, the time-resolved fluorescence emission spectrum indicates a significantly reduced "dark state" duration (0.09 - 0.26 ps) in the newly designed LDMRMs compared to the original ones, marking a substantial leap forward in the design and efficiency of LDMRMs.

In Chapter 5, the direct process of the NH_2^+ DR mechanism is studied. Dissociative recombination (DR) of NH_2^+ is a chemical reaction in which a positive molecular ion NH2+ recombines with a free electron (e^-) and breaks into two or more neutral atomic or molecular combinations. In this process, molecular ions are directly stimulated from the ground state of the cation to the dissociative excited states of the neutral species NH_2 after capturing a free electron. Subsequently, the NH_2 dissociates into several fragments. This process is an essential process in the evolution of ionization and chemistry in astrophysical environments. Consequently, understanding the evolution of interstellar molecular species require studying the branching ratios of the NH_2^+ DR reaction. The dynamics of NH_2^+ dissociative recombination (DR) is explored using surface-hopping ab initio molecular dynamics (SH-AIMD) simulations at the state-averaged complete activate space self-consistent field (SA-CASSCF) level. This study incorporates the Zhu-Nakamura formalism to describe the potential energy curves crossing (nonadiabatic transitions between adiabatic electronic states) nature between the ground state and excited states of NH_2. Initial atomic coordinates and velocities are sourced from the zero-point vibrational state of NH_2^+, while the electronic state aligns with the eighth excited state of NH_2. The resulting branching ratio of the dissociative products, namely N + H + H and NH + H, shows a qualitative alignment with the experimental observations. The momentum at the hopping points of all trajectories is then analyzed using CMDS to explore the relationship between the momentum distribution and the variational mode, revealing the momentum at the hopping point is critically influenced by the variational mode, and enhance our comprehension of DR reaction.

In this thesis, I develop the SH-AIMD simulation program based on the Zhu-Nakamura algorithm. It is applied to investigate the photodynamics of $SiCH_4$ and the dynamics of NH_2+ dissociative recombination. Additionally, the momentum of NH_2^+ along the trajectory is investigated using the CMDS method. Furthermore, a new type of molecular motor is proposed, and its performance is evaluated through theoretical

calculations. Combining SH-AIMD and CMDS approaches provides a powerful theoretical tool for investigating reaction mechanisms and dynamics, as well as for proposing new functional molecules, in photochemistry. In the future, with further advancements in computational speed and theory, theoretical chemistry approaches are expected to become increasingly powerful not only in elucidating the reaction mechanisms but also in making predictions ahead of experimental validation.

Reference

1 D. G. Truhlar, B. C. Garrett and S. J. Klippenstein, Current Status of Transition-State Theory, *J Phys Chem*, 1996, **100**, 12771–12800.

2 D. Townsend, S. A. Lahankar, S. K. Lee, S. D. Chambreau, A. G. Suits, X. Zhang, J. Rheinecker, L. B. Harding and J. M. Bowman, The Roaming Atom: Straying from the Reaction Path in Formaldehyde Decomposition, *Science (1979)*, 2004, **306**, 1158–1161.

3 M. S. Quinn, K. Nauta, M. J. T. Jordan, J. M. Bowman, P. L. Houston and S. H. Kable, Rotational resonances in the H2CO roaming reaction are revealed by detailed correlations, *Science (1979)*, 2020, **369**, 1592–1596.

4 S. Maeda, T. Taketsugu, K. Ohno and K. Morokuma, From Roaming Atoms to Hopping Surfaces: Mapping Out Global Reaction Routes in Photochemistry, *J Am Chem Soc*, 2015, **137**, 3433–3445.

5 P. Klán and J. Wirz, in *Molecular Photoswitches*, 2022, pp. 1–18.

6 M. Baroncini, S. Silvi and A. Credi, *Chem Rev*, 2020, 120, 200–268.

7 J. Morstein and D. Trauner, in *Methods in Enzymology*, ed. D. M. Chenoweth, Academic Press, 2020, vol. 638, pp. 219–232.

8 N. Koumura, R. W. J. Zijlstra, R. A. van Delden, N. Harada and B. L. Feringa, Light-driven monodirectional molecular rotor, *Nature*, 1999, **401**, 152–155.

9 A. I. Florescu-Mitchell and J. B. A. Mitchell, Dissociative recombination, *Phys Rep*, 2006, **430**, 277–374.

10 K. I. Öberg, *Chem Rev*, 2016, 116, 9631–9663.

11 M. Hamberg, F. Österdahl, R. D. Thomas, V. Zhaunerchyk, E. Vigren, M. Kaminska, M. af Ugglas, A. Källberg, A. Simonsson, A. Paál, M. Larsson and W. D. Geppert, Experimental studies of the dissociative recombination processes for the dimethyl ether ions CD3OCD$_{2}^{+}$ and (CD3)2OD+, *A&A*.

12 S. Gozem, H. L. Luk, I. Schapiro and M. Olivucci, Theory and Simulation of the Ultrafast Double-Bond Isomerization of Biological Chromophores, *Chem Rev*, 2017, **117**, 13502–13565.

13 R. Improta, F. Santoro and L. Blancafort, *Chem Rev*, 2016, 116, 3540–3593.

14 G.-N. Porter and R. G. W. Norrish, Flash photolysis and spectroscopy. A new method for the study of free radical reactions, *Proc R Soc Lond A Math Phys Sci*, 1997, **200**, 284–300.

15 A. H. Zewail, Femtochemistry: Atomic-Scale Dynamics of the Chemical Bond, *J Phys Chem A*, 2000, **104**, 5660–5694.

16 H. H. Jaffe and A. L. Miller, The fates of electronic excitation energy, *J Chem Educ*, 1966, **43**, 469.

17 D. Sheppard, R. Terrell and G. Henkelman, Optimization methods for finding minimum energy paths, *J Chem Phys*, 2008, **128**, 134106.

18 K. Fukui, Role of Frontier Orbitals in Chemical Reactions, *Science (1979)*, 1982, **218**, 747–754.

19 C. Zener and R. H. Fowler, Non-adiabatic crossing of energy levels, *Proceedings of the Royal Society of London. Series A, Containing Papers of a Mathematical and Physical Character*, 1997, **137**, 696–702.

20 E. Teller, The Crossing of Potential Surfaces., *J Phys Chem*, 1937, **41**, 109–116.

21 F. Bernardi, M. Olivucci and M. A. Robb, Potential energy surface crossings in organic photochemistry, *Chem Soc Rev*, 1996, **25**, 321–328.

22 M. A. Robb, M. Garavelli, M. Olivucci and F. Bernardi, in *Reviews in Computational Chemistry*, 2000, pp. 87–146.

23 Y. Wu, J. Cao, H. Ma, C. Zhang, W. Bian, D. Nunez-Reyes and K. M. Hickson, Conical intersection–regulated intermediates in bimolecular reactions: Insights from C(1D) + HD dynamics, *Sci Adv*, 2024, **5**, eaaw0446.

24 H. Köuppel, W. Domcke and L. S. Cederbaum, in *Advances in Chemical Physics*, 1984, pp. 59–246.

25 B. F. E. Curchod and T. J. Martínez, *Chem Rev*, 2018, 118, 3305–3336.

26 H. Meyera) and W. H. Miller, A classical analog for electronic degrees of freedom in nonadiabatic collision processes, *J Chem Phys*, 1979, **70**, 3214–3223.

27 M. Amarouche, F. X. Gadea and J. Durup, A proposal for the theoretical treatment of multi-electronic-state molecular dynamics: Hemiquantal dynamics with the whole dim basis (HWD). A test on the evolution of excited Ar3+ cluster ions, *Chem Phys*, 1989, **130**, 145–157.

28 A. Jain and A. Sindhu, *ACS Omega*, 2022, 7, 45810–45824.

29 J. C. Tully, Molecular dynamics with electronic transitions, *J Chem Phys*, 1990, **93**, 1061–1071.

30 In *Introduction to Nonadiabatic Dynamics*, WORLD SCIENTIFIC, 2019, pp. 159–184.

31 T. Yonehara, K. Hanasaki and K. Takatsuka, Fundamental Approaches to Nonadiabaticity: Toward a Chemical Theory beyond the Born–Oppenheimer Paradigm, *Chem Rev*, 2012, **112**, 499–542.

32 C. Zhu and H. Nakamura, The two-state linear curve crossing problems revisited. II. Analytical approximations for the Stokes constant and scattering matrix: The Landau–Zener case, *J Chem Phys*, 1992, **97**, 8497–8514.

33 L. Wang, D. Trivedi and O. V. Prezhdo, Global flux surface hopping approach for mixed quantum-classical dynamics, *J Chem Theory Comput*, 2014, **10**, 3598–3605.

34 S. Ghosh, P. Verma, C. J. Cramer, L. Gagliardi and D. G. Truhlar, *Chem Rev*, 2018, 118, 7249–7292.

35 H. Lischka, D. Nachtigallová, A. J. A. Aquino, P. G. Szalay, F. Plasser, F. B. C. MacHado and M. Barbatti, *Chem Rev*, 2018, 118, 7293–7361.

36 D. A. Kreplin, P. J. Knowles and H.-J. Werner, MCSCF optimization revisited. II. Combined first- and second-order orbital optimization for large molecules, *J Chem Phys*, 2020, **152**, 074102.

37 H. Werner and W. Meyer, A quadratically convergent multiconfiguration–self-consistent field method with simultaneous optimization of orbitals and CI coefficients, *J Chem Phys*, 1980, **73**, 2342–2356.

38 H. Werner and W. Meyer, A quadratically convergent MCSCF method for the simultaneous optimization of several states, *J Chem Phys*, 1981, **74**, 5794–5801.

39 I. Shavitt, in *Methods of Electronic Structure Theory*, ed. H. F. Schaefer, Springer US, Boston, MA, 1977, pp. 189–275.

40 I. SHAVITT, The history and evolution of configuration interaction, *Mol Phys*, 1998, **94**, 3–17.

41 R. J. Buenker and S. D. Peyerimhoff, Individualized configuration selection in CI calculations with subsequent energy extrapolation, *Theor Chim Acta*, 1974, **35**, 33–58.

42 R. J. Buenker, S. D. Peyerimhoff and W. Butscher, Applicability of the multi-reference double-excitation CI (MRD-CI) method to the calculation of electronic wavefunctions and comparison with related techniques, *Mol Phys*, 1978, **35**, 771–791.

43 Kerstin. Andersson, P. Aake. Malmqvist, B. O. Roos, A. J. Sadlej and Krzysztof. Wolinski, Second-order perturbation theory with a CASSCF reference function, *J Phys Chem*, 1990, **94**, 5483–5488.

44 K. Andersson, P. Malmqvist and B. O. Roos, Second-order perturbation theory with a complete active space self-consistent field reference function, *J Chem Phys*, 1992, **96**, 1218–1226.

45 J. Finley, P.-Å. Malmqvist, B. O. Roos and L. Serrano-Andrés, The multi-state CASPT2 method, *Chem Phys Lett*, 1998, **288**, 299–306.

46 B. O. Roos, K. Andersson, M. P. Fülscher, P.-âke Malmqvist, L. Serrano-Andrés, K. Pierloot and M. Merchán, in *Advances in Chemical Physics*, 1996, pp. 219–331.

47 D. Zhang, M. R. Hermes, L. Gagliardi and D. G. Truhlar, Multiconfiguration Density-Coherence Functional Theory, *J Chem Theory Comput*, 2021, **17**, 2775–2782.

48 A. O. Lykhin, D. G. Truhlar and L. Gagliardi, Dipole Moment Calculations Using Multiconfiguration Pair-Density Functional Theory and Hybrid Multiconfiguration Pair-Density Functional Theory, *J Chem Theory Comput*, 2021, **17**, 7586–7601.

49 A. M. Sand, C. E. Hoyer, K. Sharkas, K. M. Kidder, R. Lindh, D. G. Truhlar and L. Gagliardi, Analytic Gradients for Complete Active Space Pair-Density Functional Theory, *J Chem Theory Comput*, 2018, **14**, 126–138.

50 M. Mostafanejad, M. D. Liebenthal and A. E. I. I. I. DePrince, Global Hybrid Multiconfiguration Pair-Density Functional Theory, *J Chem Theory Comput*, 2020, **16**, 2274–2283.

51 R. Pandharkar, M. R. Hermes, D. G. Truhlar and L. Gagliardi, A New Mixing of Nonlocal Exchange and Nonlocal Correlation with Multiconfiguration Pair-Density Functional Theory, *J Phys Chem Lett*, 2020, **11**, 10158–10163.

52 R. K. Carlson, D. G. Truhlar and L. Gagliardi, Multiconfiguration Pair-Density Functional Theory: A Fully Translated Gradient Approximation and Its Performance for Transition Metal Dimers and the Spectroscopy of Re2Cl82–, *J Chem Theory Comput*, 2015, **11**, 4077–4085.

53 G. Li Manni, R. K. Carlson, S. Luo, D. Ma, J. Olsen, D. G. Truhlar and L. Gagliardi, Multiconfiguration Pair-Density Functional Theory, *J Chem Theory Comput*, 2014, **10**, 3669–3680.

54 J. J. Bao, C. Zhou and D. G. Truhlar, Compressed-State Multistate Pair-Density Functional Theory, *J Chem Theory Comput*, 2020, **16**, 7444–7452.

55 D. Ghosh, J. Hachmann, T. Yanai and G. K.-L. Chan, Orbital optimization in the density matrix renormalization group, with applications to polyenes and β-carotene, *J Chem Phys*, 2008, **128**, 144117.

56 A. Baiardi and M. Reiher, The density matrix renormalization group in chemistry and molecular physics: Recent developments and new challenges, *J Chem Phys*, 2020, **152**, 040903.

57 N. M. Tubman, J. Lee, T. Y. Takeshita, M. Head-Gordon and K. B. Whaley, A deterministic alternative to the full configuration interaction quantum Monte Carlo method, *J Chem Phys*, 2016, **145**, 044112.

58 N. S. Blunt, S. D. Smart, J. A. F. Kersten, J. S. Spencer, G. H. Booth and A. Alavi, Semi-stochastic full configuration interaction quantum Monte Carlo: Developments and application, *J Chem Phys*, 2015, **142**, 184107.

59 B. O. Roos and K. Andersson, Multiconfigurational perturbation theory with level shift — the Cr2 potential revisited, *Chem Phys Lett*, 1995, **245**, 215–223.

60 G. Li Manni, I. Fdez. Galván, A. Alavi, F. Aleotti, F. Aquilante, J. Autschbach, D. Avagliano, A. Baiardi, J. J. Bao, S. Battaglia, L. Birnoschi, A. Blanco-González, S. I. Bokarev, R. Broer, R. Cacciari, P. B. Calio, R. K. Carlson, R. Carvalho Couto, L. Cerdán, L. F. Chibotaru, N. F. Chilton, J. R. Church, I. Conti, S. Coriani, J. Cuéllar-Zuquin, R. E. Daoud, N. Dattani, P. Decleva, C. de Graaf, M. G. Delcey, L. De Vico, W. Dobrautz, S. S. Dong, R. Feng, N. Ferré, M. Filatov(Gulak), L. Gagliardi, M. Garavelli, L. González, Y. Guan, M. Guo, M. R. Hennefarth, M. R. Hermes, C. E. Hoyer, M. Huix-Rotllant, V. K. Jaiswal, A. Kaiser, D. S. Kaliakin, M. Khamesian, D. S. King, V. Kochetov, M. Krośnicki, A. A. Kumaar, E. D. Larsson, S. Lehtola, M.-B. Lepetit, H. Lischka, P. López Ríos, M. Lundberg, D. Ma, S. Mai, P. Marquetand, I. C. D. Merritt, F. Montorsi, M. Mörchen, A. Nenov, V. H. A. Nguyen, Y. Nishimoto, M. S. Oakley, M. Olivucci, M. Oppel, D. Padula, R. Pandharkar, Q. M. Phung, F. Plasser, G. Raggi, E. Rebolini, M. Reiher, I. Rivalta, D. Roca-Sanjuán, T. Romig, A. A. Safari, A. Sánchez-Mansilla, A. M. Sand, I. Schapiro, T. R. Scott, J. Segarra-Martí, F. Segatta, D.-C. Sergentu, P. Sharma, R. Shepard, Y. Shu, J. K. Staab, T. P. Straatsma, L. K. Sørensen, B. N. C. Tenorio, D. G. Truhlar, L. Ungur, M. Vacher, V. Veryazov, T. A. Voß, O. Weser, D. Wu, X. Yang, D. Yarkony, C. Zhou, J. P. Zobel and R. Lindh, The OpenMolcas Web: A Community-Driven Approach to Advancing Computational Chemistry, *J Chem Theory Comput*, 2023, **19**, 6933–6991.

61 H.-J. Werner, P. J. Knowles, G. Knizia, F. R. Manby and M. Schütz, Molpro: a general-purpose quantum chemistry program package, *WIREs Computational Molecular Science*, 2012, **2**, 242–253.

62 W. Kohn, A. D. Becke and R. G. Parr, *Density Functional Theory of Electronic Structure*, 1996.

63 W. Kohn, A. D. Becke and R. G. Parr, Density Functional Theory of Electronic Structure, *J Phys Chem*, 1996, **100**, 12974–12980.

64 E. J. Baerends and O. V Gritsenko, A Quantum Chemical View of Density Functional Theory, *J Phys Chem A*, 1997, **101**, 5383–5403.

65 H. Chermette, Density functional theory: A powerful tool for theoretical studies in coordination chemistry, *Coord Chem Rev*, 1998, **178–180**, 699–721.

66 P. E. M. Siegbahn and M. R. A. Blomberg, DENSITY FUNCTIONAL THEORY OF BIOLOGICALLY RELEVANT METAL CENTERS, *Annu Rev Phys Chem*, 1999, **50**, 221–249.

67 L. Andrews and A. Citra, Infrared Spectra and Density Functional Theory Calculations on Transition Metal Nitrosyls. Vibrational Frequencies of Unsaturated Transition Metal Nitrosyls, *Chem Rev*, 2002, **102**, 885–912.

68 T. Ziegler and J. Autschbach, Theoretical Methods of Potential Use for Studies of Inorganic Reaction Mechanisms, *Chem Rev*, 2005, **105**, 2695–2722.

69 C. M. Marian and N. Gilka, Performance of the Density Functional Theory/Multireference Configuration Interaction Method on Electronic Excitation of Extended π-Systems, *J Chem Theory Comput*, 2008, **4**, 1501–1515.

70 B. Santra, A. Michaelides, M. Fuchs, A. Tkatchenko, C. Filippi and M. Scheffler, On the accuracy of density-functional theory exchange-correlation functionals for H bonds in small water clusters. II. The water hexamer and van der Waals interactions, *J Chem Phys*, 2008, **129**, 194111.

71 H. Hu and W. Yang, Free Energies of Chemical Reactions in Solution and in Enzymes with Ab Initio Quantum Mechanics/Molecular Mechanics Methods, *Annu Rev Phys Chem*, 2008, **59**, 573–601.

72 F. Neese, Prediction of molecular properties and molecular spectroscopy with density functional theory: From fundamental theory to exchange-coupling, *Coord Chem Rev*, 2009, **253**, 526–563.

73 C. J. Cramer and D. G. Truhlar, Density functional theory for transition metals and transition metal chemistry, *Physical Chemistry Chemical Physics*, 2009, **11**, 10757–10816.

74 A. J. Cohen, P. Mori-Sánchez and W. Yang, *Chem Rev*, 2012, 112, 289–320.

75 W. Thiel, Semiempirical quantum-chemical methods, *Wiley Interdiscip Rev Comput Mol Sci*, 2014, **4**, 145–157.

76 P. O. Dral, X. Wu, L. Spörkel, A. Koslowski, W. Weber, R. Steiger, M. Scholten and W.

Thiel, *J Chem Theory Comput*, 2016, 12, 1082–1096.

77 J. A. Pople, D. P. Santry and G. A. Segal, Approximate Self-Consistent Molecular Orbital Theory. I. Invariant Procedures, *J Chem Phys*, 1965, **43**, S129–S135.

78 J. Wang, in *Geometric Structure of High-Dimensional Data and Dimensionality Reduction*, ed. J. Wang, Springer Berlin Heidelberg, Berlin, Heidelberg, 2012, pp. 51–77.

79 M. Greenacre, P. J. F. Groenen, T. Hastie, A. I. D'Enza, A. Markos and E. Tuzhilina, Principal component analysis, *Nature Reviews Methods Primers*, 2022, **2**, 100.

80 J. B. Tenenbaum, V. de Silva and J. C. Langford, A Global Geometric Framework for Nonlinear Dimensionality Reduction, *Science (1979)*, 2000, **290**, 2319–2323.

81 S. T. Roweis and L. K. Saul, Nonlinear Dimensionality Reduction by Locally Linear Embedding, *Science (1979)*, 2000, **290**, 2323–2326.

82 A. D. Kirilin, L. O. Belova, S. P. Knyazev, A. V Lega, M. Yu. Petrov and E. A. Chernyshev, Organosilyl Isocyanates. Reactions with Hydrazine, 1,1-Dimethylhydrazine, and 1-Methyl-1-[2-(1-Methylhydrazino)ethyl]hydrazine and Structural and Electronic Characteristics, *Russ J Gen Chem*, 2005, **75**, 1930–1934.

83 A. D. Kirilin, L. O. Belova, V. G. Lakhtin, A. V Lega, M. Yu. Petrov and E. A. Chernyshev, (Chloromethyl)alkoxysilanes, Silethanes, and Silethenes in the Synthesis of Linear and Heterocyclic Compounds, *Russ J Gen Chem*, 2005, **75**, 1402–1405.

84 S. F. Thames and K. G. Panjnani, Organosilane polymer chemistry: A review, *Journal of Inorganic and Organometallic Polymers*, 1996, **6**, 59–94.

85 R. R. LeVier, M. L. Chandler and S. R. Wendel, in *Biochemistry of Silicon and Related Problems*, eds. G. Bendz, I. Lindqvist and V. Runnström-Reio, Springer US, Boston, MA, 1978, pp. 473–514.

86 B. Blom and M. Driess, in *Functional Molecular Silicon Compounds II: Low Oxidation States*, ed. D. Scheschkewitz, Springer International Publishing, Cham, 2014, pp. 85–123.

87 J. Oddershede, J. R. Sabine and G. H. F. Diercksen, in *Understanding Molecular Properties: A Symposium in Honour of Professor Carl Johan Ballhausen, held at The Royal Danish Academy of Sciences and Letters, April 4 and 5, 1986*, eds. J. Avery, J. P. Dahl and A. E. Hansen, Springer Netherlands, Dordrecht, 1987, pp. 465–480.

88 M. Ben-Nun and T. J. Martínez, Photodynamics of ethylene: ab initio studies of conical intersections, *Chem Phys*, 2000, **259**, 237–248.

89 D. Hollas, L. Šištík, E. G. Hohenstein, T. J. Martínez and P. Slavíček, Nonadiabatic Ab Initio Molecular Dynamics with the Floating Occupation Molecular Orbital-Complete Active Space Configuration Interaction Method, *J Chem Theory Comput*, 2018, **14**, 339–350.

90 S. Saade and H. G. A. Burton, Excited State-Specific CASSCF Theory for the Torsion of Ethylene, *J Chem Theory Comput*, , DOI:10.1021/acs.jctc.4c00212.

91 R. S. Grev, G. E. Scuseria, A. C. Scheiner, H. F. Schaefer and M. S. Gordon, Relative energies of silaethylene and methylsilylene, *J Am Chem Soc*, 1988, **110**, 7337–7339.

92 R. Walsh, Bond dissociation energy values in silicon-containing compounds and some of their implications, *Acc Chem Res*, 1981, **14**, 246–252.

93 H. J. Koehler and H. Lischka, A systematic investigation on the structure and stability of the lowest singlet and triplet states of Si2H4 and SiH3SiH and the carbon analogous compounds SiH2CH2, SiH3CH, CH3SiH, C2H4, and CH3CH, *J Am Chem Soc*, 1982, **104**, 5884–5889.

94 M. Pitonak † and H. Lischka *, Excited-state potential energy surfaces of silaethylene: a MRCI investigation, *Mol Phys*, 2005, **103**, 855–862.

95 G. Zechmann, M. Barbatti, H. Lischka, J. Pittner and V. Bonačić-Koutecký, Multiple pathways in the photodynamics of a polar π-bond: A case study of silaethylene, *Chem Phys Lett*, 2006, **418**, 377–382.

96 M. Barbatti, M. Ruckenbauer, J. J. Szymczak, A. J. A. Aquino and H. Lischka, Nonadiabatic excited-state dynamics of polar π-systems and related model compounds of biological relevance, *Physical Chemistry Chemical Physics*, 2008, **10**, 482–494.

97 M. Barbatti, A. J. A. Aquino and H. Lischka, A Multireference Configuration Interaction Investigation of the Excited-State Energy Surfaces of Fluoroethylene (C2H3F), *J Phys Chem A*, 2005, **109**, 5168–5175.

98 C. He, A. M. Thomas, B. B. Dangi, T. Yang, R. I. Kaiser, H.-C. Lee, B.-J. Sun and A. H. H. Chang, Formation of the Elusive Silylenemethyl Radical (HCSiH2; X2B2) via the Unimolecular Decomposition of Triplet Silaethylene (H2CSiH2; a3A″), *J Phys Chem A*, 2022, **126**, 3347–3357.

99 L. Yu, C. Xu, Y. Lei, C. Zhu and Z. Wen, Trajectory-based nonadiabatic molecular dynamics without calculating nonadiabatic coupling in the avoided crossing case: Trans↔cis photoisomerization in azobenzene, *Physical Chemistry Chemical Physics*,

2014, **16**, 25883–25895.

100 S. Maeda, T. Taketsugu, K. Morokuma and K. Ohno, Anharmonic Downward Distortion Following for Automated Exploration of Quantum Chemical Potential Energy Surfaces, *Bull Chem Soc Jpn*, 2014, **87**, 1315–1334.

101 S. Maeda, K. Ohno and K. Morokuma, Systematic exploration of the mechanism of chemical reactions: the global reaction route mapping (GRRM) strategy using the ADDF and AFIR methods, *Physical Chemistry Chemical Physics*, 2013, **15**, 3683–3701.

102 J. Finley, P.-Å. Malmqvist, B. O. Roos and L. Serrano-Andrés, The multi-state CASPT2 method, *Chem Phys Lett*, 1998, **288**, 299–306.

103 I. Fdez. Galván, M. Vacher, A. Alavi, C. Angeli, F. Aquilante, J. Autschbach, J. J. Bao, S. I. Bokarev, N. A. Bogdanov, R. K. Carlson, L. F. Chibotaru, J. Creutzberg, N. Dattani, M. G. Delcey, S. S. Dong, A. Dreuw, L. Freitag, L. M. Frutos, L. Gagliardi, F. Gendron, A. Giussani, L. González, G. Grell, M. Guo, C. E. Hoyer, M. Johansson, S. Keller, S. Knecht, G. Kovačević, E. Källman, G. Li Manni, M. Lundberg, Y. Ma, S. Mai, J. P. Malhado, P. Å. Malmqvist, P. Marquetand, S. A. Mewes, J. Norell, M. Olivucci, M. Oppel, Q. M. Phung, K. Pierloot, F. Plasser, M. Reiher, A. M. Sand, I. Schapiro, P. Sharma, C. J. Stein, L. K. Sørensen, D. G. Truhlar, M. Ugandi, L. Ungur, A. Valentini, S. Vancoillie, V. Veryazov, O. Weser, T. A. Wesołowski, P.-O. Widmark, S. Wouters, A. Zech, J. P. Zobel and R. Lindh, OpenMolcas: From Source Code to Insight, *J Chem Theory Comput*, 2019, **15**, 5925–5964.

104 M. Richter, P. Marquetand, J. González-Vázquez, I. Sola and L. González, SHARC: ab Initio Molecular Dynamics with Surface Hopping in the Adiabatic Representation Including Arbitrary Couplings, *J Chem Theory Comput*, 2011, **7**, 1253–1258.

105 M. Baroncini, S. Silvi and A. Credi, Photo- and Redox-Driven Artificial Molecular Motors, *Chem Rev*, 2020, **120**, 200–268.

106 H. Wang, H. K. Bisoyi, X. Zhang, F. Hassan and Q. Li, Visible Light-Driven Molecular Switches and Motors: Recent Developments and Applications, *Chemistry – A European Journal*, 2022, **28**, e202103906.

107 D. R. S. Pooler, A. S. Lubbe, S. Crespi and B. L. Feringa, Designing light-driven rotary molecular motors, *Chem Sci*, 2021, **12**, 14964–14986.

108 N. Koumura, R. W. J. Zijlstra, R. A. van Delden, N. Harada and B. L. Feringa, Light-driven monodirectional molecular rotor, *Nature*, 1999, **401**, 152–155.

109 N. Koumura, E. M. Geertsema, M. B. van Gelder, A. Meetsma and B. L. Feringa, Second

Generation Light-Driven Molecular Motors. Unidirectional Rotation Controlled by a Single Stereogenic Center with Near-Perfect Photoequilibria and Acceleration of the Speed of Rotation by Structural Modification, *J Am Chem Soc*, 2002, **124**, 5037–5051.

110 M. Guentner, M. Schildhauer, S. Thumser, P. Mayer, D. Stephenson, P. J. Mayer and H. Dube, Sunlight-powered kHz rotation of a hemithioindigo-based molecular motor, *Nat Commun*, 2015, **6**, 8406.

111 R. Wilcken, M. Schildhauer, F. Rott, L. A. Huber, M. Guentner, S. Thumser, K. Hoffmann, S. Oesterling, R. de Vivie-Riedle, E. Riedle and H. Dube, Complete Mechanism of Hemithioindigo Motor Rotation, *J Am Chem Soc*, 2018, **140**, 5311–5318.

112 D. I. Pattison and M. J. Davies, in *Cancer: Cell Structures, Carcinogens and Genomic Instability*, Birkhäuser Basel, Basel, 2006, pp. 131–157.

113 R. A. van Delden, N. Koumura, A. Schoevaars, A. Meetsma and B. L. Feringa, A donor–acceptor substituted molecular motor: unidirectional rotation driven by visible light, *Org Biomol Chem*, 2003, **1**, 33–35.

114 T. van Leeuwen, J. Pol, D. Roke, S. J. Wezenberg and B. L. Feringa, Visible-Light Excitation of a Molecular Motor with an Extended Aromatic Core, *Org Lett*, 2017, **19**, 1402–1405.

115 L. Pfeifer, M. Scherübl, M. Fellert, W. Danowski, J. Cheng, J. Pol and B. L. Feringa, Photoefficient 2nd generation molecular motors responsive to visible light, *Chem Sci*, 2019, **10**, 8768–8773.

116 D. Roke, M. Sen, W. Danowski, S. J. Wezenberg and B. L. Feringa, Visible-Light-Driven Tunable Molecular Motors Based on Oxindole, *J Am Chem Soc*, 2019, **141**, 7622–7627.

117 D. R. S. Pooler, D. Doellerer, S. Crespi and B. L. Feringa, Controlling rotary motion of molecular motors based on oxindole, *Organic Chemistry Frontiers*, 2022, **9**, 2084–2092.

118 L. Greb and J.-M. Lehn, Light-Driven Molecular Motors: Imines as Four-Step or Two-Step Unidirectional Rotors, *J Am Chem Soc*, 2014, **136**, 13114–13117.

119 D. Roke, S. J. Wezenberg and B. L. Feringa, Molecular rotary motors: Unidirectional motion around double bonds, *Proceedings of the National Academy of Sciences*, 2018, **115**, 9423–9431.

120 L. Greb, A. Eichhöfer and J.-M. Lehn, Synthetic Molecular Motors: Thermal N Inversion and Directional Photoinduced C N Bond Rotation of Camphorquinone Imines,

Angewandte Chemie International Edition, 2015, **54**, 14345–14348.

121 M. Filatov, M. Paolino, S. K. Min and K. S. Kim, Fulgides as Light-Driven Molecular Rotary Motors: Computational Design of a Prototype Compound, *J Phys Chem Lett*, 2018, **9**, 4995–5001.

122 J. C. Tully, Molecular dynamics with electronic transitions, *J Chem Phys*, 1990, **93**, 1061–1071.

123 T. Taketsugu, A. Tajima, K. Ishii and T. Hirano, Ab Initio Direct Trajectory Simulation with Nonadiabatic Transitions of the Dissociative Recombination Reaction HCNH+ + e– → HNC/HCN + H, *Astrophys J*, 2004, **608**, 323.

124 Y. Ootani, K. Satoh, A. Nakayama, T. Noro and T. Taketsugu, Ab initio molecular dynamics simulation of photoisomerization in azobenzene in the nπ∗ state, *J Chem Phys*, 2009, **131**, 194306.

125 M. Filatov, M. Paolino, S. K. Min and C. H. Choi, Design and photoisomerization dynamics of a new family of synthetic 2-stroke light driven molecular rotary motors, *Chemical Communications*, 2019, **55**, 5247–5250.

126 C. García-Iriepa, M. Marazzi, F. Zapata, A. Valentini, D. Sampedro and L. M. Frutos, Chiral Hydrogen Bond Environment Providing Unidirectional Rotation in Photoactive Molecular Motors, *J Phys Chem Lett*, 2013, **4**, 1389–1396.

127 J. Ma, S. Yang, D. Zhao, C. Jiang, H. Lan and F. Li, Design and Nonadiabatic Photoisomerization Dynamics Study of a Three-Stroke Light-Driven Molecular Rotary Motor, *Int J Mol Sci*, , DOI:10.3390/ijms23073908.

128 J. Ma, D. Zhao, L. Yu, C. Jiang, Z. Lan and F. Li, Simultaneously improving the efficiencies of photo- and thermal isomerization of an oxindole-based light-driven molecular rotary motor by a structural redesign, *Physical Chemistry Chemical Physics*, 2023, **25**, 12800–12809.

129 Gaussian 09, Revision D.01, M. J. Frisch, G. W. Trucks, H. B. Schlegel, G. E. Scuseria, M. A. Robb, J. R. Cheeseman, G. Scalmani, V. Barone, G. A. Petersson, H. Nakatsuji, X. Li, M. Caricato, A. V. Marenich, J. Bloino, B. G. Janesko, R. Gomperts, B. Mennucci, H. P. Hratchian, J. V. Ortiz, A. F. Izmaylov, J. L. Sonnenberg, D. Williams-Young, F. Ding, F. Lipparini, F. Egidi, J. Goings, B. Peng, A. Petrone, T. Henderson, D. Ranasinghe, V. G. Zakrzewski, J. Gao, N. Rega, G. Zheng, W. Liang, M. Hada, M. Ehara, K. Toyota, R. Fukuda, J. Hasegawa, M. Ishida, T. Nakajima, Y. Honda, O. Kitao, H. Nakai, T. Vreven,

K. Throssell, J. A. Montgomery, Jr., J. E. Peralta, F. Ogliaro, M. J. Bearpark, J. J. Heyd, E. N. Brothers, K. N. Kudin, V. N. Staroverov, T. A. Keith, R. Kobayashi, J. Normand, K. Raghavachari, A. P. Rendell, J. C. Burant, S. S. Iyengar, J. Tomasi, M. Cossi, J. M. Millam, M. Klene, C. Adamo, R. Cammi, J. W. Ochterski, R. L. Martin, K. Morokuma, O. Farkas, J. B. Foresman, and D. J. Fox, Gaussian, Inc., Wallingford CT, 2013.

130 X. Zhuang, J. Wang and Z. Lan, Photoinduced Nonadiabatic Decay and Dissociation Dynamics of Dimethylnitramine, *J Phys Chem A*, 2013, **117**, 4785–4793.

131 X. Pang, X. Cui, D. Hu, C. Jiang, D. Zhao, Z. Lan and F. Li, "Watching" the Dark State in Ultrafast Nonadiabatic Photoisomerization Process of a Light-Driven Molecular Rotary Motor, *J Phys Chem A*, 2017, **121**, 1240–1249.

132 A. Nikiforov, J. A. Gamez, W. Thiel and M. Filatov, Computational Design of a Family of Light-Driven Rotary Molecular Motors with Improved Quantum Efficiency, *J Phys Chem Lett*, 2016, **7**, 105–110.

133 M. Che, Y.-J. Gao, Y. Zhang, S.-H. Xia and G. Cui, Electronic structure calculations and nonadiabatic dynamics simulations of excited-state relaxation of Pigment Yellow 101, *Physical Chemistry Chemical Physics*, 2018, **20**, 6524–6532.

134 Y.-H. Zhang, X.-W. Sun, T.-S. Zhang, X.-Y. Liu and G. Cui, Nonadiabatic Dynamics Simulations on Early-Time Photochemistry of Spirobenzopyran, *J Phys Chem A*, 2020, **124**, 2547–2559.

135 Y.-J. Gao, X.-P. Chang, X.-Y. Liu, Q.-S. Li, G. Cui and W. Thiel, Excited-State Decay Paths in Tetraphenylethene Derivatives, *J Phys Chem A*, 2017, **121**, 2572–2579.

136 S.-H. Xia, M. Che, Y. Liu, Y. Zhang and G. Cui, Photochemical mechanism of 1,5-benzodiazepin-2-one: electronic structure calculations and nonadiabatic surface-hopping dynamics simulations, *Physical Chemistry Chemical Physics*, 2019, **21**, 10086–10094.

137 O. Weingart, Z. Lan, A. Koslowski and W. Thiel, Chiral Pathways and Periodic Decay in cis-Azobenzene Photodynamics, *J Phys Chem Lett*, 2011, **2**, 1506–1509.

138 Z. Lan, Y. Lu, O. Weingart and W. Thiel, Nonadiabatic Decay Dynamics of a Benzylidene Malononitrile, *J Phys Chem A*, 2012, **116**, 1510–1518.

139 Y.-T. Wang, X.-Y. Liu, G. Cui, W.-H. Fang and W. Thiel, Photoisomerization of Arylazopyrazole Photoswitches: Stereospecific Excited-State Relaxation, *Angewandte Chemie International Edition*, 2016, **55**, 14009–14013.

140 X. Pang, C. Jiang, Y. Qi, L. Yuan, D. Hu, X. Zhang, D. Zhao, D. Wang, Z. Lan and F. Li, Ultrafast unidirectional chiral rotation in the Z–E photoisomerization of two azoheteroarene photoswitches, *Physical Chemistry Chemical Physics*, 2018, **20**, 25910–25917.

141 G. Cui, Z. Lan and W. Thiel, Intramolecular Hydrogen Bonding Plays a Crucial Role in the Photophysics and Photochemistry of the GFP Chromophore, *J Am Chem Soc*, 2012, **134**, 1662–1672.

142 N. Otte, M. Scholten and W. Thiel, Looking at Self-Consistent-Charge Density Functional Tight Binding from a Semiempirical Perspective, *J Phys Chem A*, 2007, **111**, 5751–5755.

143 M. R. Silva-Junior and W. Thiel, Benchmark of Electronically Excited States for Semiempirical Methods: MNDO, AM1, PM3, OM1, OM2, OM3, INDO/S, and INDO/S2, *J Chem Theory Comput*, 2010, **6**, 1546–1564.

144 W. Thiel, Semiempirical quantum–chemical methods, *WIREs Computational Molecular Science*, 2014, **4**, 145–157.

145 T. W. Keal, M. Wanko and W. Thiel, Assessment of semiempirical methods for the photoisomerisation of a protonated Schiff base, *Theor Chem Acc*, 2009, **123**, 145–156.

146 W. Weber and W. Thiel, Orthogonalization corrections for semiempirical methods, *Theor Chem Acc*, 2000, **103**, 495–506.

147 Thiel, W. MNDO Program, Version7.0; Max-Planck-Institut fur Kohlenforschung: Mulheim, Germany, 2007.

148 T. W. Keal, A. Koslowski and W. Thiel, Comparison of algorithms for conical intersection optimisation using semiempirical methods, *Theor Chem Acc*, 2007, **118**, 837–844.

149 L. Du and Z. Lan, An On-the-Fly Surface-Hopping Program JADE for Nonadiabatic Molecular Dynamics of Polyatomic Systems: Implementation and Applications, *J Chem Theory Comput*, 2015, **11**, 1360–1374.

150 A. Prlj, D. Hollas and B. F. E. Curchod, Deciphering the Influence of Ground-State Distributions on the Calculation of Photolysis Observables, *J Phys Chem A*, 2023, **127**, 7400–7409.

151 G. Granucci, M. Persico and A. Zoccante, Including quantum decoherence in surface hopping, *J Chem Phys*, 2010, **133**, 134111.

152 W. C. Swope, H. C. Andersen, P. H. Berens and K. R. Wilson, A computer simulation

method for the calculation of equilibrium constants for the formation of physical clusters of molecules: Application to small water clusters, *J Chem Phys*, 1982, **76**, 637–649.

153 A. V Karnik and M. Hasan, in *Stereochemistry*, eds. A. V Karnik and M. Hasan, Elsevier, 2021, pp. 49–91.

154 M. Barbatti, M. Bondanza, R. Crespo-Otero, B. Demoulin, P. O. Dral, G. Granucci, F. Kossoski, H. Lischka, B. Mennucci, S. Mukherjee, M. Pederzoli, M. Persico, M. Pinheiro Jr, J. Pittner, F. Plasser, E. Sangiogo Gil and L. Stojanovic, Newton-X Platform: New Software Developments for Surface Hopping and Nuclear Ensembles, *J Chem Theory Comput*, 2022, **18**, 6851–6865.

155 J. Ma, D. Zhao, C. Jiang, Z. Lan and F. Li, Effect of Temperature on Photoisomerization Dynamics of a Newly Designed Two-Stroke Light-Driven Molecular Rotary Motor, *Int J Mol Sci*, , DOI:10.3390/ijms23179694.

156 A. Kazaryan, Z. Lan, L. V Schäfer, W. Thiel and M. Filatov, Surface Hopping Excited-State Dynamics Study of the Photoisomerization of a Light-Driven Fluorene Molecular Rotary Motor, *J Chem Theory Comput*, 2011, **7**, 2189–2199.

157 Z. Lan, Y. Lu, O. Weingart and W. Thiel, Nonadiabatic Decay Dynamics of a Benzylidene Malononitrile, *J Phys Chem A*, 2012, **116**, 1510–1518.

158 H. Jin, M. Liang, S. Arzhantsev, X. Li and M. Maroncelli, Photophysical Characterization of Benzylidene Malononitriles as Probes of Solvent Friction, *J Phys Chem B*, 2010, **114**, 7565–7578.

159 D. Smith, The ion chemistry of interstellar clouds, *Chem Rev*, 1992, **92**, 1473–1485.

160 A. Sternberg and A. Dalgarno, Chemistry in Dense Photon-dominated Regions, *Astrophys J Suppl Ser*, 1995, **99**, 565.

161 E. Herbst and H.-H. Lee, New Dissociative Recombination Product Branching Fractions and Their Effect on Calculated Interstellar Molecular Abundances, *Astrophys J*, 1997, **485**, 689–696.

162 S. L. Guberman, in *Dissociative Recombination of Molecular Ions with Electrons*, ed. S. L. Guberman, Springer US, Boston, MA, 2003, pp. 1–11.

163 A. I. Florescu-Mitchell and J. B. A. Mitchell, Dissociative recombination, *Phys Rep*, 2006, **430**, 277–374.

164 C. H. Greene and Ch. Jungen, in *Advances in Atomic and Molecular Physics*, eds. D. R.

Bates and B. Bederson, Academic Press, 1985, vol. 21, pp. 51–121.

165 K. Nakashima, H. Takagi and H. Nakamura, Dissociative recombination of H+2, HD+, and D+2 by collisions with slow electrons, *J Chem Phys*, 1987, **86**, 726–737.

166 M. Tashiro and S. Kato, Quantum dynamics study on predissociation of H3 Rydberg states: Importance of indirect mechanism, *J Chem Phys*, 2002, **117**, 2053–2062.

167 S. M. Nkambule, Å. Larson, S. Fonseca dos Santos and A. E. Orel, Theoretical study of the mechanism of H2O+ dissociative recombination, *Phys Rev A (Coll Park)*, 2015, **92**, 12708.

168 T. Taketsugu, A. Tajima, K. Ishii and T. Hirano, Ab Initio Direct Trajectory Simulation with Nonadiabatic Transitions of the Dissociative Recombination Reaction HCNH+ + e– → HNC/HCN + H, *Astrophys J*, 2004, **608**, 323.

169 M. Kayanuma, T. Taketsugu and K. Ishii, Ab initio surface hopping simulation on dissociative recombination of H3O+, *Chem Phys Lett*, 2006, **418**, 511–518.

170 M. Kayanuma, T. Taketsugu and K. Ishii, An ab initio molecular dynamics study on the dissociative recombination reaction of HD2O+ + e-, *Theor Chem Acc*, 2008, **120**, 191–198.

171 K. Ishii, A. Tajima, T. Taketsugu and K. Yamashita, Theoretical Elucidation of the Unusually High [HNC]/[HCN] Abundance Ratio in Interstellar Space: Two-dimensional and Two-State Quantum Wave Packet Dynamics Study on the Branching Ratio of the Dissociative Recombination Reaction HCNH+ + e– → HNC/HCN + H, *Astrophys J*, 2006, **636**, 927.

172 T. Taketsugu and Y. Kobayashi, Ab initio surface hopping molecular dynamics on the dissociative recombination of CH3+, *Comput Theor Chem*, 2019, **1150**, 1–9.

173 I. T. Jolliffe, Ed., in *Principal Component Analysis*, Springer New York, New York, NY, 2002, pp. 338–372.

174 A. M. Virshup, J. Chen and T. J. Martínez, Nonlinear dimensionality reduction for nonadiabatic dynamics: The influence of conical intersection topography on population transfer rates, *J Chem Phys*, 2012, **137**, 22A519.

175 I. Borg and P. J. F. Groenen, *Modern multidimensional scaling: Theory and applications*, Springer Science & Business Media, 2005.

176 V. De Silva and J. B. Tenenbaum, *Sparse multidimensional scaling using landmark points*,

technical report, Stanford University, 2004.

177 J. B. Tenenbaum, V. de Silva and J. C. Langford, A Global Geometric Framework for Nonlinear Dimensionality Reduction, *Science (1979)*, 2000, **290**, 2319–2323.

178 S. T. Roweis and L. K. Saul, Nonlinear Dimensionality Reduction by Locally Linear Embedding, *Science (1979)*, 2000, **290**, 2323–2326.

179 X. Li, Y. Xie, D. Hu and Z. Lan, Analysis of the Geometrical Evolution in On-the-Fly Surface-Hopping Nonadiabatic Dynamics with Machine Learning Dimensionality Reduction Approaches: Classical Multidimensional Scaling and Isometric Feature Mapping, *J Chem Theory Comput*, 2017, **13**, 4611–4623.

180 H. M. Le, S. Kumar, N. May, E. Martinez-Baez, R. Sundararaman, B. Krishnamoorthy and A. E. Clark, Behavior of Linear and Nonlinear Dimensionality Reduction for Collective Variable Identification of Small Molecule Solution-Phase Reactions, *J Chem Theory Comput*, 2022, **18**, 1286–1296.

181 E. Becht, L. McInnes, J. Healy, C.-A. Dutertre, I. W. H. Kwok, L. G. Ng, F. Ginhoux and E. W. Newell, Dimensionality reduction for visualizing single-cell data using UMAP, *Nat Biotechnol*, 2019, **37**, 38–44.

182 T. Tsutsumi, Y. Ono, Z. Arai and T. Taketsugu, Visualization of the Intrinsic Reaction Coordinate and Global Reaction Route Map by Classical Multidimensional Scaling, *J Chem Theory Comput*, 2018, **14**, 4263–4270.

183 T. Tsutsumi, Y. Ono and T. Taketsugu, in *New Horizons in Computational Chemistry Software*, eds. M. Filatov, C. H. Choi and M. Olivucci, Springer International Publishing, Cham, 2022, pp. 55–77.

184 T. Tsutsumi, Y. Ono and T. Taketsugu, Multi-state Energy Landscape for Photoreaction of Stilbene and Dimethyl-stilbene, *J Chem Theory Comput*, 2022, **18**, 7483–7495.

185 W. Shi, T. Jia and A. Li, Quasi-classical trajectory analysis with isometric feature mapping and locally linear embedding: Deep insights into the multichannel reaction on an NH3+(4A) potential energy surface, *Physical Chemistry Chemical Physics*, 2020, **22**, 17460–17471.

186 G. H. Peslherbe, H. Wang and W. L. Hase, in *Advances in Chemical Physics*, 1999, pp. 171–201.

187 M. Paranjothy, R. Sun, Y. Zhuang and W. L. Hase, Direct chemical dynamics simulations:

coupling of classical and quasiclassical trajectories with electronic structure theory, *WIREs Computational Molecular Science*, 2013, **3**, 296–316.

188 W. Shi, K. Wang, P. Zhang, L. Yu and A. Li, Mode-specific dynamics in multichannel reaction NH++ H2, *Physical Chemistry Chemical Physics*, 2021, **23**, 20352–20358.

189 Y. C. Minh and E. F. van Dishoeck, Astrochemistry: From Molecular Clouds to Planetary Systems, *From Molecular Clouds to Planetary*.

190 L. Yue, L. Yu, C. Xu, C. Zhu and Y. Liu, Quantum yields of singlet and triplet chemiexcitation of dimethyl 1,2-dioxetane: ab initio nonadiabatic molecular dynamic simulations, *Physical Chemistry Chemical Physics*, 2020, **22**, 11440–11451.

191 Y. Fan, J. Chen, L. Yu, A. Li, G. Zhai, Y. Lei and C. Zhu, Methyl substitution enhanced photoisomerization of trans,trans-1,4-diphenyl-1,3-butadiene: direct ab initio trajectory surface hopping dynamic simulations, *Physical Chemistry Chemical Physics*, 2018, **20**, 2260–2273.

192 M. Yang, C. Huo, A. Li, Y. Lei, L. Yu and C. Zhu, Excited-state E → Z photoisomerization mechanism unveiled by ab initio nonadiabatic molecular dynamics simulation for hemithioindigo–hemistilbene, *Physical Chemistry Chemical Physics*, 2017, **19**, 12185–12198.

193 C. Xu, L. Yu, F. L. Gu and C. Zhu, Probing the π → π* photoisomerization mechanism of trans-azobenzene by multi-state ab initio on-the-fly trajectory dynamics simulations, *Physical Chemistry Chemical Physics*, 2018, **20**, 23885–23897.

194 X. Zheng, G. Zhai, W. Gao, Y. Lei, L. Yu and C. Zhu, Photoisomerization mechanisms from trans, trans-1,4-diphenyl-1,3-butadiene: CASSCF on-the-fly trajectory surface hopping dynamic simulations, *Physical Chemistry Chemical Physics*, 2016, **18**, 8971–8979.

195 Y. Lei, H. Wu, X. Zheng, G. Zhai and C. Zhu, Photo-induced 1,3-cyclohexadiene ring opening reaction: Ab initio on-the-fly nonadiabatic molecular dynamics simulation, *J Photochem Photobiol A Chem*, 2016, **317**, 39–49.

196 L. Yu, C. Xu and C. Zhu, Probing the π → π∗ photoisomerization mechanism of cis-azobenzene by multi-state ab initio on-the-fly trajectory dynamics simulation, *Physical Chemistry Chemical Physics*, 2015, **17**, 17646–17660.

197 L. Yue, L. Yu, C. Xu, Y. Lei, Y. Liu and C. Zhu, Benchmark Performance of Global Switching versus Local Switching for Trajectory Surface Hopping Molecular Dynamics

Simulation: Cis↔Trans Azobenzene Photoisomerization, *ChemPhysChem*, 2017, **18**, 1274–1287.

198 L. Yu, C. Xu, Y. Lei, C. Zhu and Z. Wen, Trajectory-based nonadiabatic molecular dynamics without calculating nonadiabatic coupling in the avoided crossing case: Trans↔cis photoisomerization in azobenzene, *Physical Chemistry Chemical Physics*, 2014, **16**, 25883–25895.

199 M. W. Walker, L. Shao and R. A. Volz, Estimating 3-D location parameters using dual number quaternions, *CVGIP: Image Understanding*, 1991, **54**, 358–367.

200 P. Celani and H.-J. Werner, Multireference perturbation theory for large restricted and selected active space reference wave functions, *J Chem Phys*, 2000, **112**, 5546–5557.

Ackonwagement

As I complete this graduation thesis, I am filled with gratitude and wish to express my heartfelt thanks to everyone who has supported and helped me throughout this journey.

First and foremost, I would like to express my deepest gratitude to my advisor, Professor Taketsugu. His patient guidance, valuable advice, and meticulous support throughout the topic selection, research methods, and writing process have been invaluable. His direction not only illuminated the path for my research but also provided timely assistance and encouragement during difficult times, enabling me to complete this thesis smoothly. I also want to thank my family for their unwavering support. My parents' and girlfriend’s care and encouragement kept me in good spirits and provided me with the motivation I needed during my research. Their understanding and patience, especially during my most challenging times, allowed me to fully dedicate myself to my thesis writing. Additionally, I am grateful to all members of quantum chemistry lab. Throughout the writing process, they offered numerous valuable suggestions and shared useful resources and information, helping to broaden my research perspective. Their companionship and encouragement helped me feel less alone and more capable in the face of pressure and difficulties. Finally, I would like to thank all the teachers and staff who assisted me during my research. Your support and help were crucial to the successful completion of my thesis.

Although the acknowledgment section is brief, the impact of everyone who has helped and supported me throughout my academic journey is deeply imprinted in my heart. Thank you once again!